MAXIMUM LIKELIHOOD FITTING OF TIDAL STREAMS WITH APPLICATION TO THE SAGITTARIUS DWARF TIDAL TAILS

By

Nathan Cole

A Thesis Submitted to the Graduate

Faculty of Rensselaer Polytechnic Institute

in Partial Fulfillment of the

Requirements for the Degree of

DOCTOR OF PHILOSOPHY

Major Subject: MULTIDISCIPLINARY SCIENCE

Approved by the
Examining Committee:

Heidi Jo Newberg, Thesis Adviser

Malik Magdon-Ismail, Member

Wayne Roberge, Member

Kristin Bennett, Member

Mohammed Zaki, Member

Rensselaer Polytechnic Institute
Troy, New York

May 2009
(For Graduation May 2009)

CONTENTS

LIST OF TABLES iii

LIST OF FIGURES iv

ACKNOWLEDGMENT viii

ABSTRACT x

1. Introduction and Historical Review 1
   1.1 The Milky Way Galaxy 2
   1.2 Sloan Digital Sky Survey 3
   1.3 The Discovery of Spheroid Substructure 6
   1.4 Ongoing Spheroid Questions 9
   1.5 Machine Learning 10
      1.5.1 The Method of Maximum Likelihood 11

2. Methods and Algorithms 14
   2.1 The Probability Density Function 14
      2.1.1 The Tidal Stream Model 14
      2.1.2 The Stellar Spheroid Model 18
      2.1.3 The Absolute Magnitude Distribution Model 19
      2.1.4 The Combined Probability Density Function 23
      2.1.5 Removing Sections from the Volume 25
      2.1.6 Multiple Pieces of Tidal Debris 26
      2.1.7 The Complete Probability Density Function 28
   2.2 Optimization 29
      2.2.1 Conjugate Gradient Technique 29
      2.2.2 Line Search Technique 32
      2.2.3 Run Time and Distributed Computing 35
      2.2.4 A Generic Maximum Likelihood Evaluator 36
   2.3 Analysis Methods 38
      2.3.1 Errors in the Estimated Parameter Values 38
      2.3.2 Separating the Tidal Debris from the Spheroid 40

3. Validating the Algorithm via Simulated Datasets 42
  3.1 Generating the Datasets 42
    3.1.1 Generating the Tidal Debris 42
    3.1.2 Generating the Stellar Spheroid 43
    3.1.3 Achievable Accuracies 44
  3.2 Testing 45
    3.2.1 Simulated Stripe 82 46
    3.2.2 Simulated Stripe 86 With Volume Removal 50
    3.2.3 Simulated Stripe 82 With Two Streams 53
  3.3 Robustness of the Models 59
    3.3.1 Impact of Magnitude Distribution 61
    3.3.2 Stream Model Correctness 61
    3.3.3 Spheroid Model Correctness 65
4. SDSS Data Analysis 67
  4.1 The Datasets 67
    4.1.1 Fitting the Datasets 69
  4.2 SDSS Stripe 82 70
  4.3 Additional SDSS Stripes 74
5. Discussion and Conclusions 107
  5.1 The Sagittarius Tidal Stream 107
    5.1.1 Trailing Tail 107
    5.1.2 The Leading Tail 111
  5.2 Global Stream Analysis 114
  5.3 The Stellar Spheroid 119
  5.4 Overview 125
  5.5 Future Work 128
LITERATURE CITED 129

APPENDICES

A. Standard Candles 144

LIST OF TABLES

2.1 Perturbation values used for the gradient and Hessian 33

3.1 Stripe 82 Simulated Dataset Results 49

3.2 Stripe 86 Simulated Dataset Results 54

3.3 Stripe 82 Simulated Dataset with Two Streams Results 57

3.4 Results of Tests Fitting an Incorrect Stellar Spheroid Model 66

4.1 SDSS Stripe 82 Results 72

4.2 SDSS Stripe Dataset Statistics 76

4.3 SDSS Stripe Results 77

4.4 SDSS Stripe Results Supplemental 78

5.1 Spheroid results by stripe. 124

LIST OF FIGURES

2.1 The definitions of the data volume and the stream parameters. 16

3.1 Stripe 82 simulated dataset density wedge plot. 47

3.2 Stripe 82 simulated dataset separated density wedge plots. 51

3.3 Stripe 86 simulated dataset with volume section removed density wedge plot. 52

3.4 Stripe 86 simulated dataset with volume section removed separated density wedge plots. 55

3.5 Stripe 82 simulated dataset with two tidal streams density wedge plot. . 58

3.6 Stripe 82 simulated dataset with two tidal streams separated density wedge plots. 60

3.7 Cross section and histogram of N-body and model-generated streams. . 63

3.8 N-body simulation of Sgr dSph disruption. 64

4.1 SDSS stripe 82 dataset density wedge plot. 71

4.2 SDSS stripe 82 dataset separated density wedge plots. 73

4.3 SDSS stripe 86 dataset density wedge plot. 79

4.4 SDSS stripe 86 dataset separated density wedge plots. 80

4.5 SDSS stripe 79 dataset density wedge plot. 81

4.6 SDSS stripe 79 dataset separated density wedge plots. 82

4.7 SDSS stripe 23 dataset density wedge plot. 83

4.8 SDSS stripe 23 dataset separated density wedge plots. 84

4.9 SDSS stripe 22 dataset density wedge plot. 85

4.10 SDSS stripe 22 dataset separated density wedge plots. 86

4.11 SDSS stripe 21 dataset density wedge plot. 87

4.12 SDSS stripe 21 dataset separated density wedge plots. 88

4.13 SDSS stripe 20 dataset density wedge plot. 89

4.14 SDSS stripe 20 dataset separated density wedge plots. 90

4.15 SDSS stripe 19 dataset density wedge plot. 91

4.16 SDSS stripe 19 dataset separated density wedge plots. 92

4.17 SDSS stripe 18 dataset density wedge plot. 93

4.18 SDSS stripe 18 dataset separated density wedge plots. 94

4.19 SDSS stripe 17 dataset density wedge plot. 95

4.20 SDSS stripe 17 dataset separated density wedge plots. 96

4.21 SDSS stripe 16 dataset density wedge plot. 97

4.22 SDSS stripe 16 dataset separated density wedge plots. 98

4.23 SDSS stripe 15 dataset density wedge plot. 99

4.24 SDSS stripe 15 dataset separated density wedge plots. 100

4.25 SDSS stripe 13 dataset density wedge plot. 101

4.26 SDSS stripe 13 dataset separated density wedge plots. 102

4.27 SDSS stripe 11 dataset density wedge plot. 103

4.28 SDSS stripe 11 dataset separated density wedge plots. 104

4.29 SDSS stripe 9 dataset density wedge plot. 105

4.30 SDSS stripe 9 dataset separated density wedge plots. 106

5.1 Sgr dSph orbital plane face on. 109

5.2 Sgr dSph orbital plane edge on. 110

5.3 Sgr dSph orbital plane face on with simulation. 112

5.4 Galactic coordinate density plot of North Galactic cap F turnoff stars. . 113

5.5 Width versus angle along the stream. 116

5.6 Density versus angle along the stream. 118

5.7 New Sgr dSph orbital plane face on. 120

5.8 New Sgr dSph orbital plane edge on. 121

5.9 Sgr dSph orbital plane fit with trailing tail and Sgr dSph viewed edge on. 122

5.10 Galactic coordinate density plot of North Galactic cap stars after removing the Sgr stream. 126

5.11 Galactic coordinate density plot of North Galactic cap Sgr stream stars. 127

ACKNOWLEDGMENT

First, and foremost, I would like to thank my advisor/mentor, Heidi Newberg. If not for her tutelage, drive, and complete dedication to the purity of the sciences; my journey would have been drastically more difficult if not impossible. She is one of the strongest and most interesting people I have ever met, and I consider myself blessed to have been able to spend these past years under her wing and hope to maintain a lasting relationship with her.

I would also like to thank Malik Magdon-Ismail. He has been a second advisor all but on paper, and I am grateful for that. He has always provided a unique approach to problems or been good enough to point out the obvious when it has been overlooked. And, while it will not say he has done any more for me than sit on my committee; it will never be forgotten that he has always went above and beyond any other.

It is with a great amount of gratitude that I thank the rest of my committee Wayne Roberge, Kristin Bennett, and Mohommed Zaki. They have been good enough to accompany me on this path less traveled that is the Multidisciplinary track, and despite all its pitfalls and abruptness of some of the obstacles they have been there through it all. I would like to extend an additional hand to Wayne Roberge for the countless hours I have spent in his classes reaping the benefits of his experience. He has been (and is) a wonderful teacher to me; both in and out of the classroom.

Thanks also must go to the Astroinformatics group: Boleslaw Szymanksi, Carlos Varela, and of course Travis Desell. They have been a panel to try ideas and offer encouragement and guidance. A special thanks must also go to Travis Desell who has been on this journey with me simply on a slightly different path. I only hope I have managed to aide in his success as much as he has mine. Thanks also to those other members past and present for the work they have added to the project.

I would like to thank all those here at Rensselaer, both from my lab and otherwise, that have provided aide to this work or simply friendship over these years: Ben Willett, Amanda Cook, Jonathan Purnell, Kris Dawsey, Xinyang "Fred" Liu, Warren Hyashi, James Wisniewski, and anyone else that has graced my time here. Thanks also to Brian Yanny for his help regarding SDSS specific problems.

I would like to take this time to thank a few special people that have helped me along either through support, teachings, friendship or all of the above. Dan Owens, Thomas Albin, and Jeremy Sweeney, for your friendship and stimulating conversations and adventures. David Haines, who taught me how to be a part of something bigger than myself. Sarah (Smith) Buffington, whose intense love of science was infectious. And, not to forget: Todd Brown, Fujiko Sawtarie, Majid Sawtarie, Dr. Lozier, for the considerable time spent with me during my undergrad career.

Additionally, I would like to send my deepest love and gratitude to my parents: Dale and Barbara Cole, for their love and support throughout the years. They have always pushed me to be my best, but let me choose my own path (mistakes and all). I cannot fathom a better pair to call "Mom and Dad." I love you, and I thank you for everything! Thanks also goes to my brother Jacob for his love and support. I would also like to thank and acknowledge my grandparents Kenneth and Esther Bykens and Allen and Betty Cole; you have always been there for me regardless of the time/need and I know your thoughts are always with me no matter how far apart. I would also like to thank the rest of my family, and while there is far too many of you that have influenced and taught me how to get to this point, I just want all of you to know, I appreciate what you have done for me far more than you probably know and hope only to repay your kindness. I would like to point out my uncle, William Bykens; he introduced me to the stars and to the joys of computers; without him I could not be where I am today.

Lastly, I would like to thank my wonderful wife, and best friend, Jacqui. She is my world, and I do not know what I would do without her. She has stood by me through all the ups and downs of life since we met. She has pushed me to be a better person and to be the best that I can be. I love you and thank you for all you have done, and I look forward to all that is to come with you at my side.

ABSTRACT

A maximum likelihood method for determining the spatial properties of tidal debris and of the Galactic spheroid is presented. Over small spatial extent, the tidal debris is modeled as a cylinder with density that falls off as a Gaussian with distance from its axis while the smooth component of the stellar spheroid is modeled as a Hernquist profile. The method is designed to use 2.5° wide stripes of data that follow great circles across the sky in which the tidal debris within each stripe is fit separately. The maximum likelihood method is defined with the ability to fit any number of tidal streams within the input dataset, as well as, to be able to remove sections from the probed volume. The effectiveness and correctness of the algorithm is then demonstrated through the use of three simulated datasets which mimic the conditions found within real datasets: a single stream and the spheroid, a single stream and the spheroid with a section of the probed volume removed, and two streams and the spheroid. The algorithm is shown to perform well under all conditions using the conjugate gradient method coupled with a line search as the optimization method.

A probabilistic separation technique which allows for the extraction of the optimized tidal streams from the input data set is presented. This technique allows for the creation of separate catalogs for each component fit in the stellar spheroid: one catalog for each piece of tidal debris that fits the density profile of the debris and a single catalog which fits the density profile of the smooth stellar spheroid component. This separation technique is proven to be effective by extracting the simulated tidal debris from the simulated datasets. A method to determine the statistical errors is also developed which utilizes a Hessian matrix to determine the width of the peak at the maximum of the likelihood surface. This error analysis method serves as a means of testing the the algorithm with regard to the simulated datasets as well as determining the statistical errors of the optimizations over observational data. An heuristic method is also defined for determining the numerical error in the optimizations.

The maximum likelihood algorithm is then used to optimize spatial data taken from the Sloan Digital Sky Survey. Stars having the color of blue F turnoff stars $0.1 < (g - r)_0 < 0.3$ and $(u - g)_0 > 0.4$ are extracted from the Sloan Digital Sky Survey database. In the algorithm, the absolute magnitude distribution of F turnoff stars is modeled as a Gaussian distribution, which is an improvement over previous methods which utilize a fixed absolute magnitude $M_{g_0} = 4.2$ value to estimate stellar distances. Fifteen stripes were extracted and used to trace the Sagittarius Dwarf Spheroidal galaxy tidal stream. These analyses characterize the Sagittarius tidal stream in both the trailing tidal tail and the leading tidal tail.

Comparing these detections with that of the current models for the Sagittarius dwarf galaxy disruption shows that there is considerable disagreement. The positions along the trailing tidal tail correspond well with the model disruption; however, the leading tidal tail positions differ greatly from those seen in the model disruptions indicating that new models need to be created to better fit the observations. The widths of the trailing tail show some evidence for increasing as the magnitude of the angle along the stream increases. This trend is also present in the model simulation. The leading tidal tail, however, shows a trend in decreasing width as the magnitude of the angle along the stream increases. Again, this trend is seen in the model disruption. Both the trailing and leading tidal tails show a distinct trend in decreasing density as the magnitude of the angle along the stream increases, and the leading tidal tail of the model disruption shows this trend as well. However, the model disruption shows that the density along the trailing tidal tail remains relatively constant as the magnitude of the angle along the stream increases. Finally, the fifteen stripes analyzed contain 9.0% as many F turnoff stars as currently seen in the Sgr dSph. This implies considerable disruption of the galaxy.

A new orbital plane of the Sagittarius dwarf galaxy has been calculated, using the fifteen detections of the Sgr stream, with equation $-0.207X + 0.925Y + 0.319Z - 1.996 = 0$. The leading tidal tail lies along this plane while the Sgr core and the trailing tail do not. A second plane was fit to the three southern detections and the Sagittarius dwarf position and is described by equation $0.024X + 03990Y + 0.136Z - 1.801 = 0$. The leading and trailing tails are fit well with these two planes, respectively. There is approximately a 17° difference in orientation of these two planes and may imply a strong precession of the orbit of the Sagittarius dwarf.

The separation technique was applied to the analyzed data to successfully create a catalog of stars matching the density profile of the Sagittarius tidal streams; however, these stars do not explicitly represent stars drawn from the Sagittarius tidal stream. The stream was then successfully extracted from the data resulting in a much smoother spheroid. Therefore, through the fitting and extraction of all tidal debris in the data using this method, the smooth component of the spheroid may be recovered for uncontaminated study to determine the true structure of the smooth spheroid. The primary use of the stream catalog, beyond analysis of the Sagittarius stream itself, would be to apply it as a means to generate simulations, thereby constraining the models used in these simulations, specifically that of the Galactic potential which would allow for the determination of the distribution of mass, and therefore dark matter, in the Milky Way.

CHAPTER 1

Introduction and Historical Review

The heavenly bodies, specifically those of the night sky, have always held an important place in the history of mankind. They have been revered through religion spanning much of history and the globe through astrology [1], used as a means to navigate the world via astronavigation, to tell stories via constellations, or simply to generate a feeling of awe as one looks up at the vast reaches of space. Those heavenly bodies have also served as a means to study the universe around us. Without the study of those bodies, some of the most fundamental concepts of the universe, such as gravity, may still be unknown and misunderstood. However, through the careful study of the movements of the planets Kepler and Newton were able to usher a new era of science. Galileo can arguably be considered to have had the largest impact upon the field of astronomy; for 400 years ago he pointed the first telescope towards the sky (a tube containing refractive lenses). Though crude by today's standards, this 3x magnification device provided the prototype for the primary method through which to study the objects of the night sky.

After Galileo's first telescope, it was desired to create telescopes of greater magnification. However, the nature of a refractive telescope causes this to be quite difficult due to chromatic aberration causing the image to blur. This effect was solved by using a reflective telescope, which uses mirrors to collect light as opposed to lenses. Although not free of optical aberrations, the reflective telescope design has proven the superior model and has been used in the design of almost all major telescopes.

It was upon one of these reflective telescopes, the 100 inch Hooker telescope at the Mount Wilson Observatory that Edwin Hubble discovered that the Milky Way was but one many galaxies within the universe. He also discovered that these other galaxies were retreating away from the Milky Way thus proving the existence of an expanding universe. [2] Since these incredible discoveries, the astronomical community has continued to study the universe around us in an effort to understand its nature, structure, past, and future.

1.1 The Milky Way Galaxy

The Milky Way galaxy is the host galaxy to the Solar planetary system, which contains the Earth. It is a spiral galaxy, more specifically a SBb/c Hubble type spiral consisting of four major arms. [3] [4] This means that the Milky Way is a disk type galaxy with loosely wound spiral arms and a bar structure at its center. The Galaxy also contains the those features typical of a spiral Galaxy: a roughly spherical bulge at its center, a planar disk containing the spiral arms, and a halo with the other structures embedded. It has long been accepted that the Milky Way has a circular velocity of 220 km s^{-1} at the Solar distance of about 7.5 kpc from the Galactic center, and a mass of approximately $6 \cdot 10^{11}$ $\mathrm{M}_{\cdot}$, however, recent finding by the Very Long Baseline Array (VLBA) have determined that the Milky Way has a rotational velocity of 254 km s^{-1} at a Solar distance of approximately 8.5 kpc and has a mass of nearly $3 \cdot 10^{12}$ $\mathrm{M}_{\cdot}$. [5]

The disk of the Milky Way contains two populations of stars: a thin disk with scale height of approximately 55 pc, and a thick disk with scale height of approximately 375 pc. [6] This thin disk is composed of a younger, more metal rich, population of stars, while the thick disk is older and more metal poor. The disk of the Galaxy contains the majority of the gas/dust of the Milky Way; for this reason, the vast majority of the current star formation of the Galaxy occurs in the disk and bulge. Despite the relatively small volume occupied by the disk of the Galaxy, almost all of the light emitted by the Milky Way comes from the disk, due to the existence of bright young stars in this component.

The stellar halo, or spheroid, of the Milky Way extends over a large volume and contains the majority of the mass of the Galaxy. This mass is primarily dark matter, however. Dark matter is a proposed constituent of the Universe that emits/reflects no light and is observable only via its gravitational mass. The nature of the dark matter and its distribution within the halo of the Milky Way is unknown. For many years, the spheroid was imagined to have formed in conjunction with the rest of the Galaxy and gradually evolved to its current state as the other components collapsed inward. [7] [8] It has also long been imagined to have a smooth and continuous power law density distribution. [9] However, the advancement in technology and analysis techniques led to the discovery of a large amount of substructure, to be discussed in section 1.3, and has shown that at least some of the spheroid was constructed via merger events and that the spheroid was composed of debris from hierarchical structure formation. [10] The discovery of multiple pieces of substructure has caused a shift in the thinking regarding the spheroid. The continuing studies and discoveries have been aided through the development and operation of large scale surveys such as the Two-Micron All-Sky Survey (2MASS) and the Sloan Digital Sky Survey (SDSS). Without projects such as these, it would be incredibly difficult to generate the amount at a high enough accuracy to further this field of study.

1.2 Sloan Digital Sky Survey

The Sloan Digital Sky Survey (SDSS) is a large, international astronomy collaboration. The survey was originally developed to find, and study, galaxies and the largest structures within those galaxies in the universe. However, since its inception, the survey has become one of the most prosperous and influential projects in astronomical history with major discoveries across the astronomical field (from asteroids to cosmology). The SDSS was constructed to perform an imaging survey of 10,000 deg^2 of the sky while simultaneously collecting over 1,000,000 galactic spectra which were to be selected via photometry (from the images). The survey included two distinct operational phases, SDSS-I and SDSS-II, which were completed from 2000-2005 and 2005-2008, respectively. The first of these phases saw the collection of over 8,000 deg^2 of sky and spectra of galaxies and quasars selected from this imaging. The second phase was composed of three distinct surveys: the Sloan Legacy Survey, the Sloan Extension for Galactic Understanding and Exploration (SEGUE), and the Sloan Supernova Survey.

After its completion in the summer of 2008, a seventh and final data release (DR7) was released to the public including all of the SDSS-I, Sloan Legacy, SEGUE, and Sloan Supernova data. The Sloan Legacy Survey endeavored to complete the original SDSS imaging and spectroscopy studies. The surveyed 8,400 deg^2 of sky saw the detection of 230,000,000 unique objects and spectra of 930,000 galaxies, 120,000 quasars, and 225,000 stars. SEGUE was a project developed specifically to probe the Milky Way itself in an effort to study the history and structure of the Galaxy. This effort was completed with the collection of 3,500 deg^2 of additional imaging data and spectra of 240,000 stars targeted across various fields. [11] This new imaging data is taken along stripes as well, however, the great circles that define the SEGUE stripes are not necessarily those used for the SDSS proper, nor do they form a contiguous dataset. The SEGUE survey specifically targets interesting areas, and sparsely samples all directions of the sky that are visible from the observatory. The Sloan Supernova Survey discovered and studied supernovae and other variable objects. [12] [13] This was accomplished by repeatedly surveying of the southern Celestial Equator (Equatorial stripe) composed of 300 deg^2 and the three month project saw the discovery of over 500 supernova type Ia, which have been spectroscopically confirmed.

The SDSS data is taken in stripes, that follow great circles, across the sky. The entire sky is divided up into 144 numbered stripes, 2.5° in width, that begin and end at the survey poles: $(l, b) = (209.33°, -7°)$ and $(29.33°, 7°)$. The stripes designated as 10 and 82 are centered on the Celestial Equator with stripe 10 in the north Galactic cap and stripe 82 in the south. The other stripes are numbered sequentially with inclinations 2.5° apart. If every stripe were imaged across the entire 180° length of stripes, a total of 64,800 deg^2 of imaging data would be collected, compared with the 41,253 deg^2 in the entire sky. The overlap between stripes increases towards the survey poles. The SDSS, however, typically observes only those areas greater than thirty degrees from the survey poles. There is approximately a 50% overlap at the end of each stripe and almost no overlap on the survey Equator (at $\alpha = 185°$). [14]

The survey was completed using a dedicated 2.5 meter dedicated telescope. This telescope is housed, operated, and maintained at the Apache Point Observatory in New Mexico. This telescope is composed of two instruments: an imaging camera and a pair of spectrographs. The SDSS images are taken with an array of thirty 2,048 x 2,048 pixel charge-coupled device (CCD) cameras. [15] CCDs have become ubiquitous in the world and have become popular in the world of digital photography, astronomy, microscopy, and other fields. After being theorized by Eugene Lally in 1961 as a means for taking digital images [16] during interplanetary travel, the device was subsequently invented at the AT&T Bell Lab by Willard Boyle and George Smith in 1969. [17] The devices operate through the use of accumulated charge in a capacitor proportional to the intensity of light at a specific location on the device. In this manner, the collected "light" can be transformed into a digital image.

The SDSS CCD array operates in a drift-scan mode. This means that the telescope is panned, in an arc, across the visible sky. This scan produces six "scan lines" of data, each of which are 13.6° wide. The "scan lines" grow in length at a rate of 15° per hour over the course of a run. In each of these scan lines the sky is imaged with coverage from 3,000 to 11,000 Angstroms in five optical filters: u, g, r, i, and z. This five filter system means that the time with which an astronomical object is imaged is a few minutes different for each passband. [18] [19] Drift scans are most easily completed along the Celestial Equator where the telescope does not move as the sky moves by at a rate of 15° per hour. The SDSS pioneered the driven drift scan , in which the telescope is moved in combination with the sky moving by, so any great circle can be scanned. A complete stripe of data is generated when a second set of six scan lines are observed to fill in the gaps between the scan lines in the first data collection. This resulting stripe is 2.5° wide and its length is dependent upon the time the sky was observed during the runs used to complete the stripe. Each of these stripes follows a great circle across the sky and is composed of two or more runs.

The SDSS spectroscopic studies are completed using two 320-fiber double (blue/red) spectrographs. This means that the spectrograph can simultaneously obtain a total of 640 unique objects in both the blue and red part of the spectrum. The spectral resolution of these instruments are R = 1,800. Additional information regarding the spectrographs and the SDSS technical specifications, procedures, and calibrations can be found in [20], [21], and [22]. Further information regarding SDSS technical details, operation, and specific datasets can be found in the data release publications: DR1 [23], DR2 [24], DR3 [25], DR4 [26], DR5 [27], DR6 [28], and the final and complete release of the entire SDSS catalog in DR7 [29] and the SDSS website [30].

The SDSS was a well designed, large, and extremely well calibrated imaging survey. The SDSS spectroscopic study also included a large number of stellar spectra. These two facts have led the SDSS to provide a significant contribution to the knowledge of the Milky Way, particularly the spheroid. The discovery of new spheroid substructure has been driven primarily by the SDSS, as is discussed in the next section.

1.3 The Discovery of Spheroid Substructure

Spheroid substructures can be divided into the study of specific types: globular clusters, dwarf galaxies, and gravitational unbound structures primarily consisting of tidal streams. Globular clusters are gravitationally bound groupings of stars which formed from the same interstellar medium at approximately the same time. This similar history means that the stars within the cluster have similar properties such as metallicity and age. Dwarf galaxies are relatively small galactic bodies which are bound by the Milky Way's gravitational potential.

Tidal streams are a recent discovery having only been discovered in the past decade. A tidal stream occurs as a gravitationally bound object (i.e. a globular cluster or dwarf galaxy) comes under the gravitational potential of another larger object (i.e. the Milky Way). As the smaller object traverses the gravitational potential of the Milky Way, and approaches the Galactic center, it comes under the influence of differential gravitational forces (tidal forces) which cause stars to become stripped (gravitationally unbound) from the smaller object. As the disrupted object continues to traverse the potential the stripped stars are drawn out into long streams of stars (tidal streams) that lead and trail the core of the object. Those stars with lower energies are drawn into the leading tail, while those with higher energies fall behind and form the trailing tail. Over time, these tails extend to farther distance from the core of the original object as more stars are stripped and added to the tidal tail. Given sufficient time, the entirety of the previously bound structure will be disrupted, leaving only the tidal stream. The tidal stream itself will continue to assimilate into the Milky Way spheroid until all traces of the merger have been erased.

As previously discussed, the spheroid was thought to have a smooth distribution. The discovery of the Sagittarius (Sgr) Dwarf Spheroidal (dSph) galaxy in 1994 in [31]. As with many important discoveries in the sciences, it was accidental. During a study of giant stars towards the Galactic center using 2MASS data, a very large overdensity was discovered which was later identified as the core of the Sgr dSph. Despite its close proximity to the Milky Way, it was not previously detected because the Sgr dSph is on the opposite side of the Milky Way center slightly below the Galaxy's plane. This positioning requires all observations of the Sgr dSph to be taken through the Galactic plane and towards the center which introduces a high amount of foreground contamination.

The existence of stellar tidal streams were theorized only, but evidence to support this theory was found in the existence of unbound globular cluster stars and moving groups of stars with no obvious bound progenitor. [32] [33] [34] [35] The discovery of the Sgr dSph's associate tidal stream provided irrefutable evidence of stellar tidal streams and provided the first evidence of a current merger event, and remains the most impressive example discovered. [36] [37] [38] The tidal stream circles the entire sky and can be seen to be several kiloparsecs wide.

Since the Sgr tidal stream discovery, the search for and study of tidal streams has exploded. These studies can be divided into two primary methods: kinematic and spatial. The kinematic approach is to search for co-moving groups of stars in phase space. That is to say, identification of groups of stars in a similar location with common velocities. These co-moving groups potentially indicate they were once part of a bound structure as opposed to part of the smooth stellar spheroid. This approach is a very powerful way to discover and study substructure, however, it is limited in that it requires a spectroscopic study of all of the stars within the sample in order to generate the phase space characteristics. Since spectroscopy is somewhat difficult to obtain, the amount of data for use in these types of studies are somewhat limited.

The spatial technique for substructure studies seeks to determine only those places that exhibit an overdensity in the number of star counts. This method utilizes only photometric data (images) which is much easier to obtain than that of spectroscopic data and therefore benefits from a greater amount of data to analyze. This type of study is conducted by looking for statistically relevant deviations from an assumed background distribution, for the stellar spheroid in this case. The relevant deviations are therefore candidate tidal debris that may be analyzed further for confirmation. Though both techniques have proven to be an effective means of tidal debris study, the majority of the discoveries of substructure in the spheroid of the Milky Way have come from the use of photometric data.

Beyond the Sgr tidal stream, a number of other tidal debris streams are thought to be associated with dwarf galaxies have been discovered. The Monoceros stream was discovered in the Galactic plane towards the Galactic anti-center. [39] [40] New studies have shown this feature to contain many identifiable streams that appear to be parallel orbits. [41] [42] Additional debris has been found in Tringulum-Andromeda which may be connected to the Monoceros stream. [43] [44] The overdensity in Virgo appears to be composed of one or more structural components including the Virgo stellar stream. [45] [46] [47] The Orphan stream is a small, low-surface brightness tidal stream with an unknown progenitor. [48] [49] The most recent is the newly discovered Cetus Polar Stream. [50] Nine new low-surface brightness dwarf galaxy satellites of the Milky Way have also been discovered, though no tidal tails have been discovered to this point. [51] [52] [53] [54] [55] [48] [56] There is some evidence that these satellite galaxies of the Milky Way were actually part of a galaxy group and fell into the Galactic potential together. [57]

Globular cluster tidal tails have also been found to span many tens of degrees across the sky: Pal 5 [58] [59] [60] and NGC 5466 [61] [62]. The Styx stream is currently thought to be the disruption of Bootes III. [63] At least four streams associated with globular clusters have also been found with unknown progenitors. [63] [64]

There is also ongoing work to study the nature of the spheroid itself. In [65] evidence is presented supporting the existence of the Hercules-Aquila cloud as a spheroid component. Also, in [66] suggests the spheroid is actually composed of an two overlapping, counter-rotating components creating an inner and outer stellar halo/spheroid.

The Sgr tidal stream has been the most extensively studied stream. Measurements of position, velocity, and metallicity have been taken all across the sky. [39] [67] [47] [68] [69] [70] [71] [72] [73] These measurements have then been used to model the disruption of the Sgr dSph. [74] [75] [76] [77] [78] [79]. Despite the large amount of work done, there is still much that is unknown about the Sgr stream. This is in part due to the difficulty in comparing models to the data. In fact, the recent detections of the Sgr tidal stream have proven inconsistent with the simulations. A self-consistent and robust method for analyzing the Sgr stream, and tidal debris in general, is needed so that improved simulations can be generated.

1.4 Ongoing Spheroid Questions

Despite all that has been learned of the spheroid within recent history, many of the biggest questions still remain. It has clearly been shown that the spheroid is not simply a smooth power law. However, it remains to be seen if there is an underlying smooth distribution. One way to study this would be to analyze those regions that contain no substructure; however, it has become almost impossible to guarantee that an area contains no substructure given the number of substructures discovered already. A better technique would therefore be to remove the substructure from the data leaving only spheroid stars which can then be analyzed separately for a smooth component.

The determination of the existence of a smooth spheroid component would also serve as a method to study the evolution and formation of the Milky Way. Should a smooth component not be present, this would be evidence that the entire spheroid was constructed via hierarchical formation through merger events. However, the existence of a smooth underlying spheroid component would provide evidence that the spheroid initially evolved from the Milky Way as its other structural components and that the substructure was added at a later time via mergers or has had a significant amount of time to completely relax.

It is also important to determine the distribution of mass within the spheroid.

Given this is dominated by the dark matter of the Galaxy, which has not yet been detected directly. Thus, the only possibility is to study dark matter through its effects on luminous matter. Through the use of computational techniques, it is possible to simulate merger events through time until the present. This is done, primarily via N-body computations, by evolving the system until the simulation matches that which is seen in the observational data.

Tidal streams provide an excellent tracer of the Galactic potential, for they provide a trail which traces out the Galactic potential through which the disrupted body passed. [80] Thus, by evolving a simulated galaxy to have the same tidal stream features and dynamics as the observational data, it is possible to constrain the Galactic potential, and therefore the mass, and ultimately the dark matter distribution of the Galaxy. To accomplish these simulations with the needed accuracy, it is necessary to have a large number of extremely accurate detections of the streams all across the sky complete with as much dynamical and statistical information as possible. This high level of accuracy and large number of statistics can be determined via the application of machine learning techniques.

1.5 Machine Learning

Machine learning is part of the artificial intelligence (AI) field of computer science. Explicitly, machine learning seeks to develop algorithms that can autonomously improve a result. In regards to AI, this would typically be the development of algorithms which seek to generate a better result in future actions based upon the results of actions taken in the past. This is the essence of machine learning: improving future results through the use of previous results. Machine learning can be broken down into two distinct types of learning: supervised and unsupervised.

Supervised learning refers to the development of algorithms that seek to learn a function via a set of training data. The task of the learner is therefore to predict the value of an underlying function for any valid point. Through the use of supervised learners it is possible to perform many tasks such as the classification of objects according to an underlying model and to perform such tasks as regression analysis. Examples of supervised learners are support vector machines (SVMs) and the maximum likelihood method.

Unlike supervised learning, the unsupervised learning paradigm refers to the development of algorithms that determine how a set of data is organized. An unsupervised learner is given no training data, but is simply given a set of data to effectively determine the underlying model. Unsupervised learners are often used in clustering problems and in independent or principle component analysis. Methods such as k-means clustering are unsupervised learners

1.5.1 The Method of Maximum Likelihood

The maximum likelihood method is a common statistical technique for fitting a mathematical model to a dataset. This method of model estimation seeks to determine the most likely parameter values given a set of data and an underlying probability model. Given a parameterized model and some input data generated according to that model it is possible to determine those parameters. Utilizing Bayesian statistics, this problem can be reconstructed as the determination of the a posteriori most likely parameters given the data and the model. The likelihood of a set of parameters is defined as the probability of obtaining a specific data set for a given set of model parameters. Utilizing Bayes' theorem, the a posteriori probability of a specific set of parameters, given the data and model, can be decomposed into two terms: the likelihood of the parameters and the prior probability of the parameters. It is common practice to assume that the prior probability distribution over the parameters is uniform. When this is the case, the a posteriori probability is proportional to the likelihood. Therefore, the maximum likelihood method can be used to determine the most likely model parameters given the data and the model. [81]

The maximum likelihood method can be decomposed into two distinct tasks: (1) the development and definition of the likelihood function to be used, and (2) the optimization over the parameters to find those that maximize the likelihood function given the data and the model. This latter task will be discussed in sections 2.2.1 and 2.2.2 while the likelihood function will be developed here. It is typically assumed, during the construction of a likelihood function, that the data points are independently generated; this means that the total likelihood of the dataset can be decomposed into the product of the likelihoods for each data point. The essence of the maximum likelihood method is the definition of a parameterized probability density function (PDF) that can be used to evaluate the probability of a data point given the model parameters.

A likelihood function for studying tidal streams within density space is developed here. The dataset is composed of stellar positions on the sky (l, b) and the apparent magnitude, g, which is related to the distance, R, given an estimate of the absolute magnitude, M_g. However, the nature in which the data is collected causes this distance to be poorly known. This is because the apparent magnitude is observed while the absolute magnitude can only be estimated through the use of models. Therefore, a PDF must be constructed that is a function of (l, b, g). Combining this PDF with the fact that each data point is independent, the likelihood of observing the data is the product of the likelihoods of observing each of the stars within the dataset, given the model:

$$\mathcal{L}(\vec{Q}) = \prod_{i=1}^{n} PDF(l_i, b_i, g_i | \vec{Q}), \tag{1.1}$$

where the index i runs over the n stars, $\vec{Q}$ is a vector representing the parameters in the model, and the probability density function (PDF) is a normalized version of the stellar density function that will be derived in section 2.1. The individual probabilities are small; therefore to avoid numerical underflow and achieve a higher level of numerical stability the standard practice of optimizing over the logarithm of the likelihood function

$$\frac{1}{n} \ln \mathcal{L}(\vec{Q}) = \frac{1}{n} \sum_{i=1}^{n} \ln PDF(l_i, b_i, g_i | \vec{Q}), \tag{1.2}$$

is adopted. The log-likelihood function is optimized over the same parameters. Section 2.1 discusses the details for combining the stellar density and data models and defines the PDF as well as the expansion of this PDF to include special cases that may arise in the data analysis (multiple tidal streams in a single dataset, and the need to remove specific sections from the probed volume).

CHAPTER 2

Methods and Algorithms

This chapter discusses all of the techniques, algorithms, and equations that are used to apply the maximum likelihood method to spatial stellar data. Some of the methods for the analysis of results from the optimizations, those that require the use of the stellar density models, are discussed here as well.

2.1 The Probability Density Function

The unique models are what differentiate maximum likelihood problems, for the models are what give a shape to the likelihood surface which is to be optimized over. In the instance of fitting tidal debris, there are two main models (tidal stream and stellar spheroid). These models describe the structures present within the data and combine to form the PDF. There are also two additional models (the absolute magnitude distribution and survey efficiency) which serve to model to the errors and other anomalous behavior that occurs within the data, through both natural means and those that arise due to assumptions in the structure models. These models and how they combine to form a usable PDF are described here.

2.1.1 The Tidal Stream Model

Tidal streams tend to have a complex path through the sky caused by the Galactic potential acting on the host structure as it is disrupted. The stars in the structures may also bunch up at apogalacticon, the point in the orbit farthest from the Galactic center, due to their lower velocity at this point in their orbit. It is also possible for the density of stars to have a complex cross-sectional density that varies with position along the stream. However, in a small volume through which the stream passes, such as in a single 2.5° wide SDSS stripe, it is reasonable to approximate the path of the stream as linear. Section 3.3 gives a detailed treatment of how reasonable this assumption is.

The stream is modeled in a piecewise linear fashion such that each stripe of

SDSS data that is analyzed has its own set of parameters for the tidal debris. The 2.5° degree wide stripes of the SDSS were chosen as the probed volume of the data, partly for easier integration of the SDSS data into the algorithm; however, the primary reason was to ensure the linearity of the stream within a given volume. In principle, the algorithm could be run on any 2.5° degree wide great circle on the sky by simply modifying the coordinate transformations necessary for converting from the SDSS great circle system to the more traditional Galactic coordinate system. In this piecewise manner, the stream is modeled as a cylinder with length that is limited by the edge of the data in one stripe. The cross section of this cylinder is axially symmetric with a density that falls off as a Gaussian distribution with distance from the cylinder axis. Figure 2.1 shows the shape of the data volume and the relationship between that volume and the tidal debris parameterized by the cylinder model.

The great circle coordinate system utilized by the SDSS is used here to measure the angular position on the sky. The μ coordinate measures the angular distance along the great circle swept out by each stripe. The angle across the stripe, ν, is defined to be zero at the mid plane of the stripe, with $-1.25^\circ < \nu < 1,25^\circ$. The inclination of each SDSS stripe is the maximum angle between that stripe and the celestial equator. Therefore, the angles (μ, ν) and the inclination of the stripe uniquely specify an angular position on the sky. A further discussion of the survey coordinates can be found in section 4.1.

The position of the cylinder center, and therefore the tidal stream, within a stripe is specified by the vector, $\vec{c}$. It is defined to point from the Galactic center to the axis of the cylinder. This vector would typically need three parameters to uniquely specify it; however, it is required that the position along the cylinder axis to which $\vec{c}$ points has $\nu = 0$ (lies in the mid plane of the data stripe), it is possible to reduce the number of needed parameters by one. Therefore, the stream position can be uniquely described by the radial distance distance from the sun, R (in kpc), and the angular position along the stripe, μ (in degrees). Thus, $\vec{c}(\mu,$ R) fixes the center point of a piece of tidal debris within an SDSS stripe and lies along the axis of the cylinder with which a segment of the tidal debris is modeled.

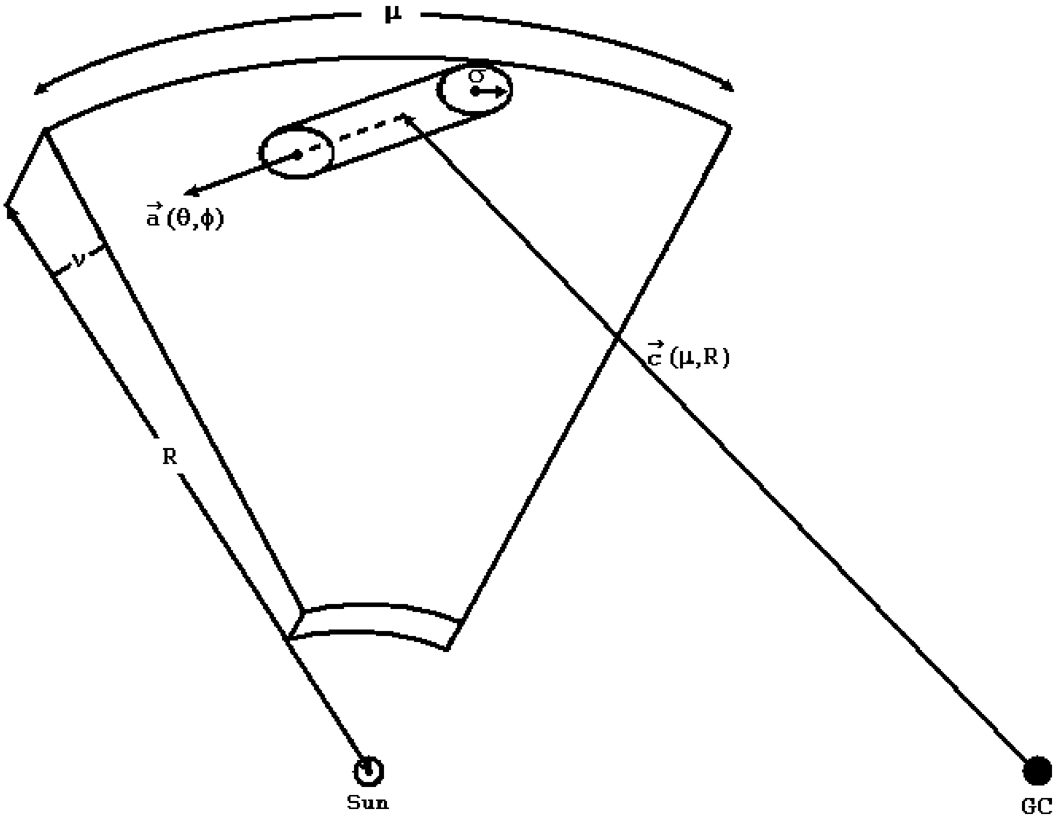

Figure 2.1: Stripe and stream parameter definitions. The segment of a stream which passes through an SDSS stripe is cylindrical within an individual stripe, with density that falls off as a Gaussian with distance from its axis. The coordinates μ, ν, and R are used to define SDSS stripes. These coordinates are adopted to define a vector, $\vec{c}(\mu, \nu = 0, R)$, which points to the center of the stream from the Galactic center. The stream directional vector $\hat{a}(\theta, \phi)$ is defined to be of unit length. Finally, the stream width, σ, is defined as the standard deviation of the Gaussian that defines the density fall off from the axis of the stream.

The orientation of the cylinder axis is defined by the unit vector $\hat{a}$. Again, three parameters would typically be needed to uniquely specify an orientation. However, since the length of the orientation vector is unity, the number of defining parameters is reduced by one. The vector, $\hat{a}$, is parameterized using the two angles θ and ϕ, both in radians. Here, θ is the angle between $\hat{a}$ and the Galactic Z-axis with Z perpendicular to the Galactic plane and towards the North Galactic Cap. The azimuthal angle ϕ is measured counterclockwise about the Z-axis, as viewed looking down on the Galaxy from the north Galactic pole, starting from the X-axis, which points in the direction from the Sun to the Galactic Center.

The width of the cylinder is described by the parameter, σ (in kpc). This width parameter is defined as the standard deviation of the Gaussian distribution that is used to describe the density fall off with distance from the cylinder axis. Thus, for a star with spatial coordinates given by $\vec{p}$, the distance, d, from the cylinder axis is given by

$$d = \mid (\vec{p} - \vec{c}) - \hat{a} * (\hat{a} \cdot (\vec{p} - \vec{c}) \mid . \tag{2.1}$$

In practice, this calculation is done by first converting each vector to a Galactocentric Cartesian coordinate system.

In summary, five parameters are needed to completed define a cylinder with Gaussian density fall off from the cylinder axis within a single 2.5° wide SDSS stripe: μ, R, θ, ϕ, and σ. Figure 2.1 graphically depicts the definition of these values with respect to the stripe volume. Through the use of these parameters, the stellar density of the stream at point $\vec{p}$ can be described as

$$\rho_{stream}(\vec{p}) \propto e^{-\frac{d^2}{2\sigma^2}}. \tag{2.2}$$

The normalization of this and the subsequent spheroid distribution will be considered once the entire PDF has been assembled.

2.1.2 The Stellar Spheroid Model

Here, the stellar spheroid is modeled with a Hernquist profile [82]. This is a modified power law defined as

$$\rho_{spheroid}(\vec{p}) \propto \frac{1}{r(r+r_0)^3}, \text{ where} \qquad (2.3)$$
$$r = \sqrt{X^2 + Y^2 + \frac{Z^2}{q^2}}.$$

Here X, Y, and Z are Galactocentric Cartesian coordinates. The coordinates X and Y are in the Galactic plane, with X directed from the Sun to the Galactic center and Y in the direction of the Solar motion. The coordinate Z is perpendicular to the Galactic plane and points in the direction of the North Galactic Cap. The stellar spheroid is thus defined by the two parameters, q and r_0 (in kpc). The dimensionless quantity q is a scaling factor in the Z-coordinate direction. This serves to make the stellar spheroid oblate ($q < 1$), spherically symmetric ($q = 1$), or prolate ($q > 1$). The parameter r_0 is a core radius that sets the scale of the Hernquist profile for at small $r, \rho \propto r^{-1}$ while at large $r, \rho \propto r^{-4}$. The Hernquist profile was chosen for the stellar spheroid model here, for it is a commonly used density function used to describe stellar and dark matter spheroids (halos).

There are many components of the Galaxy besides the spheroid. These include the bulge, bar, thick disk, and thin disk. All these components could, in principle, be used to create a complete Galactic model. However, due to the data being used with the algorithm, it is expected that contamination from these non-spheroid components is very low because the data is far from the plane of the Galaxy (where disk stars dominate) and the color-selected F turnoff stars used in this work are bluer than the turnoff of the thick disk stellar population, which is the component with the largest scale length. Therefore, most disk stars are excluded from the sample. An explicit discussion of the data used in this work can be found in section 4.1. It should also be noted that a global spheroid fit is not done within this work, thus it is only necessary to maintain a reasonable piecewise fit to the data.

2.1.3 The Absolute Magnitude Distribution Model

It is possible to utilize blue F turnoff stars as a standard candle[1] despite the fact that they do not occur at one distinct absolute magnitude. This is for the F turnoff stars can be described as a distribution that peaks at a specific absolute magnitude. By modeling this absolute magnitude distribution in blue F turnoff stars, it is therefore possible to make use of the large number of stars of this type.

If it were assumed that all color-selected stars have the same magnitude (at the mean value of the population) their estimated distances from the Sun would have a slight error causing any substructure in the spheroid to appear to be elongated along the line of sight. To account for this fact, the "observed" spheroid spatial density that is elongated along the line of sight is calculated by convolution of the model with the absolute magnitude distribution function along the line of sight.

The distribution of absolute magnitudes are modeled as a Gaussian with center of $\bar{M}_{g_0} = 4.2$ (the mean value of the blue F turnoff star population) and dispersion $\sigma_{g_0} = 0.6$. This distribution of the absolute magnitude distribution was determined through a simplification of the results found in [83]. Thus, the observed absolute magnitude, M_{g_0} is

$$M_{g_0} = \bar{M}_{g_0} + \Delta M_{g_0} \tag{2.4}$$

where $\bar{M}_{g_0} = 4.2$ and ΔM_{g_0} has a Gaussian distribution with zero mean and standard deviation 0.6. To account for this distribution in the absolute magnitudes, the probability of observing a star per unit apparent magnitude per unit solid angle is first derived, assuming all stars are of absolute magnitude $\bar{M}_{g_0} = 4.2$. This result is then convolved in apparent magnitude with a Gaussian of dispersion 0.6 centered at zero. The result is the probability of observing a star per unit apparent magnitude per unit solid angle, but with the absolute magnitude distribution taken into account.

Several density functions in different spaces will be needed, so to make this discussion more clear some definitions must first be described. The density $\rho_A(x)$ is defined as the density within the "A" coordinate space, while x refers to a generic

---

[1] For a discussion of standard candles please see Appendix A.

variable set in this space. Thus, six densities are defined as:

$$\rho_X(\vec{x}), \quad \rho_R(R,\Omega), \quad \rho_{g_{4.2}}(g_{4.2},\Omega), \quad \rho_{g_0}(g_0,\Omega), \quad \rho_{\mathcal{R}}(\mathcal{R}(g_0),\Omega), \quad \rho_{X_c}(\vec{x}), \tag{2.5}$$

where the first three densities describe the model in Cartesian, spherical, and apparent magnitude coordinate systems;

$$\rho_X(\vec{x}) = \frac{dV}{dxdydz}, \quad \rho_R(R,\Omega) = \frac{dV}{dRd\Omega}, \text{ and } \rho_{g_{4.2}}(g_{4.2},\Omega) = \frac{dV}{dg_{4.2}d\Omega}. \tag{2.6}$$

The densities that take into account the distribution on the absolute magnitude space are denoted by $\rho_{g_0}(g_0,\Omega), \rho_{\mathcal{R}}(\mathcal{R}(g_0),\Omega)$, and $\rho_{X_c}(\vec{x})$, where the subscript c stands for convolved. All coordinate systems are centered at the Sun, with Solar position assumed to be 8.5 kpc from the Galactic center, and the direction from the Sun to the Galactic center is in the positive X-direction. It should be noted that a distinction has been made between R and $\mathcal{R}$; R denotes the actual distance each star is from the Sun, while $\mathcal{R}(g_0)$ denotes the distance a star of apparent magnitude g_0 would appear if it had an absolute magnitude of $M_{g_0} = 4.2$. A distinction has also been made between g_0 and $g_{4.2}$. Here, g_0 denotes the actual reddening-corrected apparent magnitude of a star, while $g_{4.2}$ denotes the apparent magnitude a star at distance R would be calculated to have if it had an absolute magnitude $M_{g_0} = 4.2$. This convention is adopted for the remainder of this manuscript.

The Galactocentric Cartesian density, ρ_X is the actual spatial density of stars as described in equations 2.2 and 2.3 for the the stream and spheroid, respectively. The ultimate goal is to calculate ρ_{X_c}, the observed Galactocentric Cartesian density that is elongated along our line of sight which accounts for the Gaussian distribution, with dispersion ΔM_{g_0}, of absolute magnitudes. This density, ρ_{X_c} is obtained through the sequence of transformations

$$\rho_X(\vec{x}) \rightarrow \rho_R(R,\Omega) \rightarrow \rho_{g_{4.2}}(g_{4.2},\Omega) \rightarrow \rho_{g_0}(g_0,\Omega) \rightarrow \rho_{\mathcal{R}}(\mathcal{R}(g_0),\Omega) \rightarrow \rho_{X_c}(\vec{x}). \tag{2.7}$$

The relationship between these densities is determined by the transformations which take one coordinate space to the other. The $X \rightarrow R$ mapping is the well known spherical coordinate transform,

$$\rho_R(R,\Omega) = R^2\rho_X(\vec{x}). \tag{2.8}$$

If all of the stars had an absolute magnitude $M_{g_0} = 4.2$, then apparent magnitude would be measured as

$$\begin{aligned} g_{4.2} &= 4.2 + 5\log_{10}(\tfrac{R}{10pc}),\ \text{therefore} \\ R = \mathcal{R}(g_{4.2}) &= 10^{0.2(g_{4.2}-4.2-10)}\ (\text{kpc}),\ \text{and} \\ dR &= \tfrac{\ln 10}{5} R dg_{4.2}. \end{aligned} \tag{2.9}$$

Thus, the relationship between ρ_R and ρ_g is given by

$$\rho_{g_{4.2}}(g_{4.2},\Omega) = \frac{dg_{4.2}}{dR}\rho_R(R,\Omega) = \frac{\ln 10}{5}R^3\rho_X(\vec{x}) = \frac{\ln 10}{5}\mathcal{R}^3(g_{4.2})\rho_X(\vec{x}). \tag{2.10}$$

The measured g_0 magnitude is given by

$$g_0 = g_{4.2} + \Delta M_{g_0}. \tag{2.11}$$

Since g_0 is the sum of independent random variables, its density is the convolution of the two densities, i.e., we have that $\rho_{g_0}(g_0,\Omega) = \rho_g * \rho_{\Delta M_{g_0}}(g_0,\Omega)$, where the convolution is in the g-dimension. Thus,

$$\rho_{g_0}(g_0,\Omega) = \int_{-\infty}^{\infty} dg\ \rho_{g_{4.2}}(g,\Omega)\mathcal{N}(g_0 - g; u), \tag{2.12}$$

where $\mathcal{N}$ is the Gaussian density function given by:

$$\mathcal{N}(x;u) = \frac{1}{u\sqrt{2\pi}}e^{\frac{-x^2}{2u^2}}, \tag{2.13}$$

with $u = 0.6$. Switching back from apparent magnitude to spherical coordinates,

$$\rho_{\mathcal{R}}(\mathcal{R}(g_0),\Omega) = \frac{5}{\ln 10}\frac{\rho_{g_0}(g_0,\Omega)}{\mathcal{R}(g_0)}. \tag{2.14}$$

Since the coordinate spaces X_c and $\mathcal{R}$ are related by the spherical coordinate transformation, the results may now be collected and the convolved density ρ_{X_c} can be written in terms of ρ_X as follows:

$$\begin{aligned}
\rho_{X_c}(\vec{x}) &= \frac{1}{\mathcal{R}^2(g_0)}\rho_{\mathcal{R}}(\mathcal{R}(g_0),\Omega), \qquad (2.15)\\
&= \frac{5}{\mathcal{R}^3(g_0)\ln 10}\rho_{g_0}(g_0,\Omega),\\
&= \frac{5}{\mathcal{R}^3(g_0)\ln 10}\int_{-\infty}^{\infty} dg\ \rho_g(g,\Omega)\cdot\mathcal{N}(g_0-g;u),\\
&= \frac{1}{\mathcal{R}^3(g_0)}\int_{-\infty}^{\infty} dg\mathcal{R}^3(g)\cdot\rho_X(\vec{x}(\mathcal{R}(g),\Omega))\cdot\mathcal{N}(g_0-g;u),
\end{aligned}$$

where $(\mathcal{R}(g_0),\Omega)$ are the angular coordinates of $\vec{x}$.

The convolved stellar density function ρ_{X_c} has been derived, for a generic stellar density ρ_X, which could represent either the stream or the spheroid densities in their present context:

$$\begin{aligned}
\rho^{con}_{stream}(l,b,\mathcal{R}(g_0)) &= \frac{1}{\mathcal{R}^3(g_0)}\int_{-\infty}^{\infty} dg\mathcal{R}^3(g)\cdot \qquad (2.16)\\
&\quad \rho_{stream}(l,b,\mathcal{R}(g_0))\cdot\mathcal{N}(g_0-g;u)
\end{aligned}$$

and

$$\begin{aligned}
\rho^{con}_{spheroid}(l,b,\mathcal{R}(g_0)) &= \frac{1}{\mathcal{R}^3(g_0)}\int_{-\infty}^{\infty} dg\mathcal{R}^3(g)\cdot \qquad (2.17)\\
&\quad \rho_{spheroid}(l,b,\mathcal{R}(g_0))\cdot\mathcal{N}(g_0-g;u).
\end{aligned}$$

In practice, the convolution is performed separately on the stream and spheroid densities, to compute the function $\rho^{con}_{stream}(l,b,\mathcal{R}(g_0))$ and $\rho^{con}_{spheroid}(l,b,\mathcal{R}(g_0))$. The convolution integral is calculated numerically using the technique of Gaussian quadrature. Gaussian quadrature is a quadrature rule in which an n point rule yields the exact result of a polynomial of degree $2n-1$ through the suitable choice of the evaluation points x_i and corresponding weights w_i. A detailed description of the Gaussian quadrature technique can be found in [84].

2.1.4 The Combined Probability Density Function

The complete PDF with the combination of the stream and spheroid densities can now be computed. To do this, the following quantities are required: the stellar densities for the stream and spheroid, as derived in section 2.1.3; the volume over which the density is defined; the detection efficiency for finding stars as a function of apparent magnitude; and a normalization factor to describe the fraction of stars in each of the two components, which will be defined as the parameter ϵ.

The detection efficiency is a result of the SDSS being a magnitude limited survey. In a magnitude limited survey the survey finds all stars out to a certain magnitude limit, however this includes really bright things that have large distances, as well as dim objects that are very close. Therefore, the closer an object is to the magnitude limit, the higher the chance that the object is not detected at all. Therefore a detection efficiency function, $\mathcal{E}$, describes the percentage of stars detected at a given magnitude. In Figure 2 of [39] the authors present measurements for the detection efficiency of the SDSS at various magnitudes. These measurements were fit using a sigmoid curve and resulted in the efficiency function

$$\begin{aligned} \mathcal{E}(g_0) &= \frac{s_0}{e^{s_1(g_0 - s_2)} + 1}, \text{ where} \\ \vec{s} &= (0.9402, 1.6171, 23.5877), \end{aligned} \tag{2.18}$$

and $\vec{s}$ is the vector of parameters $s0, s1, \text{and} s2$.

The dimensionless normalization parameter, ϵ, defines the fraction of stars in the data that are in the stream and the fraction that are in the spheroid. A separate normalization parameter, ϵ, is measured for each stripe of data. Therefore, the value of ϵ for a given stripe gives only the relative number of stars that comprise the stream as compared to the smooth spheroid for that dataset and does not measure the fraction of stars in the stream as a function of position within the Galaxy.

The concept of constrained and unconstrained variables is introduced here. Instead of explicitly using ϵ to define the fraction of stars within the stream, a new variable f has been defined as just this, while $1 - f$ defines the fraction of stars within the spheroid. If this were not the case, the likelihood would need to be maximized subject to the constraint that the parameter ϵ be between zero and one. To avoid this constraint, the unconstrained value of ϵ is used. The fraction of stars within the stream is therefore defined as

$$f_{stream} = \frac{e^{\epsilon}}{1+e^{\epsilon}}. \tag{2.19}$$

Similarly, the fraction of stars within the spheroid is

$$f_{spheroid} = 1 - f_{stream} = \frac{1}{1+e^{\epsilon}}. \tag{2.20}$$

According to this definition, if ϵ is ∞ all stars are part of the stream, if ϵ is $-\infty$ all stars are part of the spheroid, and if ϵ is zero then the stars are split equally amongst the stream and spheroid. All other parameters used are naturally unconstrained and do not require a similar treatment.

Eight parameters are thus needed to fit a piece of tidal debris within a stellar spheroid utilizing the models described previously: five for the stream $(\mu, R, \theta, \phi, \sigma)$, two for the spheroid (q, r_0), and the normalization parameter ϵ. The union of these eight parameters define the parameter vector $\vec{Q}$.

Thus, the PDF is given by

$$\begin{aligned} PDF(l,b,\mathcal{R}(g_0)|\vec{Q}) \quad = \quad & \frac{e^{\epsilon}}{1+e^{\epsilon}} \frac{\mathcal{E}(\mathcal{R}(g_0))\rho^{con}_{stream}(l,b,\mathcal{R}(g_0)|\vec{Q})}{\int \mathcal{E}(\mathcal{R}(g_0))\rho^{con}_{stream}(l,b,\mathcal{R}(g_0)|\vec{Q})dV} \\ & + \frac{1}{1+e^{\epsilon}} \frac{\mathcal{E}(\mathcal{R}(g_0))\rho^{con}_{spheroid}(l,b,\mathcal{R}(g_0)|\vec{Q})}{\int \mathcal{E}(\mathcal{R}(g_0))\rho^{con}_{spheroid}(l,b,\mathcal{R}(g_0)|\vec{Q})dV}, \end{aligned} \tag{2.21}$$

where the integrals are taken over the entire volume probed by the input dataset.

These integrals cannot be solved analytically for our function, thus a numerical technique must be used. First, an integration mesh is defined which divides the total volume along each dimension $(\mu, \nu, \text{and} g)$ into many small wedge shaped volumes. The edges of the volume elements are fixed along constant $\mu, \nu, \text{and} g$. Then, the center of each sub-volume is found and the values for the stream and spheroid probabilities calculated at those points, using the density functions derived in section 2.1.3. The volume of each sub-volume is then calculated and this is multiplied by its respective stream and spheroid probabilities to calculate the contribution of the sub-volume to the stream and spheroid integrals. Finally, the contribution of the sub-volumes to the stream and spheroid integrals is summed over all sub-volumes calculate the total stream and spheroid integrals, respectively. The bounds of the volumes used within the numerical integration are set to correspond exactly with that of the data set analyzed.

2.1.5 Removing Sections from the Volume

It is necessary to provide a means to remove sections from the probed volume. There are many instances when this may be needed. It is possible that artifacts exist within the data. There may also be sections of data missing due to observation effects such as poor seeing. It is also possible that a section of data may be removed because it may influence the optimization of the algorithm. For example a globular cluster is a dense grouping of stars within a very small volume. Should the algorithm be left to fit a dataset with a structure like this, the algorithm may calculate inaccurate values, for the globular cluster would not exist within the models. Thus it may be desired to simply remove all tightly bound structures of this type. However, the corresponding volume must also be removed from the optimization for the lack of stars within that part of the volume could cause inaccuracies in the calculation of the maximum likelihood parameters. Therefore, it would be useful to be able to remove these sections devoid of stars, either due to absent or removed data, from the probed volume as well.

In theory, it is a simple task to remove the unwanted sections from the volume of a numerical integral. Since the numerical integral is defined as the sum of all sub-volumes, it is simply a matter of not adding the unwanted sub-volumes into the sum. Upon inspection, however, this becomes troublesome in that it requires the unwanted sections to exactly correspond with the sub-volumes. This must be so in order to avoid any over(under)lapping which would inaccurately remove the affected volume. It is therefore a better solution to actually subtract the results of the unwanted sections from the total volume.

The procedure for removing an unwanted section of the volume is as follows.

First, calculate the integrals over the total volume as previously defined, let this be $\vec{\mathcal{I}}^{tot}$ containing the spheroid and stream integrals, respectively. Where

$$\vec{\mathcal{I}}^{tot} = (\int \mathcal{E}(\mathcal{R}(g_0))\rho^{con}_{spheroid}(l, b, \mathcal{R}(g_0)|\vec{Q})dV, \int \mathcal{E}(\mathcal{R}(g_0))\rho^{con}_{stream}(l, b, \mathcal{R}(g_0)|\vec{Q})dV). \tag{2.22}$$

Then, calculate the integrals over the volume that is to be removed, let this be $\vec{\mathcal{I}}_{cut}$. In practice, the integral over the volume to be removed must be of a finer granularity than that over the total volume. Therefore, $\delta\mu_{cut} < \delta\mu, \delta\nu_{cut} < \delta\nu,$ and $\delta g_{cut} < \delta g$. This, however, is only the lower bound and a much finer granularity should be used to ensure an accurate calculation of $\vec{\mathcal{I}}^{cut}$. The final volume can then be calculated as

$$\vec{\mathcal{I}}^{fin} = \vec{\mathcal{I}}^{tot} - \vec{\mathcal{I}}^{cut}. \tag{2.23}$$

This technique can be expanded to an arbitrary number of removed volumes, j, by simply removing all subsequent volumes as in the same manner. Therefore, the final integrals over the volume after removing an arbitrary number of sections would be

$$\vec{\mathcal{I}}^{fin} = \vec{\mathcal{I}}^{tot} - \sum_{i=0}^{j} \vec{\mathcal{I}}^{cut_i}, \tag{2.24}$$

where $\vec{\mathcal{I}}^{cut_i}$ is the i^{th} volume to be removed of j total volumes to be removed. This modification to the integral can thus be added to the PDF

$$\begin{aligned} PDF(l, b, \mathcal{R}(g_0)|\vec{Q}) &= \frac{e^\epsilon}{1+e^\epsilon}\frac{\mathcal{E}(\mathcal{R}(g_0))\rho^{con}_{stream}(l, b, \mathcal{R}(g_0)|\vec{Q})}{\mathcal{I}^{fin}_{stream}} \\ &+ \frac{1}{1+e^\epsilon}\frac{\mathcal{E}(\mathcal{R}(g_0))\rho^{con}_{spheroid}(l, b, \mathcal{R}(g_0)|\vec{Q})}{\mathcal{I}^{fin}_{spheroid}}, \end{aligned} \tag{2.25}$$

where $\mathcal{I}_{fin_{stream}}$ denotes the stream (second) component of $\vec{\mathcal{I}}$ and similarly $\mathcal{I}_{fin_{spheroid}}$ denotes the spheroid (first) component of $\vec{\mathcal{I}}$.

2.1.6 Multiple Pieces of Tidal Debris

Another useful addition to the algorithm is the ability to fit multiple pieces of tidal debris within a single dataset. It is conceivable and quite common for there to be multiple pieces of substructure within a single stripe of data. In some instances it could be possible to remove the additional structures and utilize the method described in section 2.1.5; however, this will not always be possible, nor will it always be the best course of action. Thus, the PDF must be expanded again to account for the addition of fitting multiple streams.

The addition of simultaneously fitting an additional stream is accomplished as follows. The procedure can later be expanded to an arbitrary number of streams. First, an additional component must be added to the PDF to account for the second stream and will have a structure mimicking that of the original stream. This means that an additional integral must be calculated for this stream

$$\begin{aligned}\vec{\mathcal{I}} = (\int \mathcal{E}(\mathcal{R}(g_0))\rho^{con}_{spheroid}(l, b, \mathcal{R}(g_0)|\vec{Q})dV, \\ \int \mathcal{E}(\mathcal{R}(g_0))\rho^{con}_{stream_1}(l, b, \mathcal{R}(g_0)|\vec{Q})dV, \\ \int \mathcal{E}(\mathcal{R}(g_0))\rho^{con}_{stream_2}(l, b, \mathcal{R}(g_0)|\vec{Q})dV)).\end{aligned} \tag{2.26}$$

where $\vec{\mathcal{I}}$ now contains three components, one for the spheroid and one for each stream. An additional normalization factor is needed to accommodate the new stream. Therefore, there will be an additional 6 parameters that need to be fit to completely parameterize the new stream and normalize it with the other components properly. The new normalization factors are

$$\begin{aligned} f_{stream_1} &= \frac{e^{\epsilon_1}}{1 + e^{\epsilon_1} + e^{\epsilon_2}} \\ f_{stream_2} &= \frac{e^{\epsilon_2}}{1 + e^{\epsilon_1} + e^{\epsilon_2}} \\ f_{spheroid} &= \frac{1}{1 + e^{\epsilon_1} + e^{\epsilon_2}} \end{aligned} \tag{2.27}$$

where ϵ_1 and ϵ_2 denote the value of ϵ corresponding to the first and second stream, respectively.

Combining these changes and generalizing to an arbitrary number of streams,

k, the PDF becomes

$$\begin{aligned} PDF &= \sum_{i=1}^{k}\left[\frac{e^{\epsilon_i}}{(1+\sum_{j=1}^{k} e^{\epsilon_j})}\frac{\rho^{con}_{stream}(l,b,\mathcal{R}(g_0)|\vec{Q}_{stream_i})}{\mathcal{I}_{stream_i}}\right] \\ &+\frac{1}{(1+\sum_{i=1}^{k}\epsilon_i)}\frac{\rho^{con}_{spheroid}(l,b,\mathcal{R}(g_0)|\vec{Q}_{spheroid})}{\mathcal{I}_{spheroid}}, \end{aligned} \tag{2.28}$$

where i and j denote the i^{th} and j^{th} stream of k total streams, and $\mathcal{I}_{stream_i}$ denotes the i^{th} stream component (or the $(i+1)^{th}$ of $\vec{\mathcal{I}}$.

2.1.7 The Complete Probability Density Function

It is now possible to construct a complete PDF which contains the most likely situations which may arise during data analysis. This can be accomplished by merging the PDFs from equations 2.25 and 2.28. Therefore, let

$$\begin{aligned} f_{stream_i} &= \frac{e^{\epsilon_i}}{1+\sum_{j=1}^{k}[e^{\epsilon_j}]} \\ f_{spheroid} &= \frac{1}{1+\sum_{j=1}^{k}[e^{\epsilon_j}]} \end{aligned} \tag{2.29}$$

where i and j denote the i^{th} and j^{th} stream, respectively, of k total streams. Also let

$$\vec{\mathcal{I}}^{com} = (\mathcal{I}^{fin}_{spheroid}, \mathcal{I}^{fin}_{stream_i}), \tag{2.30}$$

where $\vec{\mathcal{I}}^{com}$ is a $k+1$ length vector composed of a spheroid integral component and k stream integral components. Here, $\mathcal{I}^{fin}_{spheroid}$ refers to the spheroid (1^{st}) component of $\vec{\mathcal{I}}^{fin}$ defined in equation 2.24, and $\mathcal{I}^{fin}_{stream_k}$ refers to the i^{th} stream (or $(i+1)^{th}$ total) component of $\vec{\mathcal{I}}^{fin}$ defined in equation 2.24. The superscript of *com* here denotes complete.

The above can now be substituted into the combined PDF defined in equation 2.21 to get a complete PDF

$$PDF = \sum_{i=1}^{k}\left[P_{stream_i}\frac{\rho^{con}_{stream}(l,b,\mathcal{R}(g_0)|\vec{Q}_{stream_i})}{\mathcal{I}^{com}_{stream_i}}\right]$$

$$+P_{spheroid}\frac{\rho^{con}_{spheroid}(l,b,\mathcal{R}(g_0)|\vec{Q}_{spheroid})}{\mathcal{I}^{com}_{spheroid}}, \tag{2.31}$$

where i and j denote the i^{th} and j^{th} stream of k total streams, $\mathcal{I}^{com}_{spheroid}$ denotes the spheroid (1^{st}) component of $\vec{\mathcal{I}}^{com}$, and $\mathcal{I}^{com}_{stream_i}$ denotes the i^{th} stream component (or the $(i+1)^{th}$ total component) of $\vec{\mathcal{I}}^{com}$.

2.2 Optimization

Given a likelihood function (equation 1.2), a PDF to utilize that likelihood function (equation 2.31), and an optimization technique to traverse the parameter space, it is possible to find the optimum parameters for the models given the data. This section describes the optimization techniques used to find this optimum parameter set, and will also discuss the computational complexity of the problem.

2.2.1 Conjugate Gradient Technique

Gradient methods are a group of well known and studied optimization techniques including the techniques of steepest descent, coordinate descent, and conjugate gradient. All of these techniques are iterative and local methods of functional minimization/maximization. "Iterative" means each successive step within the algorithm is dependent upon the last, in contrast to asynchronous algorithms which have no strict "arrow of time" dependence. "Local" means the algorithm only has knowledge of the parameter space directly around the current point, unlike global optimization methods which are able to probe the entire parameter space equally. Gradient methods work by determining the optimum direction in which the current evaluation point should move in order to increase in "goodness of fit." Thus, the point is moved along the gradient direction and a new direction is calculated at this new evaluation point. This results in a new direction to be traversed, and the process is repeated until convergence. A further discussion of gradient methods can be found in [81]. In the instance of the tidal stream problem, the conjugate gradient method was implemented. This method was chosen because the likelihood function is well-behaved and therefore well suited to gradient methods, and the conjugate gradient method tends to have the fastest convergence rate of the gradient methods.

The conjugate gradient method utilizes a fixed point gradient calculation. This is accomplished by perturbing the current parameter value, Q_i, by a small amount, h_i, henceforth referred to as the step size of the gradient. The function is then evaluated again using the new parameter $(Q_i + h_i)$. Utilizing the function value at the original point and at this perturbed point it is then possible to calculate i^{th} component of the gradient direction as

$$G_i = \left. \frac{\mathcal{L}(Q_i + h_i) - \mathcal{L}(Q_i)}{h_i} \right|_{\text{all other } Q_j \text{ fixed}}, \tag{2.32}$$

where $\mathcal{L}(\vec{Q})$ is the evaluation of the likelihood function with parameters $\vec{Q}$, Q_i denotes the i^{th} component of the parameter vector, and h_i is the step size corresponding to the i^{th} parameter. For the tidal stream problem, a double sided gradient calculation has been implemented. This involves twice perturbing the parameter by the step size: once as obtain $Q_i + h_i$ and again to obtain $Q_i - h_i$. The function is then evaluated at both these new points and the evaluation values used to generate i^{th} component of the gradient direction as

$$G_i = \left. \frac{\mathcal{L}(Q_i + h_i) - \mathcal{L}(Q_i - h_i)}{2h_i} \right|_{\text{all other } Q_j \text{ fixed}}, \tag{2.33}$$

where the denominator has become $2h_i$ since the distance between the evaluated points has doubled. This gradient vector is then used to define a directional vector $\vec{D}$ as

$$\vec{D} = \vec{G}. \tag{2.34}$$

The positive value of the gradient is used in order to maximize the value of the likelihood function. In the steepest descent method, the parameters are then updated using this direction, and the process repeated. In the conjugate gradient method, the above direction is used for only the first iteration of the algorithm. For all subsequent iterations, the direction searched is conjugate to the direction searched in the previous iteration, and therefore conjugate to all previous directions searched.

Two vectors, u and v are conjugate with respect to a matrix, $\mathbf{A}$, if

$$\vec{u}^T \mathbf{A} \vec{v} = 0. \tag{2.35}$$

In the special case that $\mathbf{A} = \mathbf{I}$, where $\mathbf{I}$ is the Identity matrix, conjugate vectors are orthogonal. This condition maintains that all directions are non-interfering and, in general, is found to dramatically increase the speed of functional optimization.

The conjugate to previous directions can be found through the use of a multiplier, B_i, based upon the current gradient vector and the previous gradient vector. Thus,

$$B_i = \frac{\vec{G}_i \cdot (\vec{G}_i - \vec{G}_{i-1})}{\vec{G}_{i-1}^2}, \tag{2.36}$$

where B_i is the multiplier for iteration i, $\vec{G}_i$ denotes the gradient vector for iteration i, and $\vec{G}_{i-1}$ is the gradient vector from the $(i-1)^{th}$ iteration. This value can then be used to calculate the new directional vector

$$\vec{D}_i = \vec{G}_i + B_i * \vec{D}_{i-1}, \tag{2.37}$$

where D_i is the directional vector for iteration i, $\vec{G}_i$ is the gradient vector determined for iteration i, B_i is the multiplier calculated for iteration i, and $\vec{D}_{i-1}$ is the direction vector from iteration $(i-1)$. It should be noted that it is common practice to occasionally reset the direction back to the pure gradient direction. This is for after a number of iterations the directions begin to lose conjugacy because no direction exists that is completely non-interfering with all previous directions. This can result in a slower convergence rate. The standard reset occurs when the iteration number is a multiple of the dimensionality of the function, or the number of parameters being fit with the technique. This practice is adopted here.

The above formulas are thus combined to construct an iterative procedure for the conjugate gradient. First, the search is initiated with an initial set of parameters. The gradient vector is populated using the appropriate step sizes and the direction found using equation 2.34. The parameters are then changed along this direction, and the iteration ends. For the second iteration, the gradient vector is again populated, however the direction is now calculated using equation 2.37. The parameters are again updated by moving them along the directional vector, and the second iteration ends. The optimization then continues in this manner of using the conjugate directions until convergence while resetting to the gradient direction every $\mathcal{N}$ iterations, where $\mathcal{N}$ is the number of parameters being optimized over. Here, convergence is achieved when all components of the gradient vector fall below a preset value, thus when the gradient becomes too flat. For all optimizations reported in this manuscript, a value of $max(g_i) < 0.00001$ has been used as a convergence condition, where $max(g_i)$ denotes the maximum component over all components of the gradient vector.

The step size, h_i, is uniquely defined for each parameter. This is because of the large variety of parameters that occur within the models and are all on differing scales. If the step size is too large, the gradient will be an inaccurate representation of the local parameter space. If the step size is too small, numerical errors may occur in the calculation of several numerical integrals which could introduce noise into the parameter space. These errors would exhibit as incorrect directions in the search algorithm which could cause the optimization to take much longer than needed or completely fail altogether. The independently chosen step sizes are tabulated in Table 2.1. These values were derived under two considerations. First, a series of gradient vectors were calculated using differing step sizes. This allowed for the change in the gradient to be observed as a function of step size. Also, the parameter space was examined through the generation of parameter distribution plots which showed the likelihood function value versus the parameter value. Combining these two methods, a value for the step size of each parameter was determined that would be small enough to provide a very accurate gradient calculation, yet large enough to overcome any numerical anomalies that may occur in the behavior of the parameters distribution.

2.2.2 Line Search Technique

After the conjugate gradient method determines the search direction for the current iteration, a line search determines the optimal distance along that direction

Table 2.1: Perturbation values used for the gradient and Hessian

Parameter	Step Size (h)
q.............	$4 \cdot 10^{-6}$
r_0 (kpc)...	$8 \cdot 10^{-4}$
ϵ..............	$1 \cdot 10^{-6}$
μ (deg).....	$3 \cdot 10^{-5}$
R (kpc)....	$4 \cdot 10^{-5}$
θ (rad).....	$6 \cdot 10^{-5}$
ϕ (rad).....	$4 \cdot 10^{-5}$
σ (kpc).....	$4 \cdot 10^{-6}$

that should be moved. The line search technique seeks to determine the value, α, that maximizes the function

$$\Phi(\alpha) = \mathcal{L}(\vec{Q}_k + \alpha\vec{D}_k), \tag{2.38}$$

where $\vec{D}_k$ is the search direction at iteration k and $\vec{Q}_k$ vector of parameters at iteration k. After determining the α^* which maximizes $\Phi(\alpha)$, an update over the parameters is performed

$$\vec{Q}_{k+1} \longleftarrow \vec{Q}_k + \alpha^*\vec{D}_k \tag{2.39}$$

which determines the initial point for the $(k+1)^{th}$ iteration.

A begin the line search, a bracketing method is first employed to ensure that a maximum of the function is within the range being searched. This is done by determining a range over which the center of three points has a greater likelihood than the other two. In this way, an initial set of three points are used at zero, one, and two times the length of the directional vector, $\vec{D}_k$. The likelihood is then evaluated at these three points. Should the center of these three points have a likelihood that is not greater than the other two, the endpoint with the greater likelihood becomes the new center point, while the center becomes a new endpoint, and a new second endpoint is calculated by expanding along the range to two times the current expansion factor, along the search direction. Iteration of the bracketing method continues in this manner until the center point is found to have the greatest likelihood of the three points.

The three points calculated during the bracketing process are then passed to the line search algorithm proper which uses them to fit a parabolic function and determine its peak. This is done by performing likelihood evaluations along the search direction and iterates as follows: initially a guess is made for the value of α by fitting a parabola via the calculation:

$$\begin{aligned} u &= a_1^2 * (L_2 - L_3) + a_2^2 * (L_3 - L_1) + a_3^2 * (L_1 - L_2), \\ b &= a_1 * (L_2 - L_3) + a_2 * (L_3 - L_1) + a_3 * (L_1 - L_2), \\ \alpha &= 0.5 * \frac{u}{b}, \end{aligned} \tag{2.40}$$

where a_1, a_2, and a_3 are the factors multiplied by the current direction that produce the parameters with likelihood L_1, L_2, and L_3, respectively. The initial line search iteration sets the values a_1, a_2, and a_3 to the values returned from the bracketing method. α is then the current guess for the value to maximize equation 2.38. The likelihood L_α is then calculated using the parameters generated using equation 2.39 assuming $\alpha = \alpha^*$. The new order of the three points is:

$$\begin{aligned} &\text{if} : \alpha > a_2 \text{ and } L_\alpha > L_2; \text{then} : 1, 2, \alpha, \\ &\text{if} : \alpha > a_2 \text{ and } L_\alpha < L_2; \text{then} : 2, \alpha, 1, \\ &\text{if} : \alpha < a_2 \text{ and } L_\alpha > L_2; \text{then} : \alpha, 2, 3, \\ &\text{if} : \alpha < a_2 \text{ and } L_\alpha < L_2; \text{then} : 1, \alpha, 2. \end{aligned} \tag{2.41}$$

In short, the distance along the search direction is reduced based upon the value of α and its corresponding likelihood. These new points are then used to calculate a new guess for α using equations 2.40, 2.41, and 2.39. Iteration continues until convergence, where the difference between subsequent α calculations drops below a preset value. If the line search determine a move that is smaller than a preset tolerance, the algorithm discontinues execution, for there was a negligible movement. If this occur during a step using a conjugate direction, the algorithm continues for one additional iteration utilizing the gradient direction as the search direction in order to determine if further optimization is possible.

2.2.3 Run Time and Distributed Computing

The numerical integrals that must be calculated within the likelihood function dominate the runtime of the algorithm. A typical dataset contains approximately 100,000 stars, while testing has shown the volume integral requires a minimum of 1.4 million subvolumes to be produce good scientific results, and the convolution integral requires a minimum of 30 points to accurately fit the absolute magnitude distribution reasonably. The minimum number of model evaluations per likelihood calculation is

$$\mathcal{Z} = \gamma\Gamma + n, \tag{2.42}$$

where γ is the number of points used in the convolution integral, Γ is the number of points used in the volume integral, n is the total number of stars in the dataset, and $\mathcal{Z}$ is the total number of model evaluations per likelihood calculation. Therefore, in determining the likelihood, there exists a trade-off between the accuracy of that likelihood evaluation and the time it takes to do the evaluation. The largest contributer to this runtime is the volume integral; however, increasing the precision of this integral leads to polynomially longer calculation times (scaling as δ^3).

Utilizing the minimum values stated above ($\gamma = 30$, $\Gamma = 1,400,000$) and assuming a dataset of size $n = 100,000$ a single likelihood calculation on a single processor will take approximately one minute (optimizing using a single stream and no volume removed). A single conjugate gradient optimization will take anywhere from 100-1,000 iterations, with an estimated twenty-five likelihood calculations per iteration, thus an average of 12,500 likelihood evaluations can be expected. Therefore, at one minute an evaluation an estimated 12,500 minutes, or approximately 200 days, would be required for a single optimization on a single processor. Clearly parallel processing is required to make progress on the science.

2.2.4 A Generic Maximum Likelihood Evaluator

A generic maximum likelihood evaluator (GMLE[2]) has been developed with the tidal stream application as its flagship test application. [85] Through the use of the GMLE package the tidal stream algorithm is able to use a number of computational architectures and environments: including a homogeneous cluster, a heterogeneous grid of clusters, the highly connected environments of a supercomputer, and even the extremely disconnected environment of volunteer computing on the worldwide scale.

The GMLE package has been developed in two frameworks: the Simple Actor Language System and Architecture (SALSA) distributed language which utilizes an actor-oriented structure and leverages the ubiquitousness of the Java environment to create heterogeneous grids for use as a distributed computing environment [86]; and the message passing interface (MPI) library designed for use in homoge-

---

[2] GMLE has been made publicly available. The download and information regarding its use can be found at http://wcl.cs.rpi.edu/gmle.

neous workstation clusters as well as massively parallel computational environments (i.e. supercomputers). [87] Through the use of the GMLE packages, the computational requirements needed by the tidal stream algorithm have been fulfilled and the enormous runtimes have been dramatically reduced. Utilizing 88 nodes on the Rensselaer Grid results in a speedup of approximately 65 times over the single processor. Through the use of 512 nodes an IBM BlueGene/L system[3] a speedup of approximately 150 times was seen over the single processor. A complete optimization can now be performed in a matter of hours in the supercomputing environment or a few days in the grid environment. It should be noted that the communication time for this application is very low, with the total communication time making up less than ten percent of the total runtime. Also, the scalability of the application is quite apparent in that the number of identical probability evaluations within the algorithm create an extremely data parallel environment which may be exploited through the use of larger numbers of nodes. Through the use of more precise integral calculations, both volume and convolution, an even higher degree of scalability will be achieved given the larger number of evaluation points. This is, of course, assuming a relatively fixed communication time. These increases in the number of evaluation points would serve to reduce the amount of numerical error observed in the algorithm. This reduced error would therefore provide more accurate scientific results, to a point.

The GMLE MPI package has also been developed to utilize the Berkeley Open Infrastructure for Network Computing (BOINC) Internet computing framework. [88] This framework allows for worldwide volunteer computing in which users donate computational resources by downloading the BOINC client and attaching the desired project. The BOINC application MilkyWay@home[4], has been created, so anyone can donate resources toward the tidal stream algorithm. The alpha stage project currently is maintaining approximately 16,350 users, spanning over 130 countries,

---

[3] The BlueGene/L used for these tests and the majority of the results presented in this manuscript is housed and maintained at the Computational Center for Nanotechnology Innovations (CCNI) which is based on the Rensselaer Polytechnic Institute campus and at the Rensselaer Technology Park

[4] Information regarding the use of MilkyWay@home and the projects current status can be found at http:
milkyway.cs.rpi.edu.

and donating approximately 43,850 hosts. This equates to an average of 103.425 TeraFLOPS placing the MilkyWay@home project at spot 17 on the top 500 computers November 2008 list[5]. Since the BOINC infrastructure is naturally asynchronous, the MilkyWay@home project has implemented many asynchronous optimization techniques to take advantage of this unique environment. None of the results provided by these techniques were used in the analyses presented in this manuscript.

2.3 Analysis Methods

In this section, the method of statistical error analysis developed and implemented for use with the tidal stream algorithm is presented. Also, the probabilistic method for separating stars into a separate catalog for each structure that fits the density profile of that structure is defined.

2.3.1 Errors in the Estimated Parameter Values

The utilization of a gradient method for optimization places a limit on the accuracy of the final parameter estimates returned by the optimization. This accuracy depends upon the shape of the likelihood surface at its maximum. The shape of the surface is, in turn, governed by the number of stars within the input catalog used in optimization. The fewer stars within the catalog the wider the peak will be at the maximum and also the larger the statistical error. The error is also affected by the accuracy with which the maximum can be numerically determined. This latter point will be discussed in section 3.2.1 during the discussion of an analysis of a simulated dataset. A discussion of the method for determining the achievable accuracies and estimated errors regarding the shape of the likelihood surface will be presented here.

The error in each parameter is estimated by assuming the likelihood surface is well approximated as a Gaussian near the maximum. First, the Hessian matrix, **H**, of the parameters is calculated. The Hessian matrix is a square matrix of second-order derivatives of the likelihood function in which each element denotes one of all possible second-order partial derivatives. The Hessian matrix can be computed

---

[5] Information regarding the top 500 supercomputers list can be found at http://www.top500.org. The November 2008 list can be found at http://www.top500.org/list/2008/11/100.

numerically using a finite difference formula, similar to that used in the conjugate gradient method

$$\begin{aligned} H_{ij} &= \frac{H_{ij}^1 - H_{ij}^2 - H_{ij}^3 + H_{ij}^4}{4h_i h_j}, \text{ where,} \\ H_{ij}^1 &= \mathcal{L}(Q_j + h_j, Q_i + h_i)|_{\text{all other } Q_k \text{ fixed}}, \\ H_{ij}^2 &= \mathcal{L}(Q_j - h_j, Q_i + h_i)|_{\text{all other } Q_k \text{ fixed}}, \\ H_{ij}^3 &= \mathcal{L}(Q_j + h_j, Q_i - h_i)|_{\text{all other } Q_k \text{ fixed}}, \\ H_{ij}^4 &= \mathcal{L}(Q_j - h_j, Q_i - h_i)|_{\text{all other } Q_k \text{ fixed}}, \end{aligned} \tag{2.43}$$

where Q_j is the j^{th} component of parameter vector $\vec{Q}$, Q_i is the i^{th} component of parameter vector $\vec{Q}$, h_j is the step size for the j^{th} parameter of Q_j, and h_i is the step size for the i^{th} parameter of Q_i. In practice, the step sizes, h_k, which are used here are the same as that used in the finite difference gradient calculation found in table 2.1.

If the Hessian matrix is negative/positive definite then the point at which the Hessian is evaluated at is a local maximum/minimum. If after optimizing over a given dataset a maximum has been achieved, then the evaluated Hessian matrix should be negative definite. A variance matrix, $\mathbf{V}$, can then be constructed using the inverse of the Hessian matrix and the number of stars in the dataset, n:

$$\mathbf{V} = \frac{1}{n}\mathbf{H}^{-1}, \tag{2.44}$$

where $\mathbf{H}^{-1}$ denotes the inverse of the Hessian matrix, and the matrix values are scaled by the number of stars in the dataset. Given that the Hessian matrix was negative definite, its inverse must also be negative definite, and therefore so will be the variance matrix. The major diagonal elements of the variance matrix define the negative of the variance of the parameters at the point returned via the optimization; the square root of these values is the standard deviation of the corresponding parameter.

2.3.2 Separating the Tidal Debris from the Spheroid

Given a dataset and a maximum likelihood PDF, it is possible to separate the data into subsets that have the density profile of each component that was fit during optimization (in this case a spheroid component with a Hernquist profile plus one or more stream components). It is possible to populate catalogs of independent structures in such a manner that the density distribution of that structure is accurately represented; however, it is not possible to populate a catalog for a given structure with only stars that are physically from that structure. For example, if a star selected from the dataset is computed to be in a stream with probability 0.6 and to be in the spheroid with probability 0.4, the star would be put in the stream catalog with probability 0.6 and in the spheroid catalog with probability 0.4. However, there is a 48% chance that the star is placed in the wrong catalog.

For each star, the probability, T_i, that it is drawn from the i^{th} stream population is calculated given the parameters where T_i is defined as

$$T_i(l, b, \mathcal{R}(g_0) \mid \vec{Q}) = \frac{S_i(l, b, \mathcal{R}(g_0) \mid \vec{Q})}{S(l, b, \mathcal{R}(g_0) \mid \vec{Q}) + B(l, b, \mathcal{R}(g_0) \mid \vec{Q})}, \tag{2.45}$$

where

$$B(l, b, \mathcal{R}(g_0) \mid \vec{Q}) = P_{spheroid} \frac{\rho^{con}_{spheroid}(l, b, \mathcal{R}(g_0) | \vec{Q}_{spheroid})}{\mathcal{I}^{com}_{spheroid}} \tag{2.46}$$

and

$$S(l, b, \mathcal{R}(g_0) \mid \vec{Q}) = \sum_{i=1}^{k} \left[P_{stream_i} \frac{\rho^{con}_{stream}(l, b, \mathcal{R}(g_0) | \vec{Q}_{stream_i})}{\mathcal{I}^{com}_{stream_i}} \right] \tag{2.47}$$

and $S_i(l, b, \mathcal{R}(g_0) \mid \vec{Q})$ is defined as the i^{th} component of the sum in equation 2.47.

After probability, T_i is calculated it is tested against a random number, λ, generated uniformly on the interval 0 and 1. The star is placed into the i^{th} stream catalog with probability equal to T_i and the spheroid catalog with probability $1 - \sum_1^k T_i$. Thus, distinct population catalogs are created for each structure that was optimized over: one for the smooth spheroid, and one for each tidal stream.

This nondeterministic approach of testing the star probability against a random number to extract the tidal debris from the stellar spheroid is used because of the definition of the stream model. Since the stream probability is defined solely as a function of the stars distance from the stream axis, simply assigning all stars with a probability greater than some threshold value to a stream catalog would result in all stars within a given distance of the stream axis to be assigned to that catalog. This would not be an accurate description of either the stream or spheroid populations as this would result in a cylinder of stars being carved out of the data rather than a set of stars that fit a specific distribution with Gaussian cross-section in density.

This separation technique has proved very useful as a means of analyzing the results of the optimization. The effectiveness of the model fits is able to be estimated from these separations and the separate catalogs themselves will be very useful in fitting tidal disruption models. The structure catalogs are not a very good method for selecting spectroscopic follow-up targets to further study the characteristics of stars drawn from a specific population (composition and velocity data, for example). These follow-up targets may be better selected through the explicit use of the probability, T_i, that a star is drawn from that population, rather than on the catalog which is a random assignment based upon this probability.

CHAPTER 3

Validating the Algorithm via Simulated Datasets

The accuracy and correctness of the algorithm was tested with simulated datasets that were designed to mimic those conditions found within the observed data: a dataset with one tidal stream and a smooth spheroid; a dataset with one tidal stream, a smooth spheroid, and a section of volume that needs to be removed; and a dataset with multiple tidal streams and a smooth spheroid. The successful testing upon these three datasets provide ample support for the correctness of the algorithm under any of these, or combination of these situations. This chapter provides the results of these three tests, as well as the method with which the simulated datasets were created.

3.1 Generating the Datasets

The spheroid is modeled globally as a smooth Hernquist profile (section 2.1.2) while the stream is modeled locally as a cylinder with density that decreases as a Gaussian from its axis (section 2.1.1). These distributions were generated separately and then merged to create a test dataset.

3.1.1 Generating the Tidal Debris

Tidal debris is simulated using an active generation technique. Thus, every star that is generated is a valid stream star according to the local model. Using a set of parameters that define the stream the vectors defining the cylinder position, $\vec{c}$, and orientation, $\hat{a}$, are calculated. Three random numbers are then generated: a uniform random number which defines the position along the stream axis, and two Gaussian random numbers (with mean zero and standard deviation defined via the stream width parameter, σ) which define the cross-sectional coordinate of the star. A Galactocentric Cartesian coordinate is calculated for the generated star through the use of the cross-sectional coordinate and the position along the stream axis.

The generated star is then converted from the Galactocentric Cartesian coordinate system used in generation to the observed Galactic coordinate system: longitude, latitude, and apparent magnitude. To this point, a fixed value of $M_{g_0} = 4.2$ for the absolute magnitude of the dataset has been assumed. [39] To account for the intrinsic absolute magnitude distribution of F turnoff stars, a random number, drawn from a Gaussian distribution with mean 0 and standard deviation 0.6 (see section 2.1.3 for the reasoning behind this number), is generated for each star. This random number is then added to the generated star's apparent magnitude and effectively spreads the structure in a manner similar to that seen in the observed data.

Finally, stars are inserted into the simulated stream dataset with a probability given by the efficiency function (described in section 2.1.4). In this manner, stars near the magnitude limit of the data rejected from the sample with a probability equal to the efficiency of object detection as a function of apparent magnitude as in the observed dataset. This process is repeated until the desired number of stars have been generated and added to the dataset.

3.1.2 Generating the Stellar Spheroid

Unlike the active generation technique used to generate a simulated tidal stream, the simulated stellar spheroid must be constructed using a rejection sampling technique. The active technique is not applicable here due to the significantly increased complexity of the global spheroid model over that of the simple Gaussian model used to locally describe the stream. It does not work, however, to simply generate randomly over the three dimensions of the stripe (μ, ν, R), since the volume elements are not uniformly distributed in these variables; the distribution across the stripe, in ν, varies according to the $\cos(\nu)$, while the distribution along the radial distance, R, must account for the ever increasing volume as the distance is increased. Fortunately, the angle along the stripe, μ, may be generated uniformly, for at a given distance, R, and angle through the stripe, ν, the volume of stars will be constant along the stripe.

The volume element within a stripe is given by:

$$dV = R^2 \cos(\nu) dr d\mu d\nu. \tag{3.1}$$

Integrating this volume element over the whole volume results in a stripe volume of

$$V = \frac{R_{max}^3}{3}(\mu^+ - \mu^-)(\sin(\nu^+) - \sin(\nu^-)). \tag{3.2}$$

Here, R_{max} denotes the maximum radial distance of the stripe and the positive and negative subscripts refer to the maximum and minimum (respectively) values of that coordinate within the stripe. Using this equation it is then possible to extract the functions with which to generate over for each variable. As previously stated, μ can be generated uniformly about the stripe, while the functions for ν and R are found by taking the inverse of equation 3.2 with respect to ν and R to get the functions

$$\begin{gathered}\nu = \sin^{-1}(u * (\sin(\nu^+) - \sin(\nu^-)) + \sin(\nu^-)), \qquad (3.3)\\ R = R_{max} w^{\frac{1}{3}},\end{gathered}$$

where u and w denote uniform random numbers between zero and one which can be used to generate uniformly over the spheroid.

Once a star has been generated according to the above functions, the probability of the star is calculated according to the PDF (2.1.7) of the algorithm. This probability is then divided by the total probability possible for a star in order to construct a weighted probability of the given star to be in the dataset. The total probability possible of a star is simply the maximum value of the PDF that can be returned given the current volume and parameter set that is being generated over. This weighted probability for the star to be in the dataset is then tested against a random number generated uniformly between zero and one. The star is added to the dataset if the probability of the star being in the dataset is greater than that of the random number; otherwise, it is rejected. This process is repeated until the desired number of stars have been added to the dataset.

3.1.3 Achievable Accuracies

For the simulated datasets, the "true" parameter values are known, for they are the values used to generate the simulated dataset. These values are compared with the "measured" maximum likelihood values. The difference is a set of achievable accuracies that can be expected from the optimizations.

The statistical errors were determined via the Hessian method described in section 2.3.1. Numerical errors driven primarily by the accuracy with which the numerical integrals are calculated within the likelihood function were estimated heuristically. It is possible to determine these numerical errors heuristically. This means that the numerical errors are estimated and do not comprise a true error bar.

To determine the errors heuristically, the accuracy of the likelihood for a fixed number of points in the numerical integrals was calculated. This was done by observing the change in likelihood caused by increasing/decreasing the number of integral points. The "error" in a given parameter is then estimated by perturbing that parameter, holding all others constant, by increasingly larger/smaller amounts until the deviation in likelihood, from the optimized parameter values, caused by the perturbation in parameter values is slightly greater than the value observed by modifying only the number of integration points. Through this procedure, it is possible to estimate the variance in a parameter with respect to the number of integration points.

Finally, it should be noted that there exist systematic errors within the SDSS data that is not present within the simulated datasets used for testing this algorithm. These systematic errors are unknown and are inherent to the data. All error bars quoted in regards this observed ("real") data assumes that the models used are accurate representations of the stellar density functions, including the those used for the smooth stellar spheroid, tidal debris, and absolute magnitude distribution of F turnoff stars.

3.2 Testing

After generating the smooth spheroid and stream-like populations using the above methods and combining them to form a complete dataset, the maximum likelihood method developed in chapter 2 was run on the datasets to determine the "measured" parameter values. Three data sets were created and tested independently: a simulation of SDSS stripe 82, a simulation of SDSS stripe 86 containing a section of missing volume, and a simulation of SDSS stripe 82 with two streams.

After analyzing these stripes, a series of tests to verify the robustness of the models were performed. The results of these tests are discussed below.

3.2.1 Simulated Stripe 82

A dataset that mimics the observable data in SDSS stripe 82 was generated as the first test dataset. The dataset was created with a smooth spheroid and a single stream. The simulated dataset was generated based upon the parameters seen in the "Generated" column of table 3.1 and was limited to the volume defined by the bounds: $(310^\circ < \mu < 59^\circ)$, $(-1.25^\circ < \nu < 1.25^\circ)$, and $(16 < g_0 < 22.5)$. The dataset was generated with a total of 205,708 simulated stars of which 28,498(13.85%) stars are in the stream. A density plot of the simulated dataset can be seen in figure 3.1.

The maximum likelihood algorithm was ran on this dataset eight times, each time starting from a different randomized set of input parameters. Randomized, here, means that a random perturbation of each of the actual parameters (those used to generate the dataset) was used to generate the input parameter set. The perturbation used was 75% of the parameter's actual value. Parameters outside this range are in principle allowed, provided they are within the bounds of the stripe; however, the likelihood surface becomes very flat at sufficient distance from the correct values. This causes the gradient to be very small and the gradient measurement to be dominated by numerical errors. Therefore, if the input parameters are too far away from the correct values, the optimization will not converge because there will not be enough information to choose a correct direction.

The optimization algorithm was allowed to run to convergence for these eight datasets. Of the eight, five optimized to the correct parameter values, two optimized to a local maximum, and one did not converge (presumably because the input parameter set was too distant from the true values).

The local maximum is comprised of approximately the correct parameter values with the exception of the stream orientation parameters, θ and ϕ, and the stream width parameter, σ. This means that the stream position and approximate number of stars within the stream is found correctly, as are the spheroid parameters. The discrepancy in the other three parameters is an artifact of the small volume over

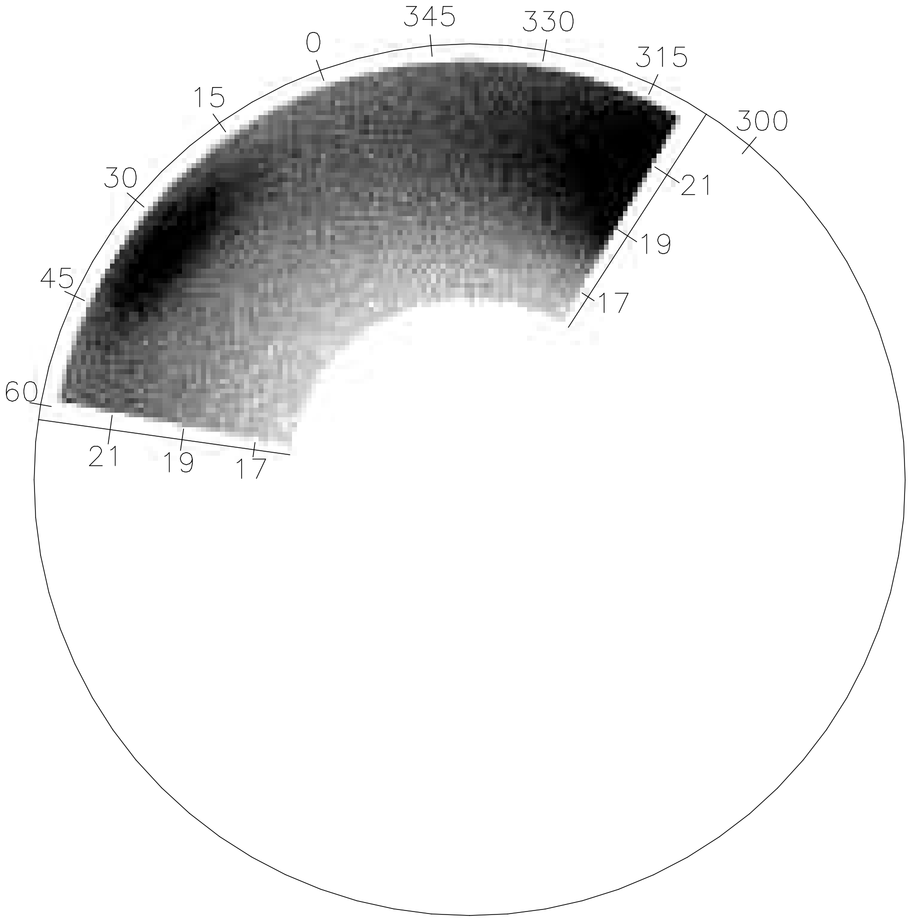

Figure 3.1: Stripe 82 simulated dataset density wedge plot. Plotted here is a Sun-centered density plot of the 205,708 stars generated to mimic SDSS stripe 82. The plane of the plot is along the angle $\nu = 0.0$. The reddening corrected apparent magnitude g_0 is labeled along the radial spokes, with $g_0 = 23$ denoted at the circle of constant magnitude. The angle about the stripe, μ, is marked in degrees about this circle. The simulated stream is easily discernible at the coordinates $(\mu, g_0) = (33.4°, 21.4)$

which the algorithm probes, and is caused by there being a valid fit to the data with parameters that are at a high inclination to the stripe. The width parameter, therefore, grows to compensate this incorrect angle. The local maximum exists primarily when the stream passes through the stripe plane at low inclination; the closer to perpendicular the stream and the data plane, the lower the ability for the algorithm to fit the data in this manner.

The average of the five successful optimizations was calculated and are reported in the “Optimized” column of table 3.1. The Hessian method was utilized to generate a set of error bars for the simulated data and these values can be seen in the “Achievable Accuracy” column of table 3.1. The heuristic errors were also calculated using the method described in section 3.1.3 and are given in the “Numerical Error” column of table 3.1. The two remaining columns in table 3.1, “Deviation” and “Std. Dev. of the Optimizations”, denote the difference between the “Optimized” value of the parameter and the “Generated” value of the parameter and the standard deviation of the parameter values returned from the five optimizations, respectively. As can be seen, the optimized parameter sets varied very little. It should be noted that if the theoretical deviation is large for a given parameter, then the likelihood changes very little with variation in that parameter. This can, therefore, lead to a larger deviation between optimized and true value of the parameter and can also make it more difficult for the algorithm to numerically find the maximum, for the gradient will be very small at this point. The errors calculated via the Hessian method assume the maximum of the likelihood has been found exactly.

A close examination of table 3.1 shows that all parameters have a “Deviation” smaller than that of the corresponding “Achievable Accuracy” with the exception of r_0. It has been found that the likelihood surface that corresponds to this parameter is exceptionally flat. Therefore, since the likelihood changes so little compared to perturbations in this parameter, it is not being calculated accurately enough to reach the “Generated” value. The true error bar should thus be taken as the sum, in quadrature, of the “Achievable Accuracy” and the “Numerical Error” columns as described in section 3.1.3. Once this is done, the “Optimized” value of all parameters are within the error bar of the “Generated” value. In most cases the numerical error

Table 3.1: Stripe 82 Simulated Dataset Results

Parameter	Generated	Achievable Accuracy	Numerical Error	Optimized	Deviation	Std. Dev. of Optimizations
q	0.670	0.013	0.000	0.671	0.001	0.0004
r_0 (kpc)	13.500	0.276	0.150	13.917	0.417	0.016
ϵ	-1.828	0.005	0.002	-1.833	0.005	0.005
μ (deg)	31.361	0.233	0.050	31.443	0.082	0.064
R (kpc)	29.228	0.167	0.040	29.217	0.011	0.010
θ (rad)	1.445	0.032	0.003	1.421	0.024	0.0005
ϕ (rad)	3.186	0.049	0.001	3.182	0.004	0.002
σ (kpc)	2.854	0.033	0.015	2.858	0.004	0.009

is negligible in comparison to the statistical error.

The average of the returned parameter sets was then used to create two separate catalogs that trace the density structure of the stream and spheroid via the separation algorithm described in section 2.3.2. A density plot of each of these catalogs can be found in figure 3.2. The stream density profile (left) has clearly been extracted from that of the stellar spheroid leaving a smooth Hernquist profile (right).

3.2.2 Simulated Stripe 86 With Volume Removal

A dataset that mimics the observable data in SDSS stripe 86 was generated to test the effect of removing a section of volume from the probed space on the accuracy of the model parameter determinations. This stripe was chosen because there is a small angle, about the stripe, in the stripe 86 dataset that needs to be removed before analysis. The dataset was created with a smooth spheroid and a single stream. The simulated dataset was generated based upon the parameters seen in the "Generated" column of table 3.2 and was limited to the volume defined by the bounds: $(310° < \mu < 420°(60°))$, $(-1.25° < \nu < 1.25°)$, and $(16 < g_0 < 22.5)$. After generating the dataset, a volume, $21.6° < 22.3°$, was removed in order to simulate the same missing volume in the observed data. As with the observed data, the removed volume passes through the center of the stream to be fit. After generation and removing the small volume above, the dataset contained a total of 198,732 simulated stars of which 29,800(15.0%) stars are in the stream. A density plot of the simulated dataset can be seen in figure 3.3.

The algorithm was allowed to converge over fourteen input parameter sets generated according to the same method as in section 3.2.1. Of these fourteen optimizations, five converged to the true parameters (those used to generate the dataset), while eight converged to a local maximum of similar origin to that discussed in section 3.2.1, and one did not converge (presumably due to the input parameters being too distant from the true values). The local maximum has a lower likelihood value than that of those that converged to the true parameters.

The average of the five successful optimizations is reported in the "Optimized"

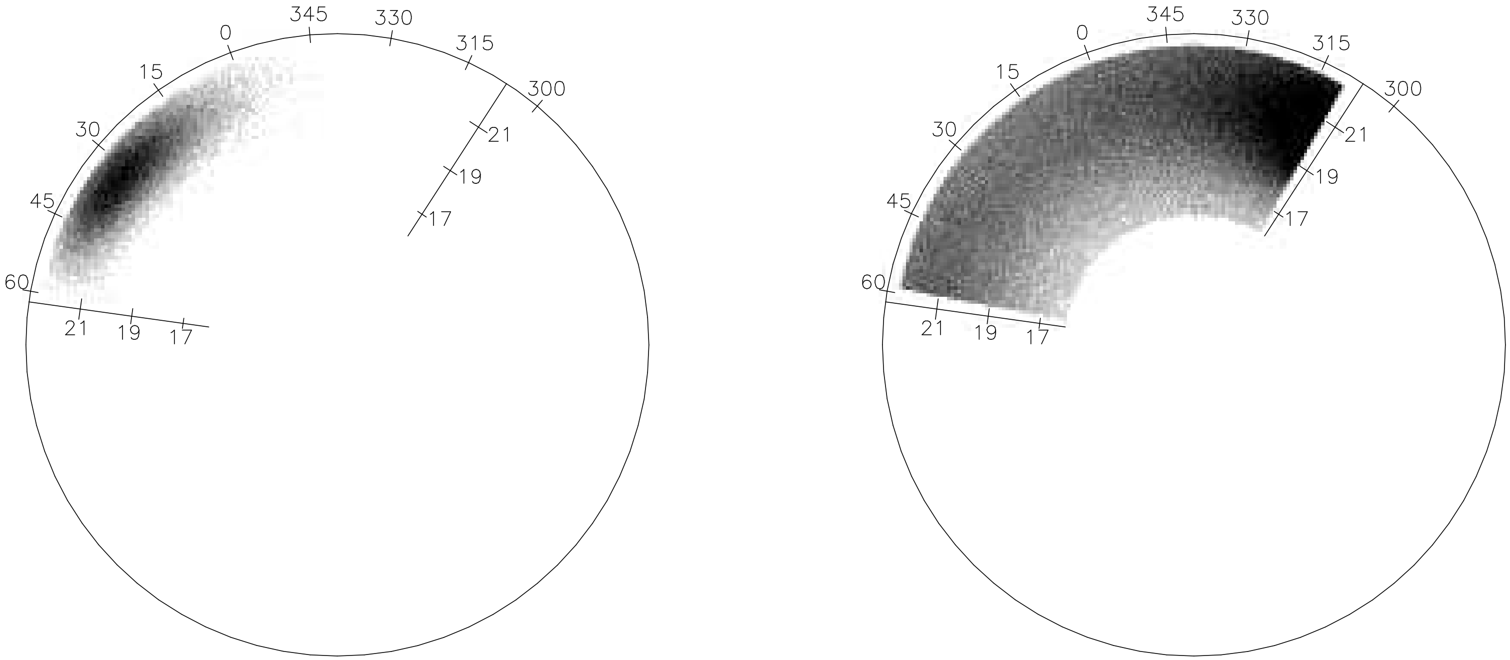

Figure 3.2: Stripe 82 simulated dataset separated density wedge plots. Plotted here, in the same manner as figure 3.1, is the same 205,708 star simulated dataset, however, the stars have been plotted separately based upon the catalogs returned from the separation algorithm. Thus, the stream (left) and the spheroid (right) can be seen after the stream has been extracted. The spheroid is clearly recovered as a smooth Hernquist profile after the removal of the stream component.

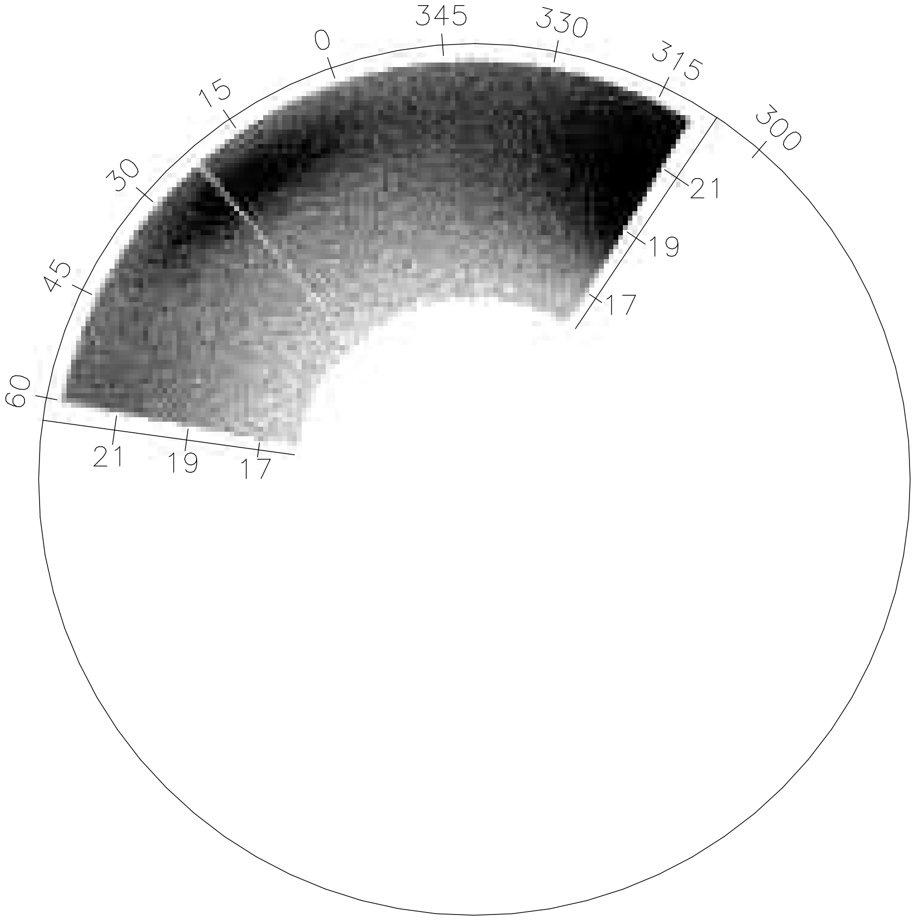

Figure 3.3: Stripe 86 simulated dataset with volume section removed density wedge plots. Plotted here, in the same manner as figure 3.1, is the 198,732 star simulated dataset. The stream is clearly visible at $(\mu, g_0) = (16.3°, 21.3)$. To simulate the conditions found in SDSS stripe 86, a small angle of the data volume, $21.6° < 22.3°$, has been removed. It should be noted that the removed volume is in the center of the tidal stream to be fit.

column of table 3.2. The Hessian method was utilized to generate a set of error bars for the simulated data and these values can be seen in the "Achievable Accuracy" column of table 3.2. The two remaining columns in table 3.2, "Deviation" and "Std. Dev. of the Optimizations," are defined in the same manner as in section 3.2.1. As in the previous simulated test results, the optimized parameter sets vary very little.

The average of the optimized parameter values corresponds very well with those values used to generate the data set. In general, the removal of a section of the volume appears to have no affect upon the achievable accuracy as calculated via the Hessian method. However, several optimized results fall just slightly outside of the 1σ error level when considering only the statistical error. However when taken in quadrature the statistical and numerical errors account for all deviations aside from that seen in ϕ. While the peak appears to be very sharp as according to the Hessian method, it would appear that this angle is harder to fit, in principle. It is quite possible that this parameter is difficult to fit in this instance since the removed volume passes through the center of the tidal debris, this may influence the angle just enough to prevent as accurate a fit as should be possible. However, even though ϕ falls outside the 1σ error bar, and falls just outside the 2σ error bar, it is well inside the 3σ errors, and having one parameter in eight at this level seems reasonable.

The separated stream and spheroid components are shown in figure 3.4. The stream density profile (left) has clearly been extracted from that of the stellar spheroid leaving a smooth Hernquist profile (right). According to the above results, the algorithm is still able to optimize to the true set of parameters for a set of data with a section of volume that needs to be removed. This is accomplished even in the unfortunate instance that the removed volume passes through the tidal stream to be fit.

3.2.3 Simulated Stripe 82 With Two Streams

To test the impact of simultaneously fitting two tidal streams a second simulated tidal stream, consisting of 20,000 simulated stars, was added to the dataset from section 3.2.1. The parameters with which the second stream was generated

Table 3.2: Stripe 86 Simulated Dataset Results

Parameter	Generated	Achievable Accuracy	Numerical Error	Optimized	Deviation	Std. Dev. of Optimizations
q	0.633	0.007	0.005	0.643	0.010	0.000
r_0 (kpc)	16.657	0.310	0.184	16.638	0.019	0.018
ϵ	-1.735	0.005	0.001	-1.734	0.001	0.000
μ (deg)	16.312	0.352	0.029	16.451	0.139	0.004
R (kpc)	26.077	0.162	0.042	25.899	0.178	0.004
θ (rad)	1.403	0.025	0.003	1.423	0.020	0.000
ϕ (rad)	0.086	0.004	0.003	0.074	0.012	0.001
σ (kpc)	2.425	0.033	0.008	2.462	0.037	0.006

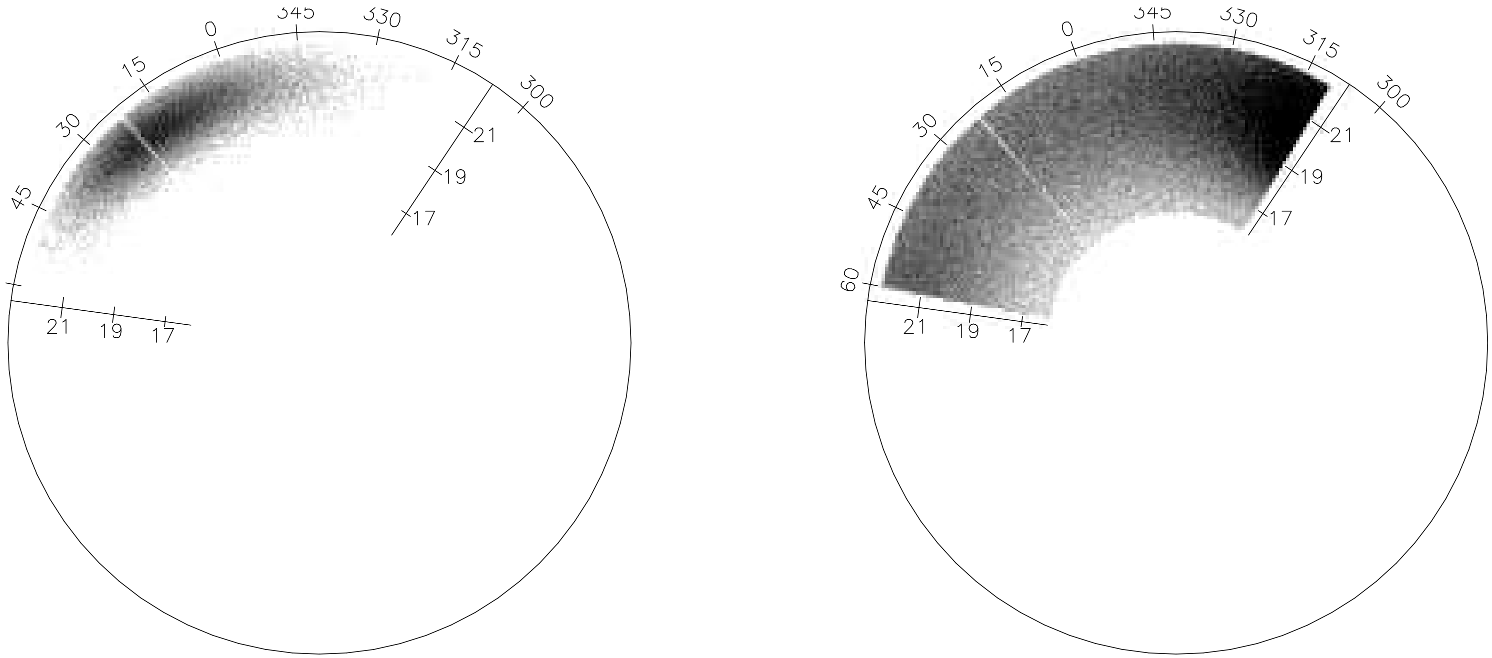

Figure 3.4: Stripe 86 simulated dataset with volume section removed separated density wedge plots. Plotted here, in the same manner as figure 3.1, is the same dataset found in figure 3.3, however, the stars have been plotted separately based upon the catalogs returned from the separation algorithm. Thus, the stream (left) and the spheroid (right) can be seen after the stream has been extracted. The spheroid is clearly recovered as a smooth Hernquist profile after the removal of the stream component, despite the missing volume of data.

can be found in table 3.3 (subscript “2”). With the addition of this new stream, the dataset contains 225,708 stars of which 28,498 (12.63%) are the first stream and 20,000 (8.86%) are the second stream. The stripe volume and spheroid parameters are the same as for the dataset in section 3.2.1. The dataset can be found in figure 3.5 Testing of this simulated dataset was performed in a similar manner as the previous with a total of fourteen randomized starts for the optimization.

The results of these fourteen optimizations saw five converge to the true parameter values (those used to generate the dataset), while the remaining nine optimizations converged to some combination of local maximums created via the two tidal streams. The existence of two pieces of tidal debris within the data created two local maxima within the likelihood surface, one for each tidal stream. Thus, it was suspected that three local maxima would be found within the dataset: when the true parameters are found for the first stream and the local maximum of the parameters found for second stream; when the true parameters are found for the second stream and the local maximum of the parameters are found for the first stream; and when the local maximum of the parameters are found for both streams. However, this final possibility of converging to the local maximum of the parameters for both streams proved to not exist. Of the fourteen optimizations, none were found to converge to this configuration of parameters, so it would appear that the combination of local maximums does not necessarily produce a local maximum itself. The nine optimizations that did not converge to the true parameter values were, therefore, found to converge to the local maximum created by parameters of one stream while the other converged to the true values. This is a very important result, for it proves that when optimizing over multiple streams, one of those streams converge to the correct parameter values. It should be noted that those optimizations to the true parameters, did indeed have the highest likelihood; while the optimizations to the true parameters of the second stream and the local maximum of the first stream (the original and larger stream) had the second highest likelihood; and the optimizations to the true parameters of the first stream and the local maximum of the second stream saw the lowest likelihood of all convergences. The results of the optimizations can be found in table 3.3.

Table 3.3: Stripe 82 Simulated Dataset with Two Streams Results

Parameter	Generated	Achievable Accuracy	Numerical Error	Optimized	Deviation	Std. Dev. of Optimizations
q	0.670	0.007	0.002	0.671	0.001	0.001
r_0 (kpc)	13.500	0.283	0.214	13.885	0.385	0.055
ϵ_1	-1.827	0.017	0.001	-1.841	0.014	0.002
μ_1 (deg)	31.361	0.228	0.052	31.438	0.077	0.016
R_1 (kpc)	29.228	0.169	0.028	29.233	0.005	0.012
θ_1 (rad)	1.445	0.038	0.007	1.479	0.034	0.124
ϕ_1 (rad)	3.186	0.017	0.006	3.205	0.019	0.006
σ_1 (kpc)	2.854	0.088	0.009	2.767	0.087	0.030
ϵ_2	-2.182	0.005	0.000	-2.177	0.005	0.001
μ_2 (deg)	1.000	0.121	0.037	1.093	0.093	0.011
R_2 (kpc)	25.000	0.116	0.058	24.824	0.176	0.017
θ_2 (rad)	1.000	0.021	0.002	0.974	0.026	0.006
ϕ_2 (rad)	-1.660	0.003	0.002	-1.663	0.003	0.001
σ_2 (kpc)	1.500	0.048	0.007	1.497	0.003	0.003

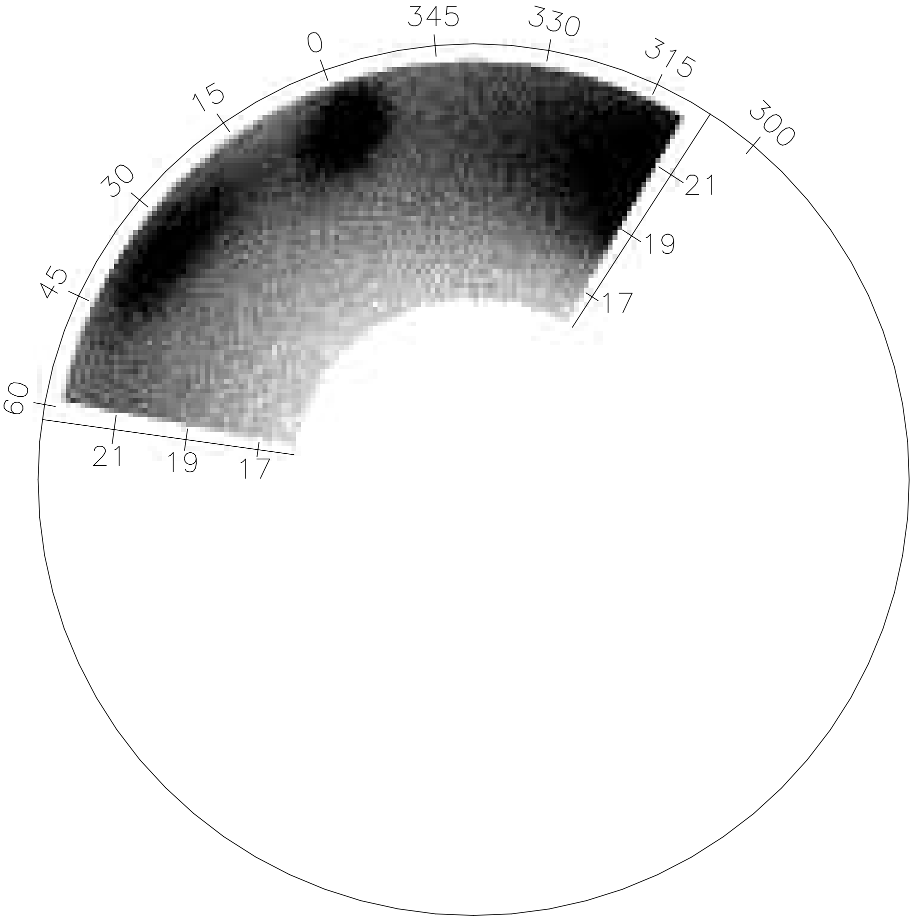

Figure 3.5: Stripe 82 simulated dataset with two tidal streams density wedge plot. Plotted here, in the same manner as figure 3.1, are the 225,708 stars generated by adding an additional stream to the dataset created in section 3.2.1. The simulated streams are easily discernible at the coordinates $(\mu, g_0) = (33.4°, 21.4)$ and $(\mu, g_0) = (1.0°, 21.2)$.

The optimized results correspond very well with those values used to generate the dataset. As can be seen, the vast majority of the results fall easily within the 1σ errors with regards to just the statistical errors, with the others easily falling within the 2σ level. This, by itself seems reasonable a reasonable occurrence, yet when taken in quadrature the complete error bar accounts for all but two parameters at the 1σ level, and those are just inside the 2σ level of error. As with the volume removal, the addition of a second stream seems to have little or no effect upon the achievable accuracies as derived via the Hessian method. This shows that even under complicated circumstances, the maximum likelihood algorithm is a good choice to achieve accurate results.

The average of the returned datasets was then used to create separate catalogs for each structure within the dataset: a catalog of the stars in the first stream, a catalog of stars in the second stream, and a catalog of the smooth stellar spheroid stars. This was accomplished via the separation algorithm, and these catalogs have been plotted in figure 3.6. The stream density profile of both pieces of tidal debris has clearly been extracted (left and center) leaving a smooth Hernquist profile (right).

The above results show that the optimization algorithm performs admirably when posed with the task of simultaneously fitting multiple pieces of tidal debris within the same dataset. These results also show that when multiple streams are fit, the local maximum problem still exists; however, this only occurs in the convergence to the local maximum of a single stream, not both. This important find, implies that when fitting multiple debris pieces that at least one of the optimized parameter sets is the true optimal parameters.

3.3 Robustness of the Models

The previous sections have shown that the optimization algorithm produces the optimum parameters (those used to generate the datasets) given the data is drawn from the models developed for the algorithm. This section will examine how the results of optimizations over data that is not drawn from the models within the algorithm and the validity of various assumptions in those models.

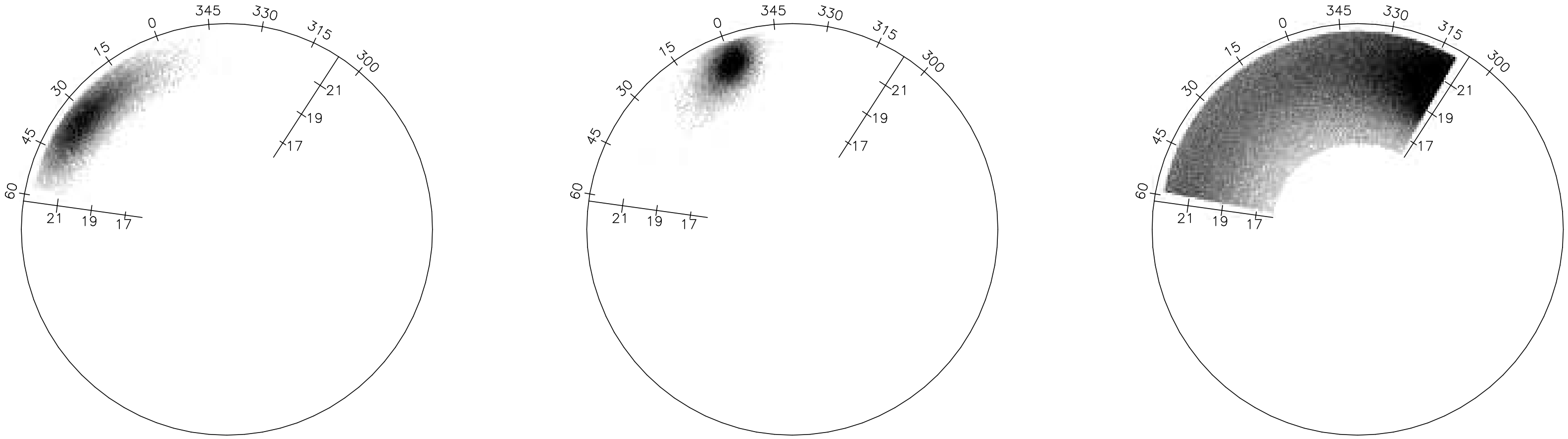

Figure 3.6: Stripe 82 simulated dataset with two tidal streams separated density wedge plots. Plotted here, in the same manner as figure 3.1, is the same dataset found in figure 3.5, however, the stars have been plotted separately based upon the catalogs returned from the separation algorithm. Thus, the original first stream (left), from the dataset seen in figure 3.1, and the second added stream (center) can be seen to be completely recovered and separate from the spheroid (right). The spheroid is clearly recovered as a smooth Hernquist profile after the removal of the stream components. The addition of multiple streams clearly does not affect the fitting or the separation algorithms.

3.3.1 Impact of Magnitude Distribution

To examine the necessity of modeling the absolute magnitude distribution in F turnoff stars, a series of optimizations were allowed to run to convergence in which the optimizations were completed assuming no absolute magnitude distribution. Thus, all stars within the dataset were assumed to have an absolute magnitude, $\bar{M}_{g_0} = 4.2$ These tests were completed using the dataset from section 3.2.1. The results of these optimizations showed that the stream positional parameter, μ, and the spheroid parameter r_0, were relatively unaffected by this simpler model. However, the rest of the parameters deviated wildly from their generated values with the stream parameters R, θ, and ϕ representing the worst of the parameters and reaching upward of 34σ in error.

3.3.2 Stream Model Correctness

Next, the robustness of the cylindrical stream model with Gaussian fall-off from the axis was examined. To do this, a reproduction of the Sgr dwarf galaxy tidal disruption generated in [79] was created using a semi-analytic N-body approach. The reproduction was created using the same parameters for the Galactic potential and kinematic values. The NEMO Stellar Dynamics Toolbox [89] was used to evolve an orbit for the Sgr dwarf disruption. Specifically, a Plummer sphere composed of one million particles (representing the Sgr dwarf) was allowed to evolve in a Galactic potential that is spherically symmetric and has velocity dispersion of 114 km s^-1. The system was allowed to evolve for 3.18 Gyr until it reached the present position of the Sgr dSph. The result of this reproduction is plotted in figure 3.8 and is consistent with that found in [79]. A volume corresponding with that of SDSS stripe 82 was extracted from this simulation of the Sgr dSph disruption and combined with the model spheroid created for the dataset seen in section 3.2.1. This new dataset was then used as input to the optimization algorithm and it was allowed to run to convergence.

Utilizing the optimized parameters derived from optimizing over the dataset created above, a new simulated stream was created using the method derived in section 3.1.1. By generating this new simulated stream, a means of comparison is thus derived for comparing the disruption data and the model data within a single stripe. In order to compare the two datasets, a cross section of the two streams, 1 kpc thick, and centered at the optimized stream center is plotted in figure 3.7. Along with this cross section, a histogram over the cross section is plotted beneath the respective cross section. Figure 3.7 (left) depicts the cross section and histogram of the stream generated via the N-body disruption, while figure 3.7 (right) depicts the stream generated according to the model using the parameters returned from optimizing over the dataset created using the N-body disruption data. It can be seen that the distribution of the N-body stream is, indeed, not Gaussian; however, the drawback to using an N-body model is that there are no correct model parameters with which to compare the results. The optimized center and direction of the N-body stream, as seen in figure 3.7 (left) and figure 3.8 are reasonable. In order to determine the error in the fitting of the stream center, what is meant by the center of an asymmetric distribution must be defined; however, the optimized center determined by the algorithm seems a reasonable choice.

The validity of a linear fit to a tidal stream is addressed by estimating the curvature of the Sgr tidal stream within SDSS stripe 82. Assuming the distance to the center of the stream to be 29 kpc as found in [67], it can be calculated that the 2.5° wide SDSS stripe would be 1.3 kpc thick at this distance. Assuming the stream intersects the stripe plane at an inclination of 30°, as according to [90], the length of the stream in stripe 82 would then be 2.5 kpc. The radius of curvature of the trailing Sgr tidal stream within the orbital plane can then be estimated via fitting a circle to the two southern detections in [67] and is determined to be approximately 18 kpc. Therefore, the deviation from linear of a 2.5 kpc long stream segment can be found to be $d = 0.6$ kpc at its edge. This is much smaller than that of the width of the stream at this point (6 kpc) according to [90]. Thus, the linear approximation of a stream over a 2.5° wide stripe is quite reasonable, unless the stream passes through the stripe plane at incredibly low inclinations such that the stream direction is approximately parallel to the stripe plane.

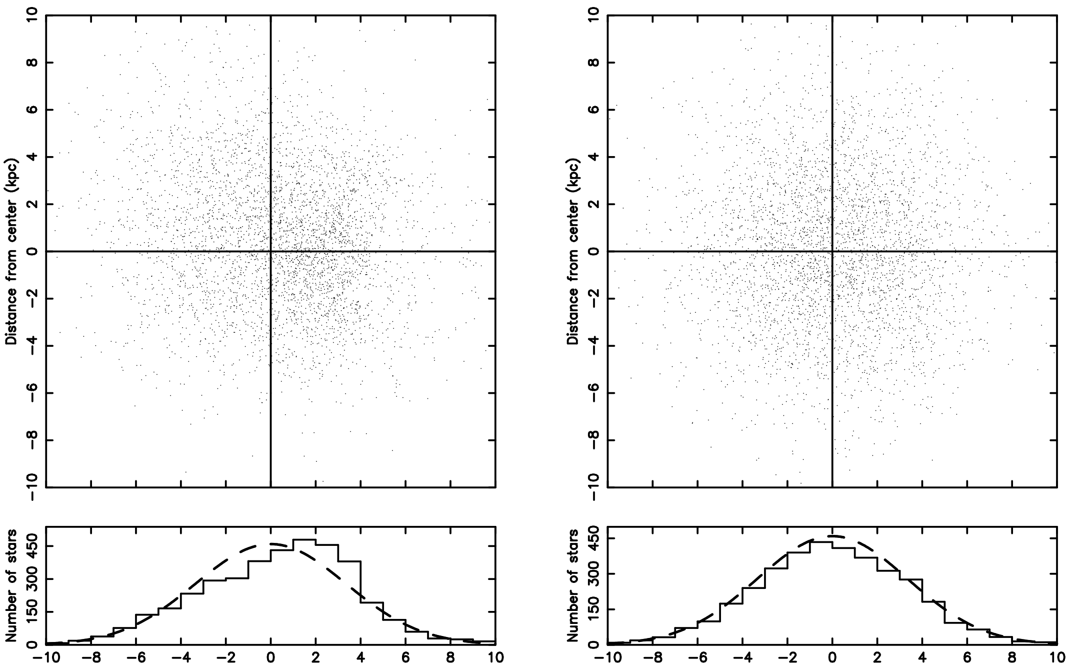

Figure 3.7: Cross-sections of Sgr N-body simulation stream (left panel) and simulated stream (right panel). The upper figure in both panels show the 1 kpc thick cross-section of the respective data set. The cross-sections are centered at the best-fit value of the optimization of the center in the N-body simulation from figure 3.8. Here the axes are perpendicular to the stream direction. The X-axis is $0.053X + 0.055Y + 0.997Z$ and the Y-axis is $0.055X + 0.997Y - 0.058Z$, where X,Y,Z are Galactocentric Cartesian coordinates with the Sun at X = -8.5 kpc and moving in the direction of positive Y. The lower figure of both panels is a histogram of those stars within the cross section binned along the X-axis. The heavy dashed line shows a Gaussian distribution with standard deviation given by σ from the fit to the N-body simulation. Note that the cross-section of the N-body simulation is non-Gaussian and somewhat asymmetric. Also note the model simulated stream is well fit by a Gaussian. The density distributions in the left and right panels are not the same, however, the algorithm still fits a reasonable center for the non-Gaussian N-body data set.

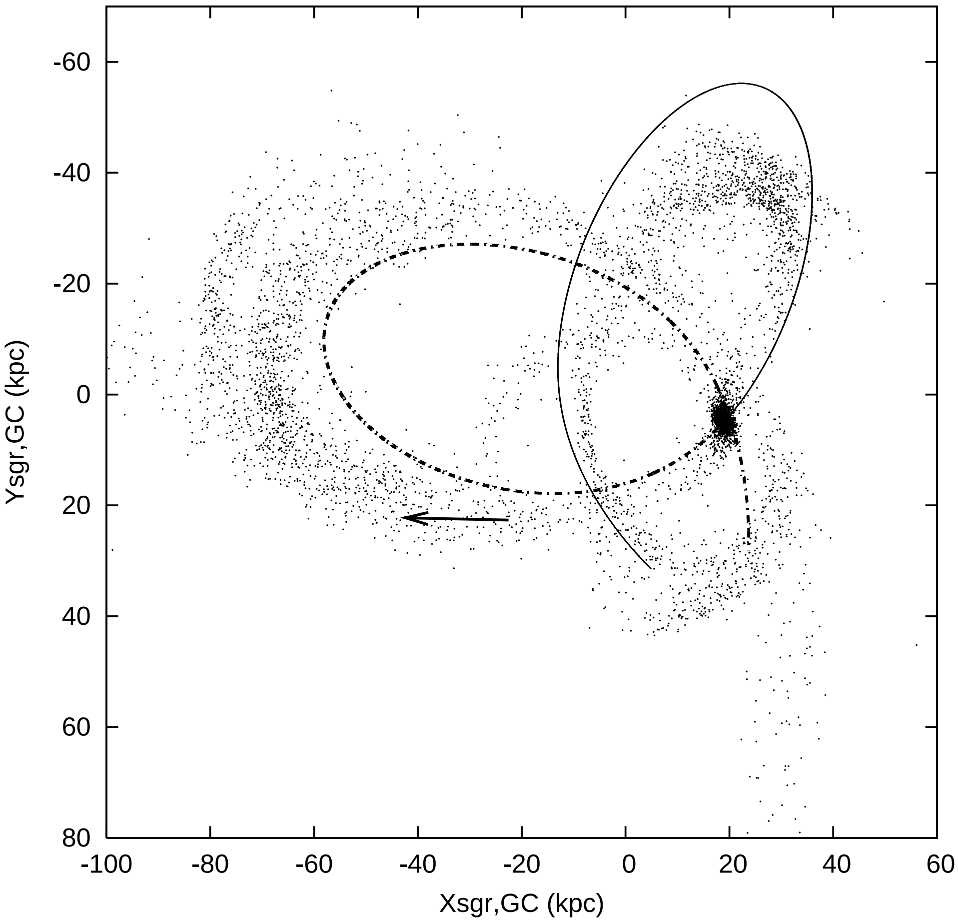

Figure 3.8: Disruption of one million particle simulated Sgr dSph as seen in the Sgr X-Y orbital plane. A spherical dark matter halo ($q = 1$) and velocity dispersion $\nu_{halo} = 114$ km s^{-1} was used. For clarity, the stream was sampled 1 in 100. The thin line denotes the future orbit of the core while the dotted line denotes the past orbit. The past orbit is not closed, but actually follows the lower trailing stream. The arrow shows the center (tail) and direction returned by optimizing over the stars within the SDSS stripe 82 volume.

3.3.3 Spheroid Model Correctness

Finally, the effect of an incorrect spheroid model on the optimization was tested. It is far easier to modify the model fit by the algorithm than to generate many differing datasets with various spheroid densities. Therefore, the dataset used in section 3.2.1 was fit multiple times here using an incorrect spheroid model. The exponential component of the Hernquist model was modified for these tests. The dataset was optimized using an exponential in the Hernquist of 3.5, 2.5, and 2.0 as compared to the value of 3.0 used to generate the data. The results from these tests can be seen in table 3.4. In all cases, the stream parameters experienced little to no change and were within the achievable accuracies calculated for this dataset. As expected the spheroid parameters are incorrect, yet represent the best model profile fit to the simulated date within the volume of the stripe. The results of this test successfully shows that tidal debris can be successfully and accurately fit even if the spheroid model is incorrect. This is incredibly important and useful, for it means that all tidal debris can be fit, characterized, and extracted from the spheroid allowing the spheroid to be studied without contamination from tidal debris and the correct model for the stellar spheroid density profile to be determined.

Table 3.4: Results of Tests Fitting an Incorrect Stellar Spheroid Model

			Optimization		
Parameter	Generated	Achievable Accuracy	$\alpha = 3.5$	$\alpha = 2.5$	$\alpha = 2.0$
μ (deg)	31.361	0.233	31.449	31.526	31.457
R (kpc)	29.228	0.167	29.094	29.326	29.108
θ (rad)	1.445	0.032	1.426	1.452	1.437
ϕ (rad)	3.186	0.049	3.172	3.168	3.160
σ (kpc)	2.854	0.033	2.869	2.848	2.865

CHAPTER 4
SDSS Data Analysis

The application of the maximum likelihood algorithm to characterize the Sgr dwarf tidal stream in SDSS photometric data is described here. This chapter will describe the data that was used and give an in-depth analysis of the results extracted from each of the datasets the maximum likelihood algorithm was applied to.

4.1 The Datasets

All of the data analyzed in this manuscript was taken from the SDSS photometric catalog. The results presented here contain results derived from both SDSS DR6 and SDSS DR7 data. The southern Galactic cap analysis was completed with SDSS DR6 catalog while all of the north Galactic cap analysis was completed using data from the SDSS DR7 catalog. The SDSS data is organized into a series of great circle stripes that are 2.5° wide. The maximum likelihood algorithm presented here takes advantage of this stripe structure to fit the tidal debris using a simple geometric model in a piecewise manner, such that each stripe is analyzed separately. All sources, from a given stripe, that were identified as point sources were selected that have the color of blue F turnoff stars. It was shown in [39] that the Sgr turnoff is much bluer than that of the thick disk stars and even slightly bluer than the stellar halo, in general. Selecting those stars consistent with the colors of the Sgr turnoff will preferentially select those stars in the stream and helps to limit the amount of contamination from other Galaxy components.

Those sources with colors $0.1 < (g-r)_0 < 0.3$ and $(u-g)_0 > 0.4$, that were not EDGE or SATURATED, and with magnitude $g_0 > 16$ were added to the dataset. The subscript "0," here denotes that reddening corrected magnitudes were selected. All of the selected stars are have $b > 30°$ (or $b < -30°$ for those southern stripes) and have distances $R > 2.3$ kpc. All stars are therefore far from the Galactic plane and behind the dust. It can be reasonably estimated that all reddening occurs due to the total amount of dust along that line of sight in the sky. The amount of dust along a given line of sight is determined through the well known dust map created in [91]. The color cut in $(g-r)_0$ is taken to select only those blue F turnoff stars with which the average absolute magnitude is taken to be $\bar{M}_{g_0} = 4.2$. The color cut in $(u-g)_0$ is performed in order to remove contamination of the sample by low redshift quasi-stellar objects (QSOs).

As mentioned previously in this manuscript, the SDSS is organized into a series of great circles across the sky and the maximum likelihood algorithm presented here is designed to leverage this survey design by analyzing the spatial properties of structures over small volume. Thus, a single dataset is comprised of only those stars that make up an SDSS stripe. Therefore, all datasets are 2.5° wide. Stars brighter than $g_0 = 16$ were removed to avoid saturated stars. At this magnitude most if not all contamination by disk stars is avoided since magnitude $g_0 = 16$ corresponds to the approximate distance of $R = 2.3$ kpc. The datasets are typically limited to $g_0 < 22.5$. This is because the efficiency function, described in section 2.1.4, begins to fall rapidly at approximately this value. However, the Sgr stream is seen at much fainter magnitude ($g \approx 23$) in F turnoff stars. In instances where the Sgr stream is observed at these faint magnitudes, the faint limit on the stripe is increased accordingly such that the stripe can be analyzed with regard to the Sgr stream.

The angular length of each stripe is, in general, $\Delta\mu \approx 140°$. However, the angular lengths of the stripes used in these analyses are shorter to reduce the complexity of the model required to describe the data. For example, the Monoceros stream ([39] [40]) is seen towards the anti-center of the Galaxy and is apparent in the data along the edge of many stripes within the north Galactic cap. Therefore, the angular length of these stripes were chosen to specifically remove all instances of this structure. Similarly, a section of data is removed around globular clusters and the optimization over these datasets is then performed using the algorithmic method for removing a section from the probed volume seen in section 2.1.5. The Hernquist profile is often not a good fit to the data towards the Galactic center. These sections are removed to prevent the occurrence of these poor fits.

4.1.1 Fitting the Datasets

The datasets constructed in the method described above are then used as input to the maximum likelihood algorithm. In all cases of the observed data, a number of optimizations were completed such that five of these optimizations were found to converge to the "best-fit" parameters. "Best-fit" is defined here as the parameters which result in the highest likelihood. The optimizations are completed using a set of randomized input parameters, where randomized, here, is the perturbation about an initial set of parameters chosen by eye. These amount of these perturbations is typically 75% as was used when testing the algorithm, however, in certain instances parameters grow too large for this to be an adequate method. In this instance, a perturbation by 25% of the total range of the parameter is used. For example, should the angular positional parameter $\mu = 200^\circ$ and the angular length is limited by $150^\circ < \mu < 250^\circ$, a perturbation by 75% is too large. Therefore, the perturbation is taken to be 25% of the total angular length. Thus, the perturbation amount would be by 25% of 100° and the initial parameter of 200° would be randomly perturbed by 25°.

The spheroid is a complicated thing that contains numerous pieces of substructure. This often demands that multiple streams be simultaneously fit even if only one piece of substructure is being analyzed. This is because other pieces of substructure can influence the optimization of the maximum likelihood algorithm. This problem becomes particularly bad when there are two pieces of substructure very near each other. In these instances, the algorithm tends to fit both pieces of substructure as a single entity, thereby invalidating the results obtained. For this reason all of the datasets in the North Galactic cap are fit using three streams simultaneously. The datasets from the South Galactic cap appear to be much less complicated and are adequately fit using a single stream.

The existence of the local maxima described in section 3.2 will be assumed from this point on. That is to say, some number of optimizations will converge to a local maximum associated with this phenomenon. However, only the results of those five optimizations that converged to the "best-fit" parameters will be presented here. It can also be assumed that some number of optimizations will not converge at all due to the randomized parameters being too distant from the “best-fit” parameters to provide an accurate direction for the gradient. Finally, the results for the stellar spheroid will be given on a stripe-by-stripe basis with those results for the tidal debris; however, these results will not be approached until a complete discussion of the results over all stripes is possible in section 5.3.

4.2 SDSS Stripe 82

SDSS stripe 82 is located in the south Galactic cap along the celestial equator. Therefore, the great circle coordinates, μ and ν, used to describe angular position along a stripe are exactly the more common equatorial coordinates, right ascension (α) and declination (δ), respectively. The angular length about the stripe was limited to 109° where $310^\circ < \mu(\alpha) < 59^\circ$. A globular cluster was also found within the data and a volume section removed with coordinates $323.2^\circ < \mu(\alpha) < 323.6^\circ$ and $-1.0^\circ < \nu(\delta) < -0.7^\circ$. The final dataset was composed of 115,907 F turnoff stars. A plot of the entire dataset can be seen in figure 4.1.

The average results from five optimizations to the “best-fit” can be seen in table 4.1 in the “Optimized” column. Additionally, the statistical and numerical errors are presented within the appropriate column as calculated via the Hessian and heuristic methods, respectively. Finally, the standard deviation of these five optimizations are presented in the final column. Utilizing the results of the optimizations, the separation algorithm was used to generate separate catalogs for the Sgr stream and the stellar spheroid. These catalogs are plotted separately in figure 4.2. The stream (left) has clearly been extracted from the stellar spheroid (right).

The stream normalization parameter, ϵ, provides a means for determining the number of stars within the stream. Here, $\epsilon = -1.827$ and using equation 2.19 it can be calculated that there are 16,050 stars in the Sgr stream in stripe 82 out of the total 115,907 stars in the dataset. Performing a calculation that parallels that of equation (10) of [90] it is possible to estimate the total stellar mass in stripe 82 as a fraction of the Sgr dwarf itself. First, the number of stars must be calculated from figure 6 of [39] that are within the color cut $(0.1 < (g-r)_0 < 0.3)$ and magnitude

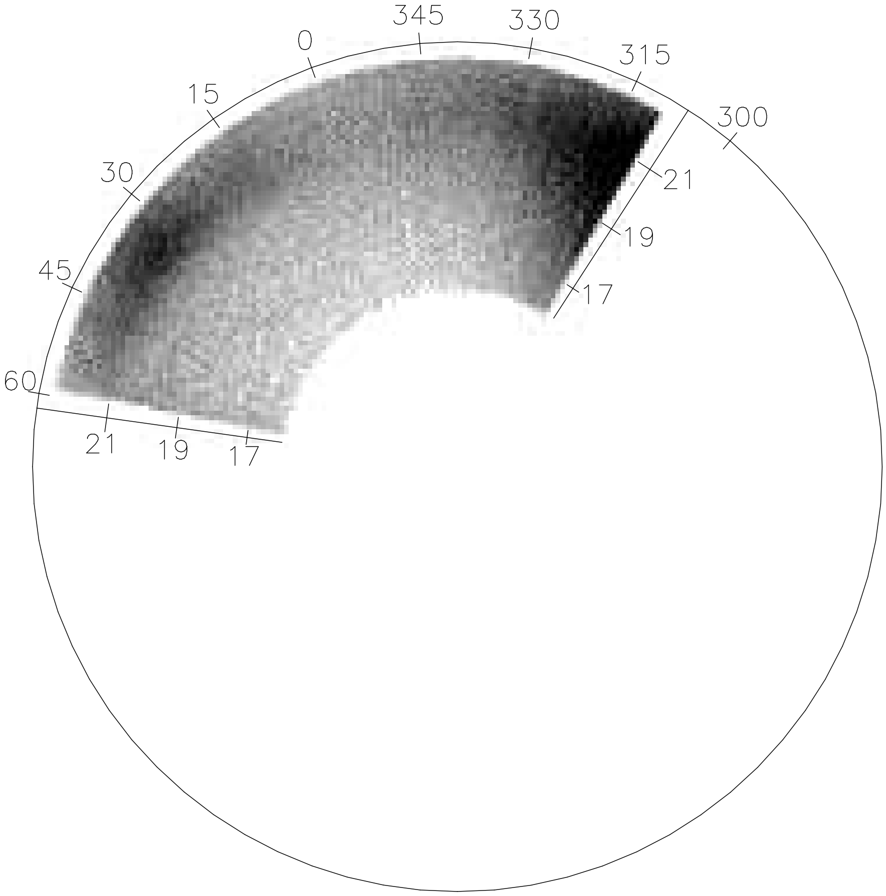

Figure 4.1: SDSS stripe 82 dataset density wedge plot. Plotted here is a Sun-centered density plot of the 115,907 F turnoff stars selected from DR6 with colors $0.1 < (g - r)_0 < 0.3$ and $(u - g)_0 > 0.4$. The plane of the plot is along the angle $\nu = 0.0$. The reddening corrected apparent magnitude g_0 is labeled along the radial spokes, with $g_0 = 23$ denoted at the circle of constant magnitude. The angle about the stripe, μ, is marked in degrees about this circle is limited to the angle $310° < \mu < 419°(59°)$. The Sgr tidal stream is easily discernible at the approximate coordinates $(\mu, g_0) = (31°, 21.5)$.

Table 4.1: **SDSS Stripe 82 Results**

Parameter	Optimized	Statistical Error	Numerical Error	Std. Dev. of Optimizations
q	0.458	0.023	0.005	0.001
r_0 (kpc)	19.404	0.581	0.090	0.051
ϵ	-1.827	0.005	0.001	0.000
μ (deg)	31.373	0.244	0.080	0.008
R (kpc)	29.218	0.184	0.070	0.012
θ (rad)	1.444	0.044	0.010	0.001
ϕ (rad)	3.184	0.034	0.008	0.002
σ (kpc)	2.862	0.025	0.008	0.009

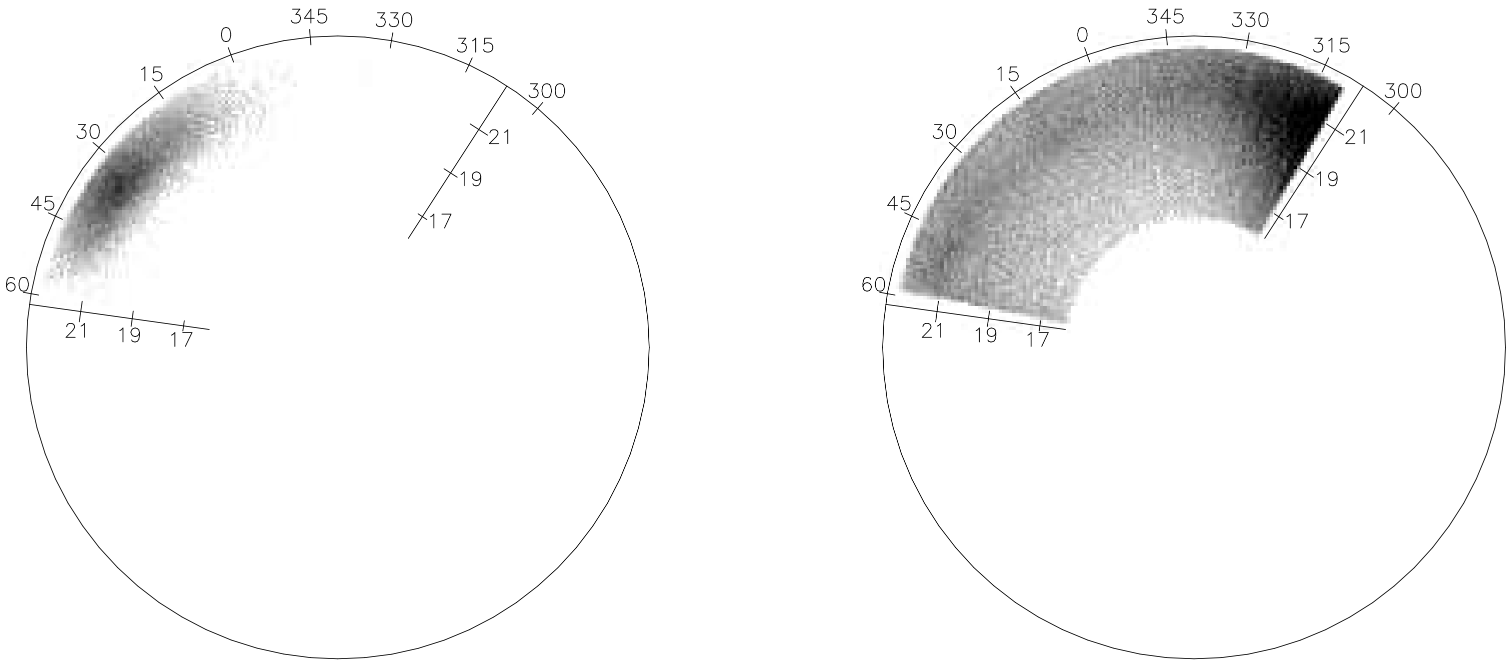

Figure 4.2: SDSS stripe 82 dataset separated density wedge plots. Plotted here, in the same manner as figure 4.1, is the same 115,907 star dataset, however, the stars have been plotted separately based upon the catalogs returned from the separation algorithm. Thus, the Sgr tidal stream (left) and the stellar spheroid (right) can be seen after the stream has been extracted. The Sgr stream has clearly been extracted from the stellar spheroid.

limits ($16 < g_0 < 22.5$) of the data used in optimization. This amounts to 2,184 stars. This is now substituted into equation (10) of [90], replacing the previous value used for G/G-type stars, and results in an estimate of the total number of F turnoff stars currently in the Sgr dwarf itself of 1,798,700 stars. The percentage of F turnoff stars in stripe 82 versus in the Sgr core itself is therefore 0.9%. Therefore, stripe 82 contains 0.9% of the Sgr dSph's current F turnoff stars. Also, in [90], the width of the Sgr stream in stripe 82 is estimated to have a FWHM of 6 kpc. The stream width, as determined by the maximum likelihood method, is $\sigma = 2.86$ which corresponds to a FWHM of 6.7 ± 0.06 kpc which is in good agreement with the previously stated value.

4.3 Additional SDSS Stripes

Sixteen additional stripes containing Sgr tidal debris have been analyzed. These are the two southern SDSS stripes beyond stripe 82 (stripes 86 and 79), and twelve of the contiguous northern stripes (stripes 23, 22, 21, 20, 19, 18, 17, 16, 15, 13, 11, and 9). These analyses were completed in a similar fashion to that done for stripe 82. Table 4.2 provides a listing of dataset statistics for each of the stripes analyzed including the volume limits, number of stars comprising the data set, and the SDSS data release the data was extracted from. The number of streams optimized are also presented here. Additional information regarding specific stripes can be found below. The values and results for stripe 82 have been duplicated here for completeness.

Stripe 86: A data artifact was removed at $21.6^\circ < \mu < 22.3^\circ$.

Stripe 82: A globular cluster was removed at $323.2^\circ < \mu < 323.6^\circ$ and $-1.0^\circ < \nu < -0.7^\circ$.

Stripe 23: A globular cluster was removed at $207^\circ < \mu < 209^\circ$ and $-1.25^\circ < \nu < -0.8^\circ$.

Stripe 22: Two globular clusters were removed: (1) $207^\circ < \mu < 209^\circ$ and $0.8^\circ < \nu < 1.25^\circ$; and (2) $202^\circ < \mu < 204^\circ$ and $-0.5^\circ < \nu < 0.4^\circ$.

Stripe 18: A globular cluster was removed at $197.0° < \mu < 198.0°$ and $-1.25° < \nu < -1.0°$.

Stripe 17: Two globular clusters were removed: (1) $182.4° < \mu < 183.0°$ and $0.9° < \nu < 1.25°$; and (2) at $197.0° < \mu < 199.0°$ and $0.4° < \nu < 1.25°$.

The results of the optimizations for the Sgr tidal stream are presented in table 4.3 with supplemental derived results in table 4.4. The complete data sets and the results of extracting the Sgr tidal debris using these optimizations can be found in figures 4.3-4.30. It should be noted that number of stream stars quoted in table 4.3 and used for the calculation of the "% of Sgr dSph itself" values in table 4.4 corresponds to the number of stars extracted via the separation algorithm and not the theoretical value calculated via the ϵ parameter, though in practice there is negligible difference between these two values.

Table 4.2: **SDSS Stripe Dataset Statistics**

Stripe	μ_{min}	μ_{max}	$g_{0_{min}}$	$g_{0_{max}}$	# streams	# stars	DR
86	310°	60°	16	22.5	1	111,642	6
82	310°	59°	16	22.5	1	92,789	6
79	311°	56°	16	22.5	1	92,789	6
23	133°	230°	16	22.5	3	65,336	7
22	131°	225°	16	22.5	3	66,201	7
21	133°	210°	16	22.5	3	60,503	7
20	133°	249°	16	22.5	3	105,909	7
19	135°	230°	16	22.5	3	84,046	7
18	135°	240°	16	22.5	3	95,462	7
17	135°	235°	16	22.5	3	91,626	7
16	135°	240°	16	22.5	3	107,033	7
15	135°	240°	16	22.5	3	108,460	7
13	135°	235°	16	22.5	3	118,836	7
11	150°	229°	16	23.0	3	97,434	7
9	170°	235°	16	23.5	3	95,435	7

Table 4.3: SDSS Stripe Results

Stripe	μ	R (kpc)	θ (rad)	ϕ (rad)	σ (kpc)	# stream stars
86	16.312° ± 0.400°	26.077 ± 0.178	1.403 ± 0.028	0.086 ± 0.017	2.425 ± 0.110	16,695
82	31.373° ± 0.257°	29.218 ± 0.197	1.444 ± 0.045	3.184 ± 0.035	2.862 ± 0.026	16,925
79	38.273° ± 0.316°	30.225 ± 0.250	2.215 ± 0.060	0.323 ± 0.069	2.774 ± 0.231	9,460
23	132.483° ± 0.265°	16.767 ± 0.540	0.437 ± 0.042	−1.568 ± 0.510	1.177 ± 0.039	1,016
22	135.914° ± 0.109°	18.138 ± 0.357	0.720 ± 0.021	−1.236 ± 0.319	1.667 ± 0.096	2,433
21	141.681° ± 0.788°	21.218 ± 0.509	0.550 ± 0.161	−0.279 ± 0.521	1.088 ± 0.649	3,560
20	148.028° ± 0.579°	22.784 ± 0.463	0.801 ± 0.198	−0.198 ± 0.177	1.124 ± 0.161	4,371
19	151.499° ± 0.472°	23.491 ± 0.302	0.700 ± 0.126	−0.099 ± 0.113	0.906 ± 0.162	5,266
18	157.138° ± 0.500°	25.298 ± 0.408	1.041 ± 0.107	−0.327 ± 0.101	2.226 ± 0.142	7,380
17	161.983° ± 0.573°	25.696 ± 0.394	2.011 ± 0.097	2.894 ± 0.057	2.569 ± 0.221	8,889
16	177.479° ± 0.876°	28.296 ± 0.416	1.343 ± 0.061	−0.093 ± 0.039	4.366 ± 0.333	21,621
15	184.577° ± 0.617°	31.162 ± 0.522	1.863 ± 0.061	3.205 ± 0.104	3.191 ± 0.779	16,502
13	196.970° ± 0.413°	36.908 ± 0.334	1.701 ± 0.119	0.192 ± 0.039	3.756 ± 0.327	17,578
11	206.137° ± 6.687°	40.365 ± 6.474	1.234 ± 0.737	3.301 ± 0.422	3.585 ± 1.506	9,011
9	219.735° ± 0.340°	43.449 ± 0.482	1.703 ± 0.040	1.333 ± 0.049	4.789 ± 0.366	19,505

Table 4.4: SDSS Stripe Results Supplemental

Stripe	l	b	FWHM (kpc)	% Sgr dSph itself
86	134.776°	−72.342°	5.71 ± 0.26	0.9%
82	159.223°	−57.558°	6.74 ± 0.06	0.9%
79	163.312°	−48.400°	6.53 ± 0.54	0.5%
23	205.701°	30.331°	2.77 ± 0.09	0.1%
22	207.239°	33.876°	3.93 ± 0.23	0.2%
21	209.187°	39.691°	2.56 ± 1.53	0.3%
20	212.030°	45.983°	2.65 ± 0.38	0.2%
19	215.528°	49.248°	2.13 ± 0.38	0.3%
18	220.540°	54.432°	5.24 ± 0.33	0.4%
17	226.857°	58.485°	6.05 ± 0.52	0.5%
16	249.882°	70.967°	10.28 ± 0.78	1.2%
15	273.334°	73.435°	7.51 ± 1.83	0.9%
13	315.112°	69.808°	8.84 ± 0.77	1.0%
11	332.370°	62.125°	8.44 ± 3.53	0.5%
9	348.825°	50.971°	11.28 ± 0.86	1.1%

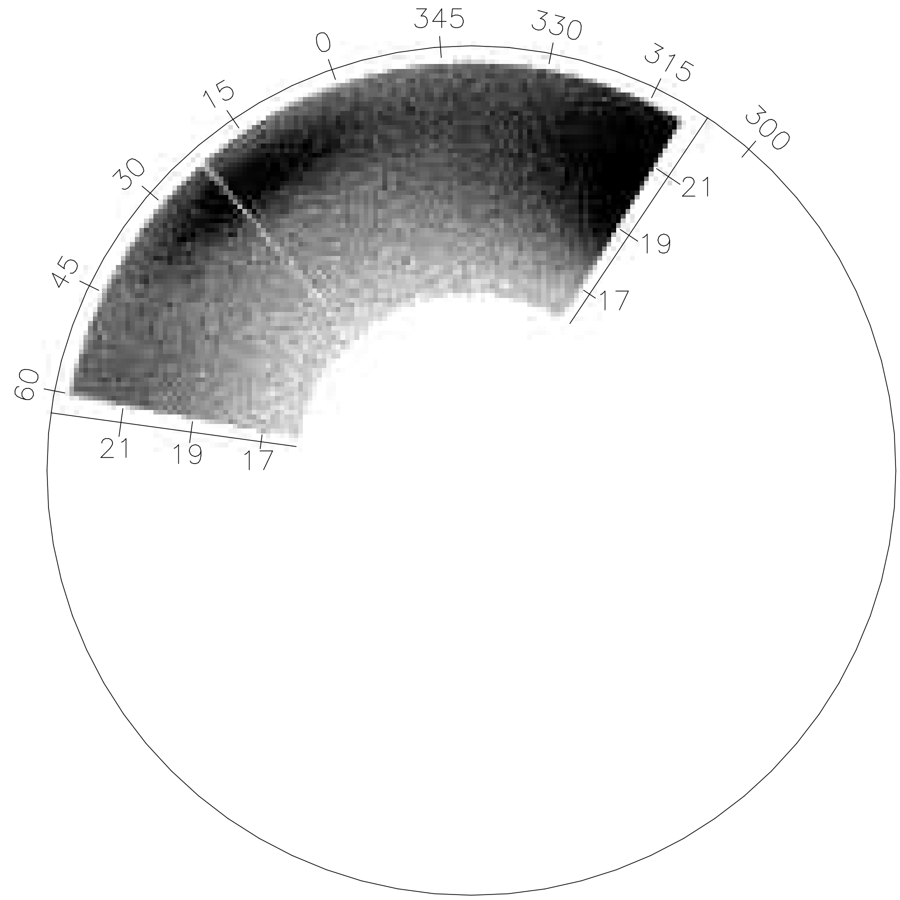

Figure 4.3: SDSS stripe 86 dataset density wedge plot. Plotted here, in the same manner as figure 4.1, is the 111,642 F turnoff stars within the volume limits of SDSS stripe 86. The angle about the stripe, μ, is limited here to $310° < \mu < 420°(60°)$. A small angle of data $21.6° < \mu < 22.3°$ needed to be removed and can be seen passing through the Sgr tidal debris. This debris easily discernible at the approximate coordinates $(\mu, g_0) = (20°, 21.5)$.

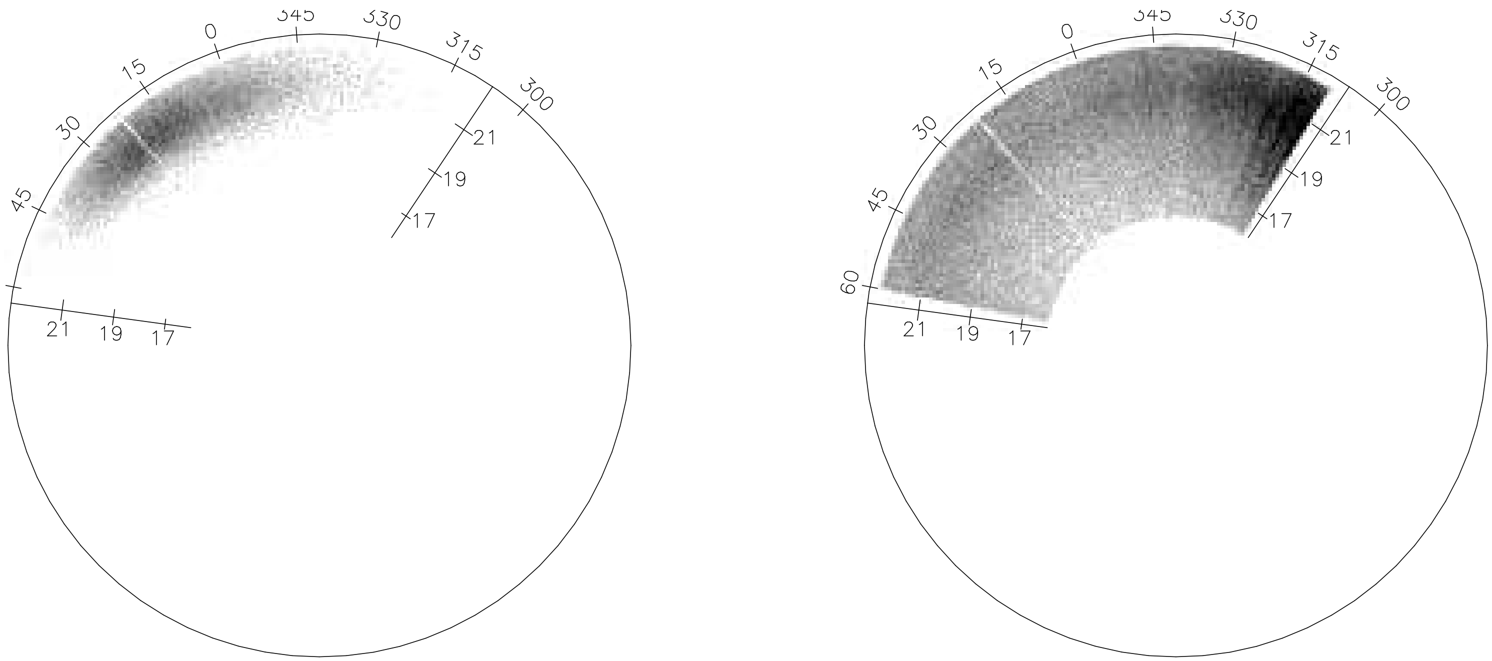

Figure 4.4: SDSS stripe 86 dataset separated density wedge plots. Plotted here, in the same manner as figure 4.1, is the same 92,789 star dataset as in figure 4.3, however, the stars have been plotted separately based upon the catalogs returned from the separation algorithm. Thus, the Sgr tidal stream (left) and the stellar spheroid (right) can be seen after the stream has been extracted. The Sgr stream has clearly been extracted from the stellar spheroid despite the removal of the volume that cuts straight through the stream.

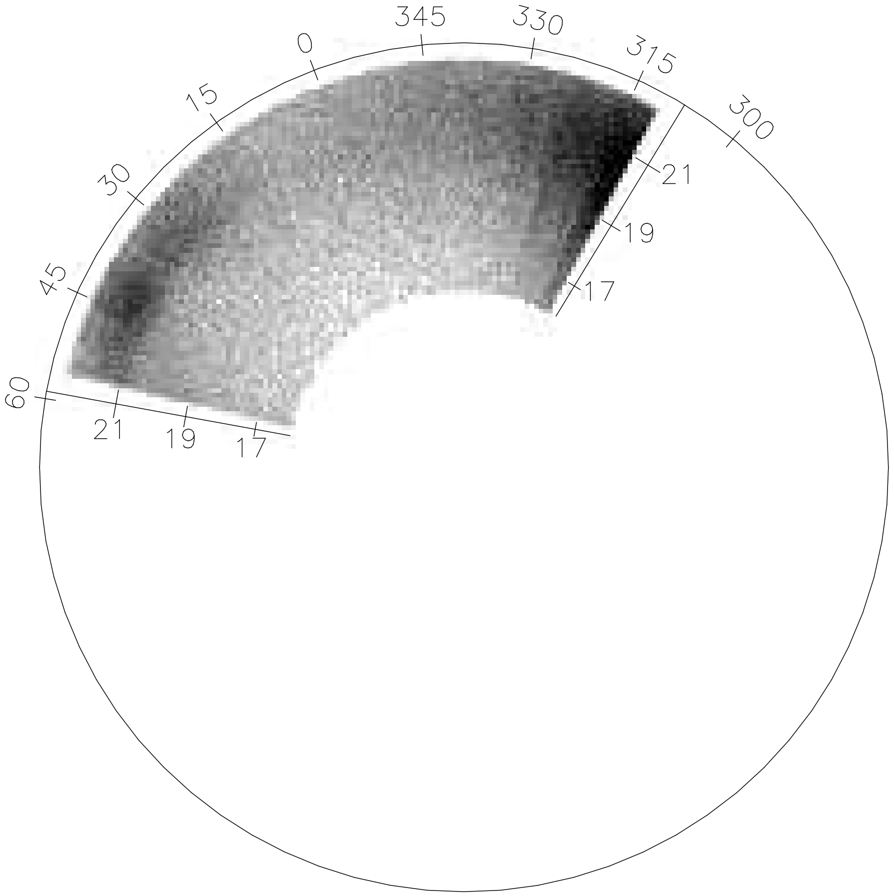

Figure 4.5: SDSS stripe 79 dataset density wedge plot. Plotted here, in the same manner as figure 4.1, is the 92,789 F turnoff stars within the volume limits of SDSS stripe 79. The angle about the stripe, μ, is limited here to $311° < \mu < 416°(56°)$. The Sgr tidal stream is easily discernible at the approximate coordinates $(\mu, g_0) = (45°, 21.5)$.

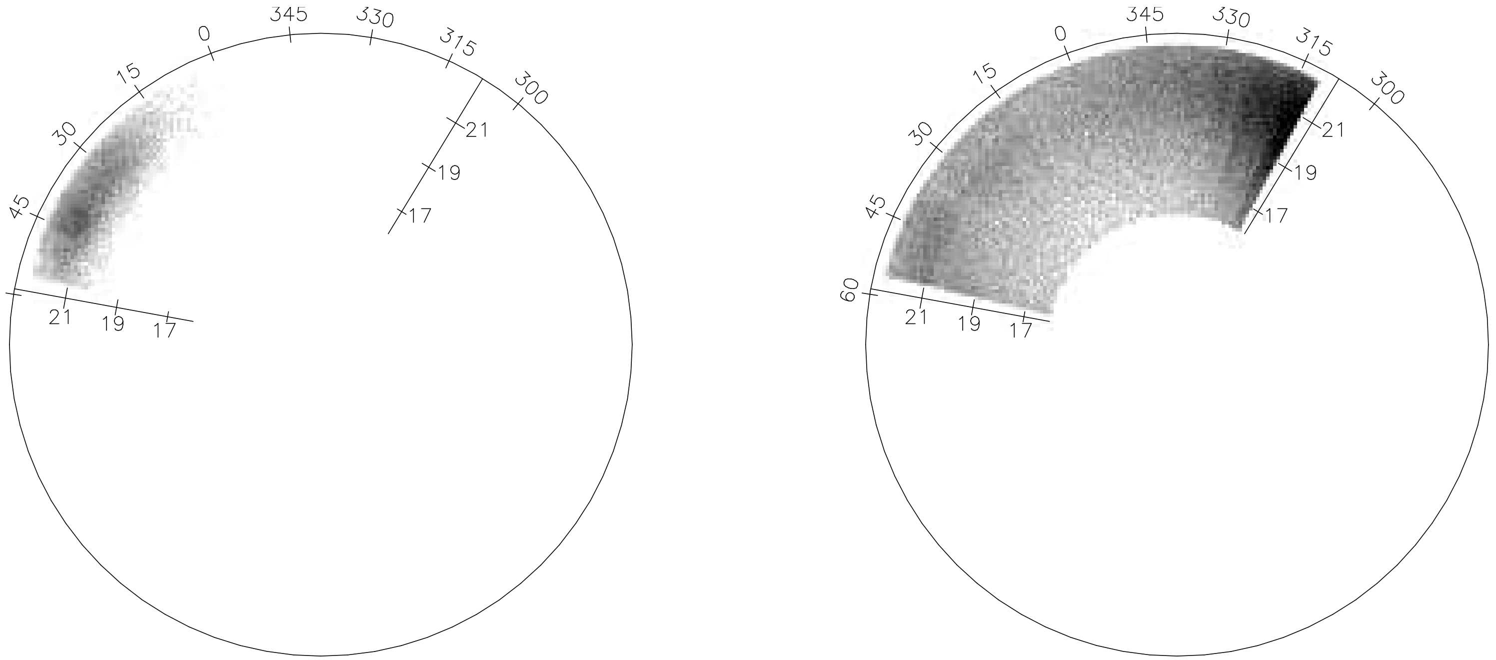

Figure 4.6: SDSS stripe 79 dataset separated density wedge plots. Plotted here, in the same manner as figure 4.1, is the same 92,789 star dataset as in figure 4.5, however, the stars have been plotted separately based upon the catalogs returned from the separation algorithm. Thus, the Sgr tidal stream (left) and the stellar spheroid (right) can be seen after the stream has been extracted. The Sgr stream has clearly been extracted from the stellar spheroid.

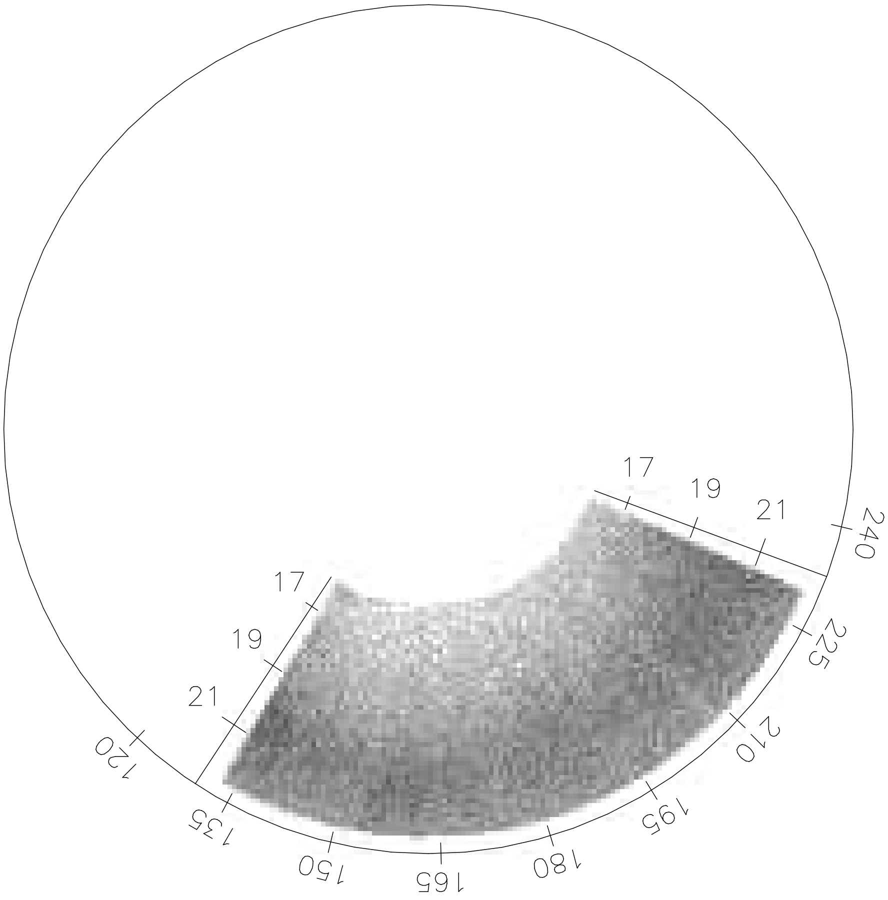

Figure 4.7: SDSS stripe 23 dataset density wedge plot. Plotted here, in the same manner as figure 4.1, is the 65,336 F turnoff stars within the volume limits of SDSS stripe 23. The angle about the stripe, μ, is limited here to $133° < \mu < 230°$.

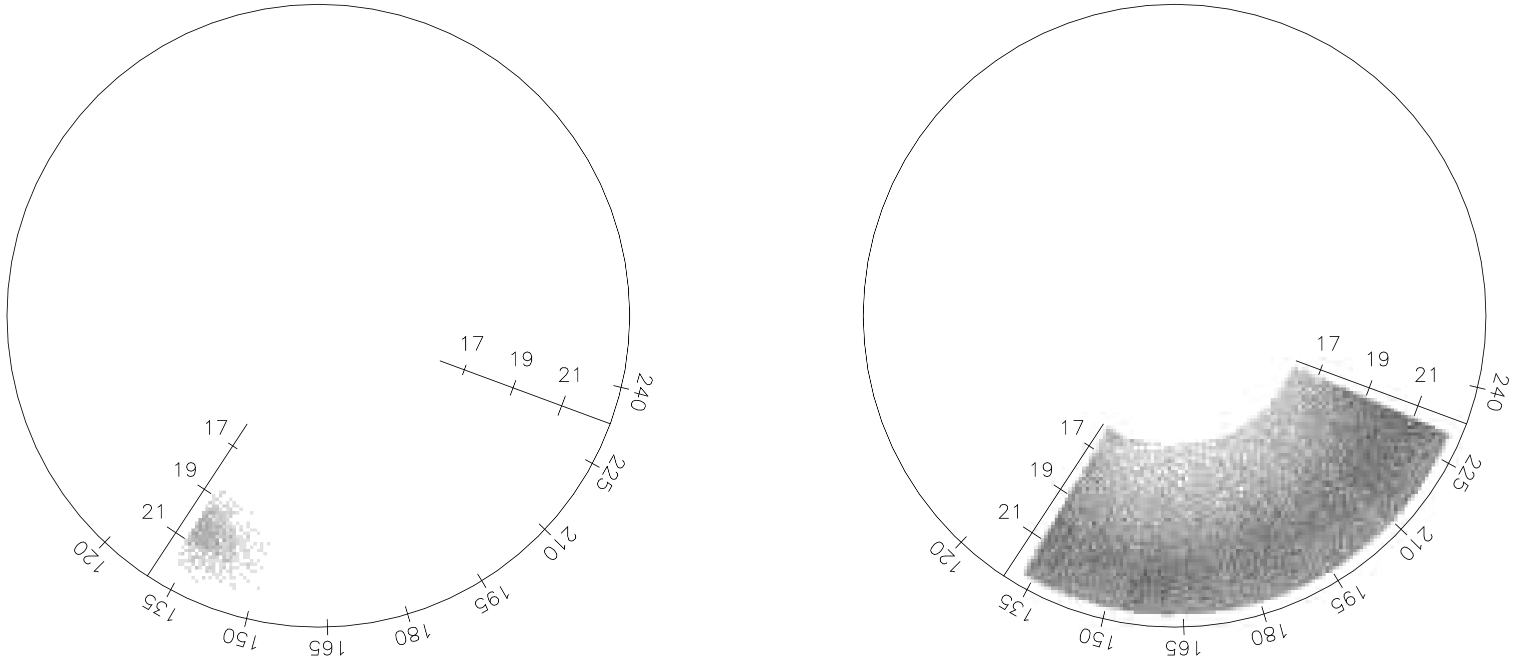

Figure 4.8: SDSS stripe 23 dataset separated density wedge plots. Plotted here, in the same manner as figure 4.1, is the same 65,336 star dataset as in figure 4.7, however, the stars have been plotted separately based upon the catalogs returned from the separation algorithm. Thus, the Sgr tidal stream (left) and the stars remaining after extracting those Sgr stream stars (right) can be seen. The Sgr stream has clearly been extracted from the background distribution.

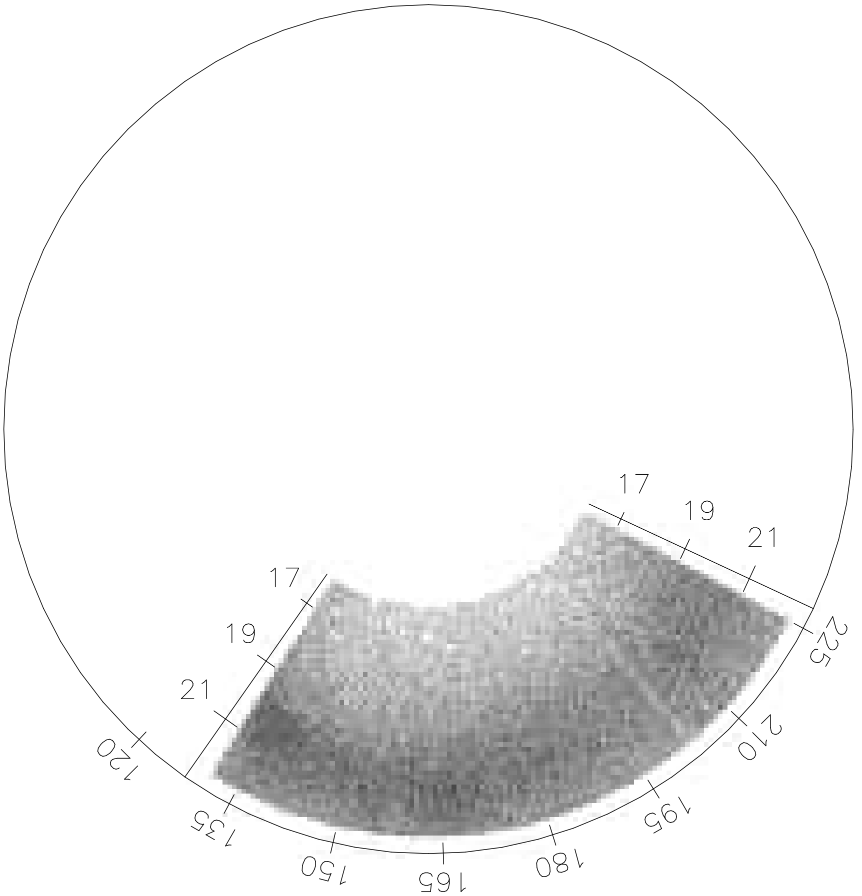

Figure 4.9: SDSS stripe 22 dataset density wedge plot. Plotted here, in the same manner as figure 4.1, is the 66,201 F turnoff stars within the volume limits of SDSS stripe 22. The angle about the stripe, μ, is limited here to $131° < \mu < 225°$.

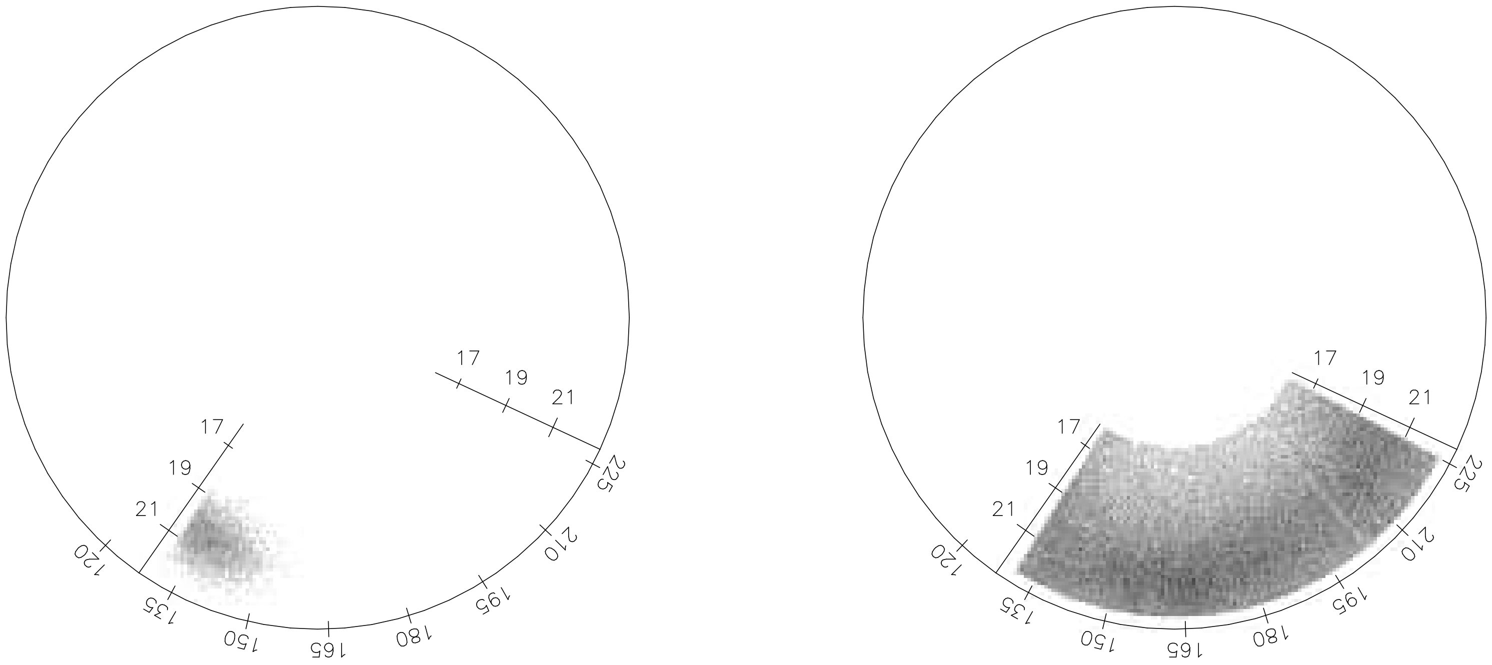

Figure 4.10: SDSS stripe 22 dataset separated density wedge plots. Plotted here, in the same manner as figure 4.1, is the same 66,201 star dataset as in figure 4.9, however, the stars have been plotted separately based upon the catalogs returned from the separation algorithm. Thus, the Sgr tidal stream (left) and the stars remaining after extracting those Sgr stream stars (right) can be seen. The Sgr stream has clearly been extracted from the background distribution.

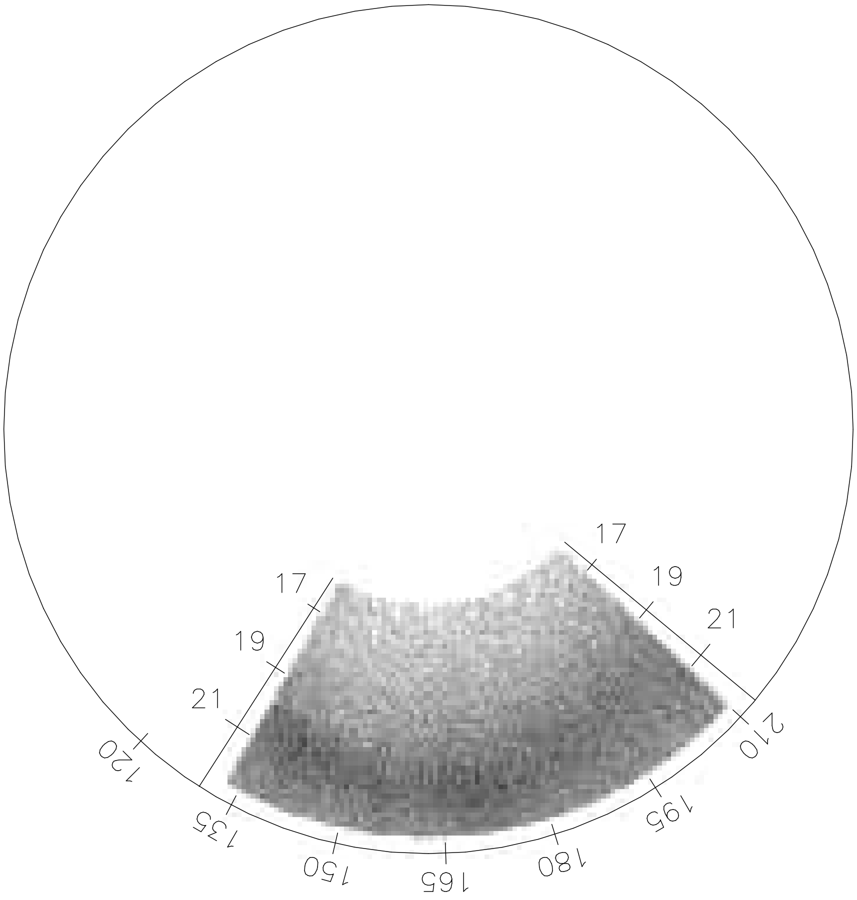

Figure 4.11: SDSS stripe 21 dataset density wedge plot. Plotted here, in the same manner as figure 4.1, is the 60,503 F turnoff stars within the volume limits of SDSS stripe 21. The angle about the stripe, μ, is limited here to $133° < \mu < 210°$.

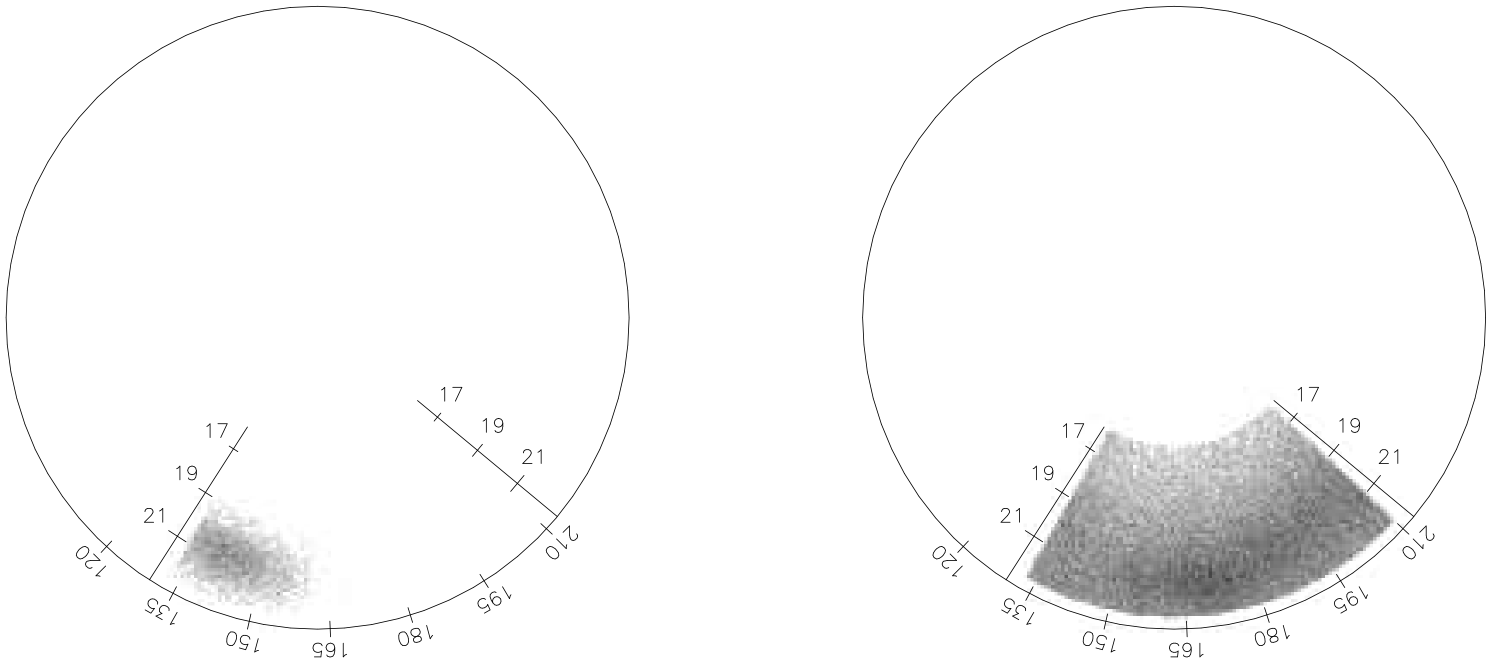

Figure 4.12: SDSS stripe 21 dataset separated density wedge plots. Plotted here, in the same manner as figure 4.1, is the same 60,503 star dataset as in figure 4.11, however, the stars have been plotted separately based upon the catalogs returned from the separation algorithm. Thus, the Sgr tidal stream (left) and the stars remaining after extracting those Sgr stream stars (right) can be seen. The Sgr stream has clearly been extracted from the background distribution.

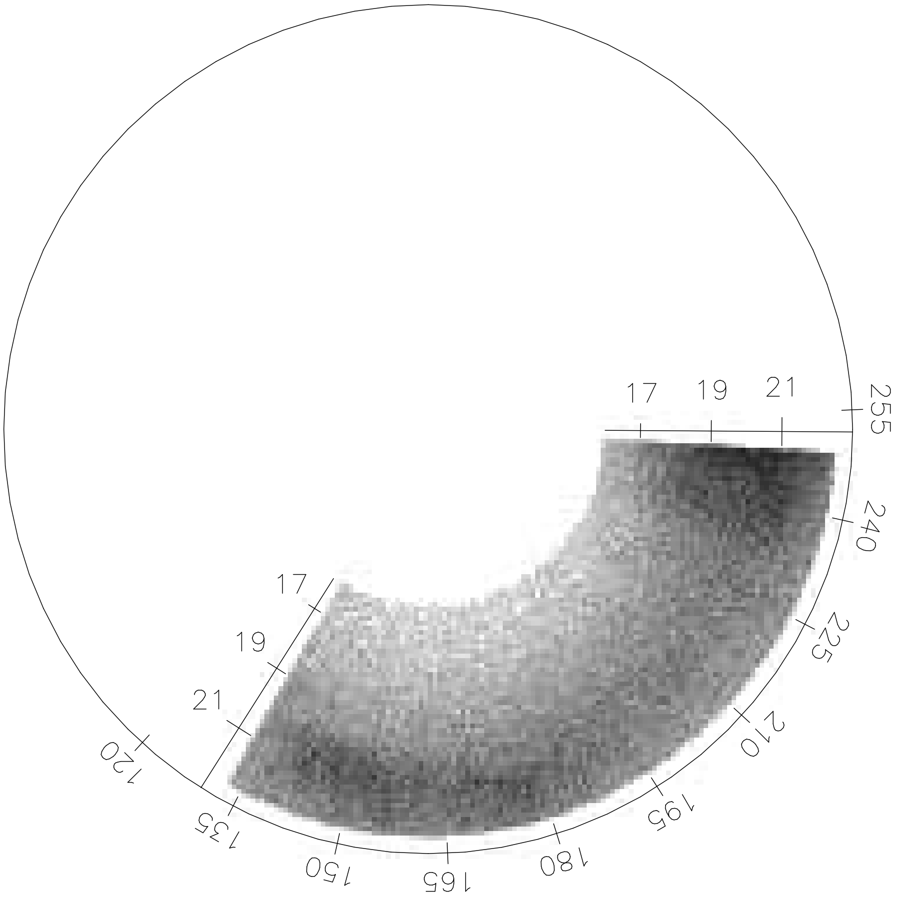

Figure 4.13: SDSS stripe 20 dataset density wedge plot. Plotted here, in the same manner as figure 4.1, is the 105,909 F turnoff stars within the volume limits of SDSS stripe 20. The angle about the stripe, μ, is limited here to $133° < \mu < 249°$.

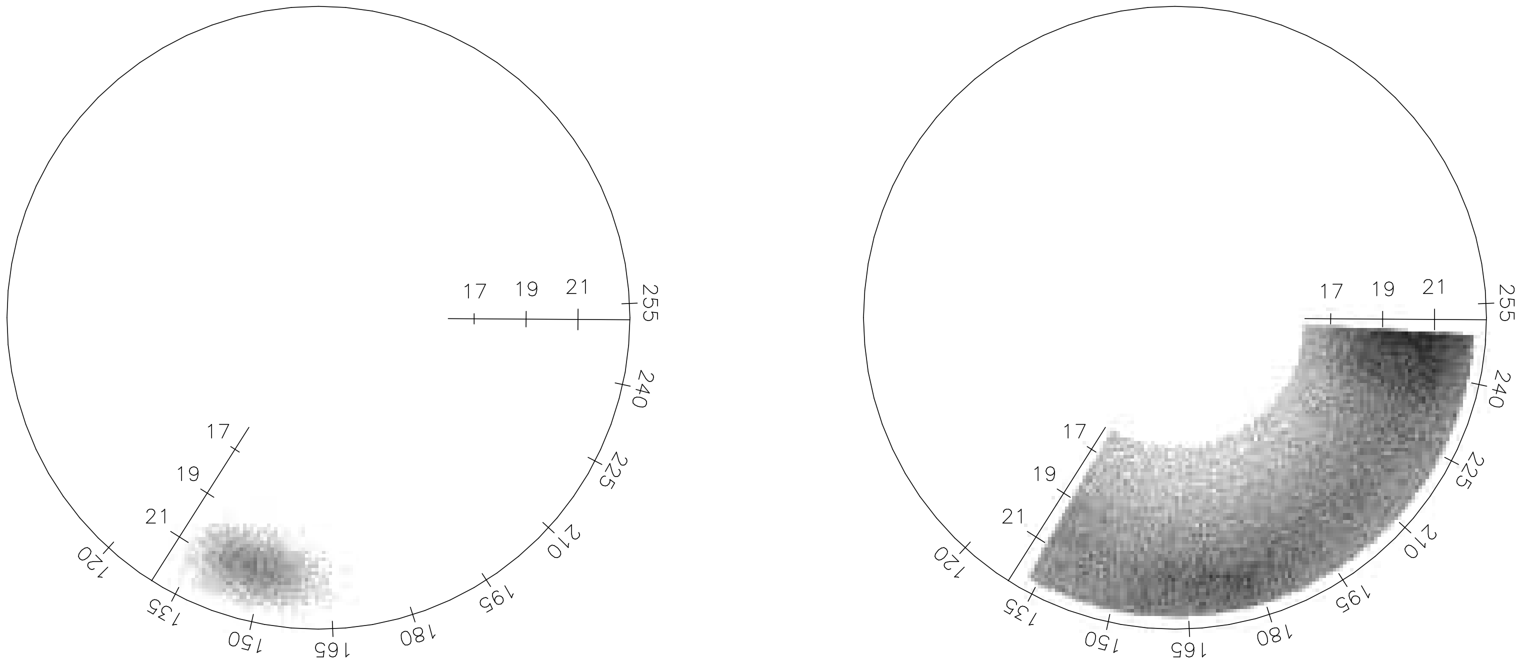

Figure 4.14: SDSS stripe 20 dataset separated density wedge plots. Plotted here, in the same manner as figure 4.1, is the same 105,909 star dataset as in figure 4.13, however, the stars have been plotted separately based upon the catalogs returned from the separation algorithm. Thus, the Sgr tidal stream (left) and the stars remaining after extracting those Sgr stream stars (right) can be seen. The Sgr stream has clearly been extracted from the background distribution.

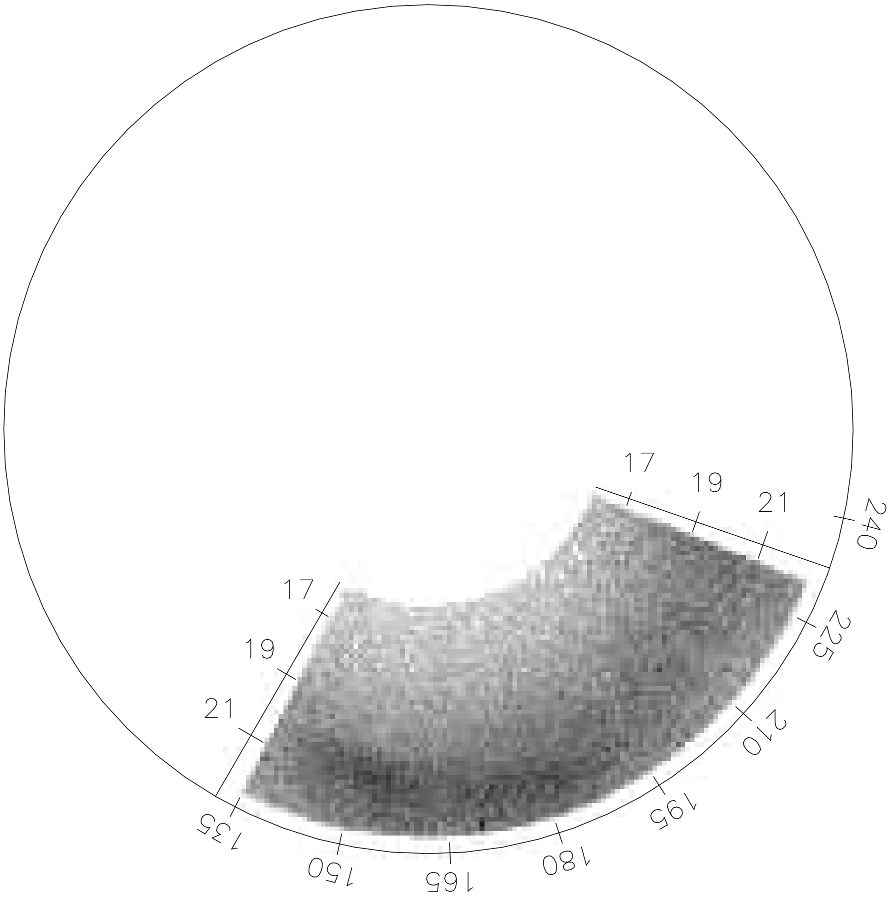

Figure 4.15: SDSS stripe 19 dataset density wedge plot. Plotted here, in the same manner as figure 4.1, is the 84,046 F turnoff stars within the volume limits of SDSS stripe 19. The angle about the stripe, μ, is limited here to $135^\circ < \mu < 230^\circ$.

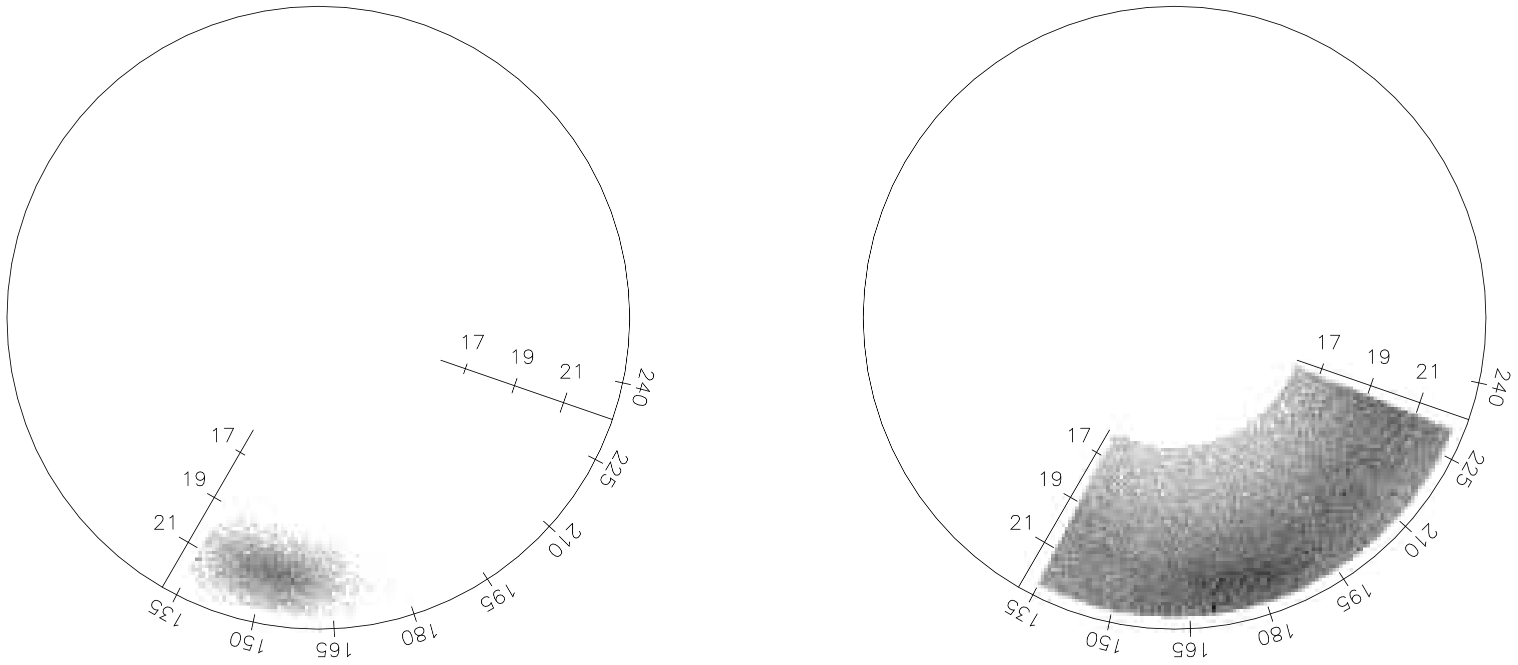

Figure 4.16: SDSS stripe 19 dataset separated density wedge plots. Plotted here, in the same manner as figure 4.1, is the same 84,046 star dataset as in figure 4.15, however, the stars have been plotted separately based upon the catalogs returned from the separation algorithm. Thus, the Sgr tidal stream (left) and the stars remaining after extracting those Sgr stream stars (right) can be seen. The Sgr stream has clearly been extracted from the background distribution.

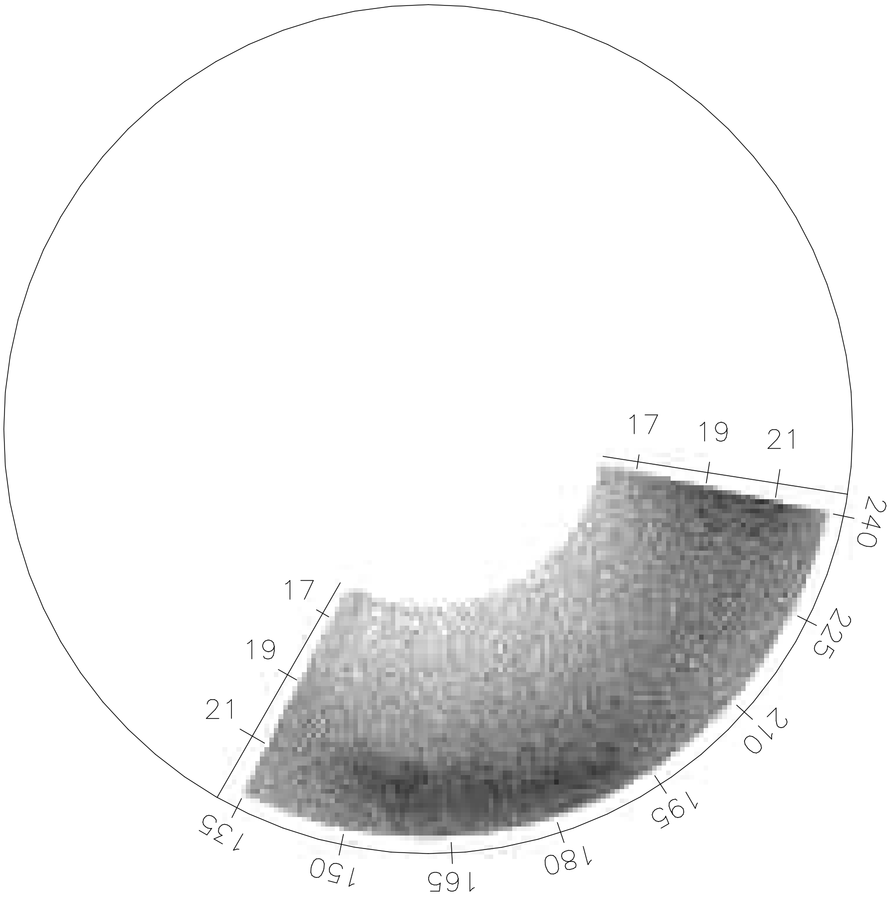

Figure 4.17: SDSS stripe 18 dataset density wedge plot. Plotted here, in the same manner as figure 4.1, is the 95,462 F turnoff stars within the volume limits of SDSS stripe 18. The angle about the stripe, μ, is limited here to $135° < \mu < 240°$.

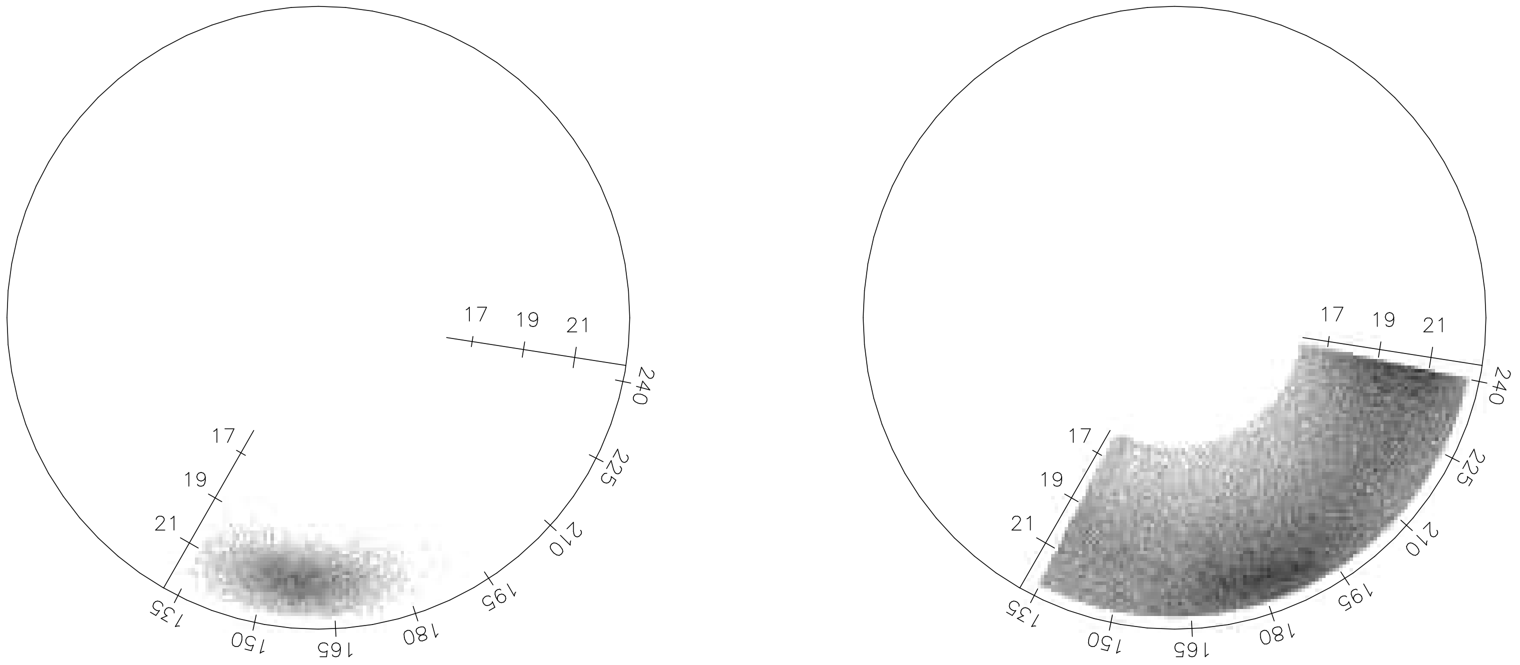

Figure 4.18: SDSS stripe 18 dataset separated density wedge plots. Plotted here, in the same manner as figure 4.1, is the same 95,462 star dataset as in figure 4.17, however, the stars have been plotted separately based upon the catalogs returned from the separation algorithm. Thus, the Sgr tidal stream (left) and the stars remaining after extracting those Sgr stream stars (right) can be seen. The Sgr stream has clearly been extracted from the background distribution.

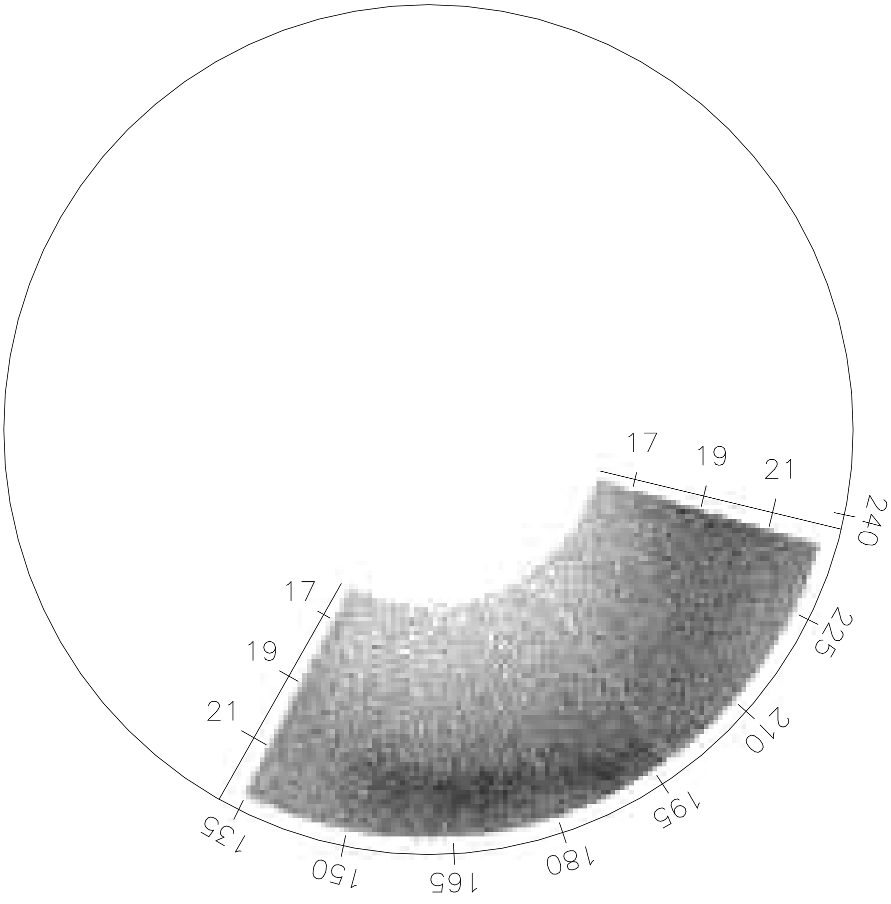

Figure 4.19: SDSS stripe 17 dataset density wedge plot. Plotted here, in the same manner as figure 4.1, is the 91,626 F turnoff stars within the volume limits of SDSS stripe 17. The angle about the stripe, μ, is limited here to $135° < \mu < 235°$.

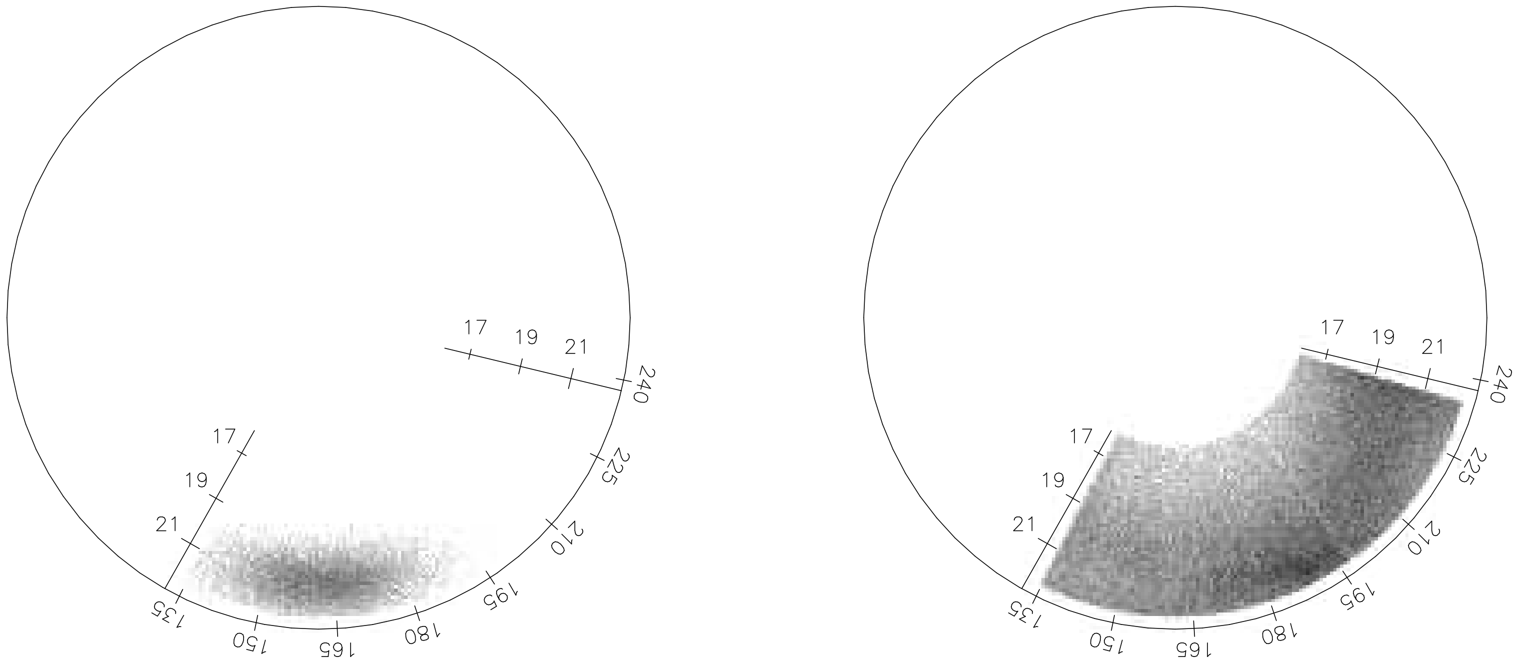

Figure 4.20: SDSS stripe 17 dataset separated density wedge plots. Plotted here, in the same manner as figure 4.1, is the same 91,626 star dataset as in figure 4.19, however, the stars have been plotted separately based upon the catalogs returned from the separation algorithm. Thus, the Sgr tidal stream (left) and the stars remaining after extracting those Sgr stream stars (right) can be seen. The Sgr stream has clearly been extracted from the background distribution.

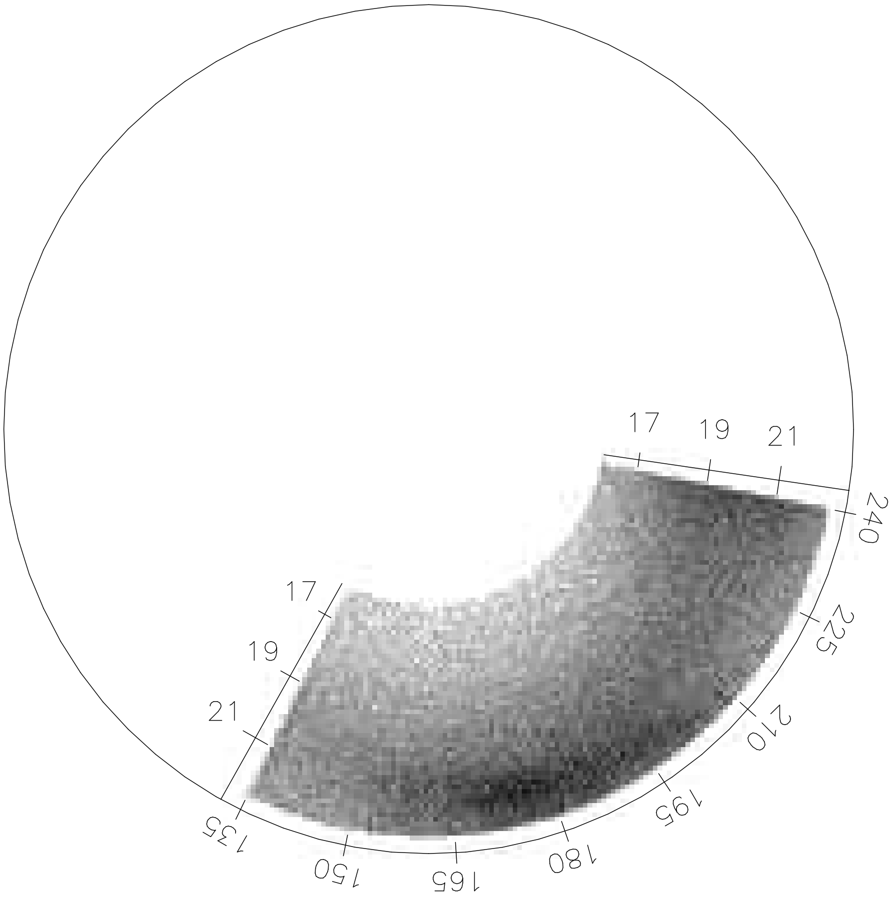

Figure 4.21: SDSS stripe 16 dataset density wedge plot. Plotted here, in the same manner as figure 4.1, is the 107,033 F turnoff stars within the volume limits of SDSS stripe 16. The angle about the stripe, μ, is limited here to $135° < \mu < 240°$.

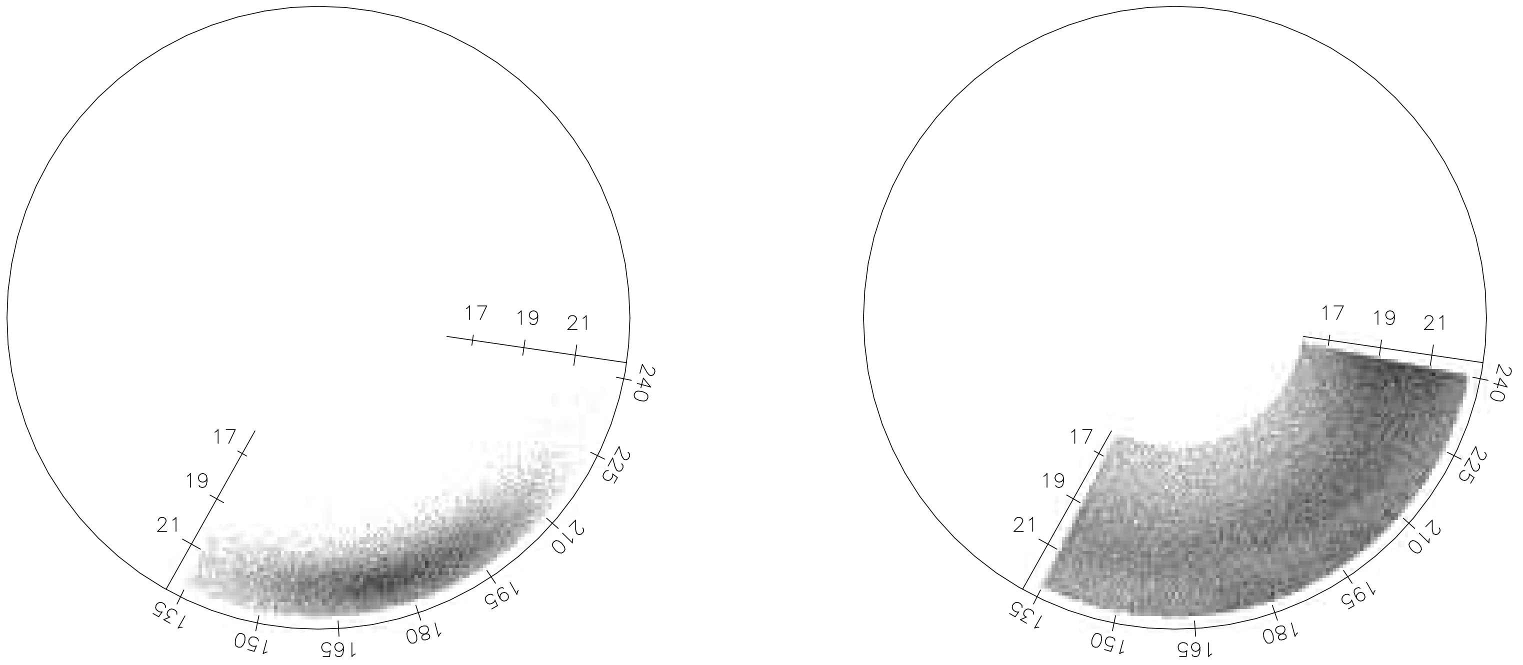

Figure 4.22: SDSS stripe 16 dataset separated density wedge plots. Plotted here, in the same manner as figure 4.1, is the same 107,033 star dataset as in figure 4.21, however, the stars have been plotted separately based upon the catalogs returned from the separation algorithm. Thus, the Sgr tidal stream (left) and the stars remaining after extracting those Sgr stream stars (right) can be seen. The Sgr stream has clearly been extracted from the background distribution.

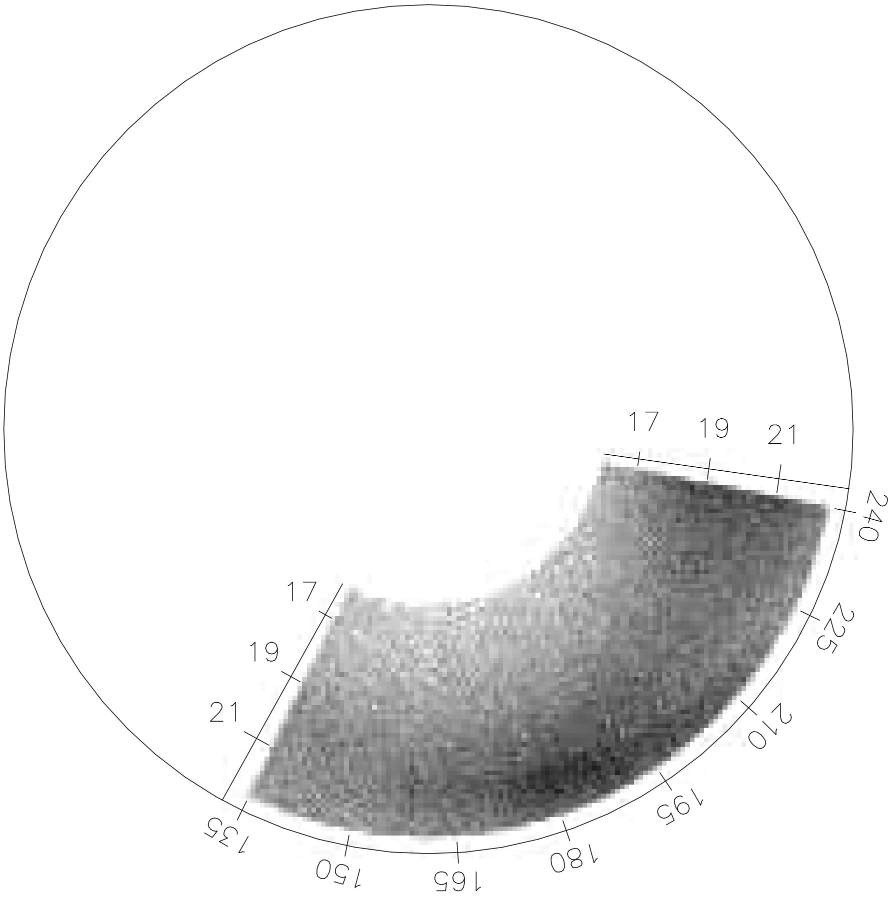

Figure 4.23: SDSS stripe 15 dataset density wedge plot. Plotted here, in the same manner as figure 4.1, is the 108,460 F turnoff stars within the volume limits of SDSS stripe 15. The angle about the stripe, μ, is limited here to $135^\circ < \mu < 240^\circ$.

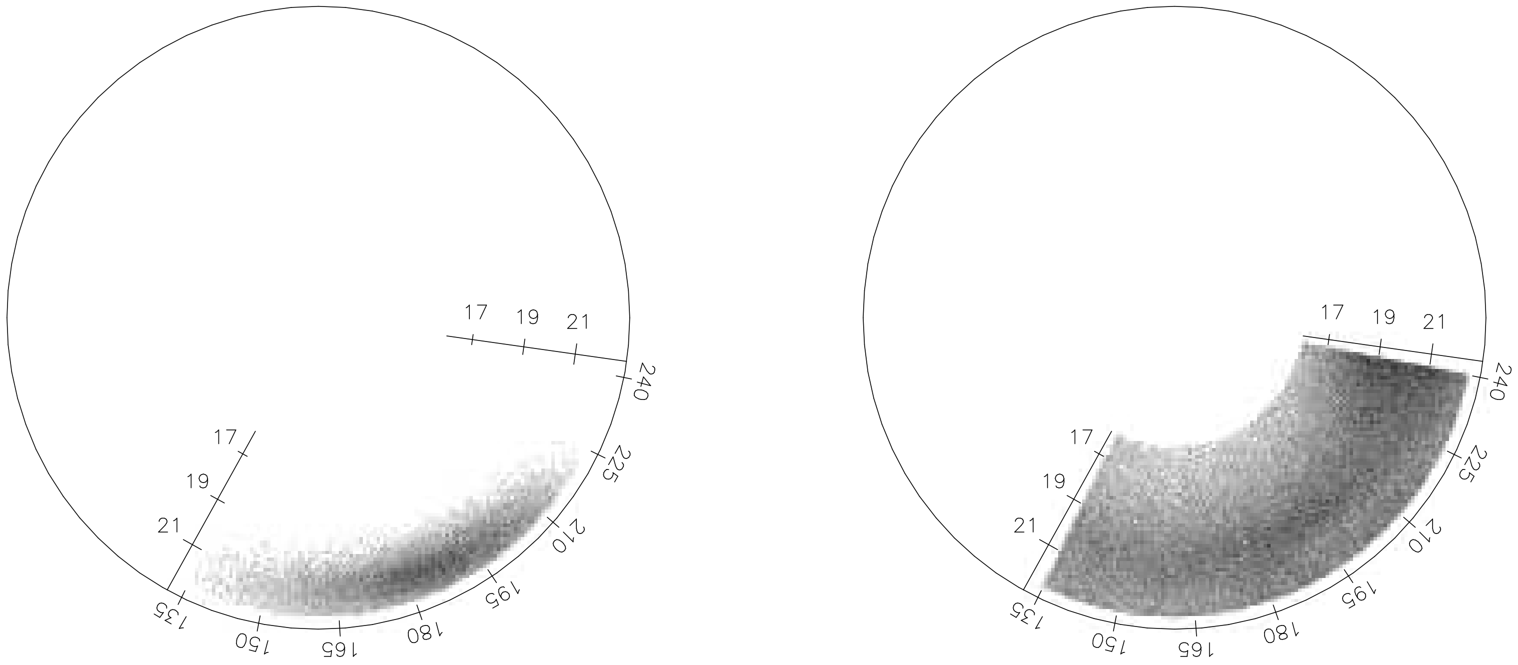

Figure 4.24: SDSS stripe 15 dataset separated density wedge plots. Plotted here, in the same manner as figure 4.1, is the same 108,460 star dataset as in figure 4.23, however, the stars have been plotted separately based upon the catalogs returned from the separation algorithm. Thus, the Sgr tidal stream (left) and the stars remaining after extracting those Sgr stream stars (right) can be seen. The Sgr stream has clearly been extracted from the background distribution.

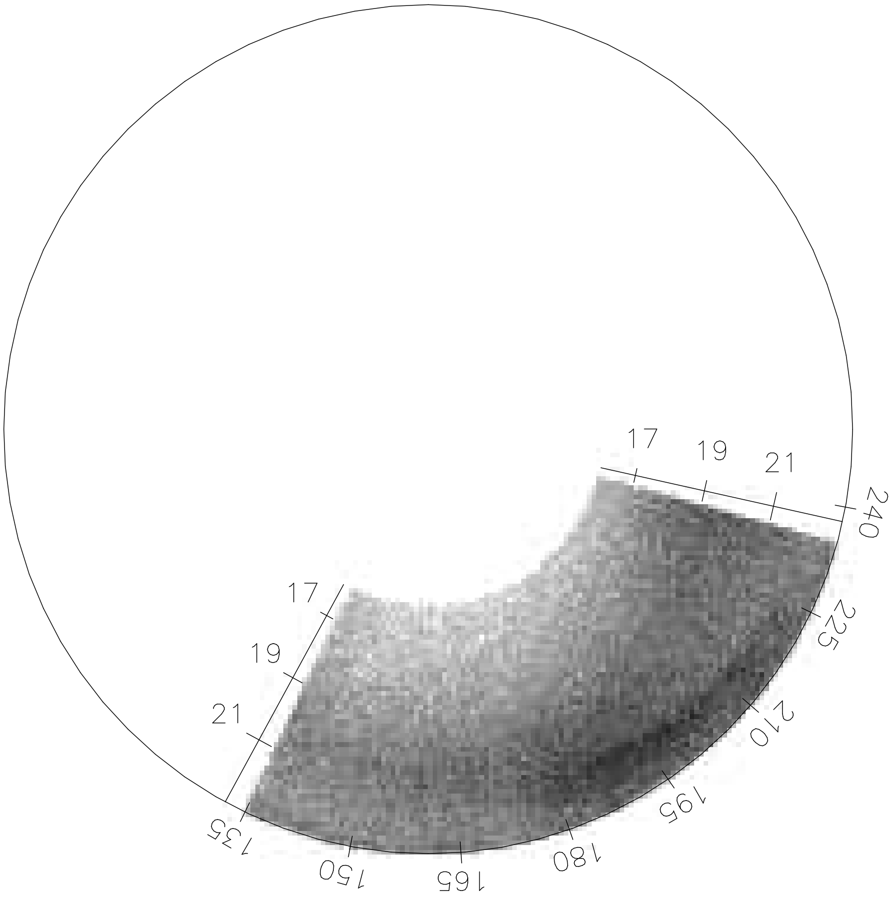

Figure 4.25: SDSS stripe 13 dataset density wedge plot. Plotted here, in the same manner as figure 4.1, is the 118,836 F turnoff stars within the volume limits of SDSS stripe 13. The angle about the stripe, μ, is limited here to $135° < \mu < 235°$.

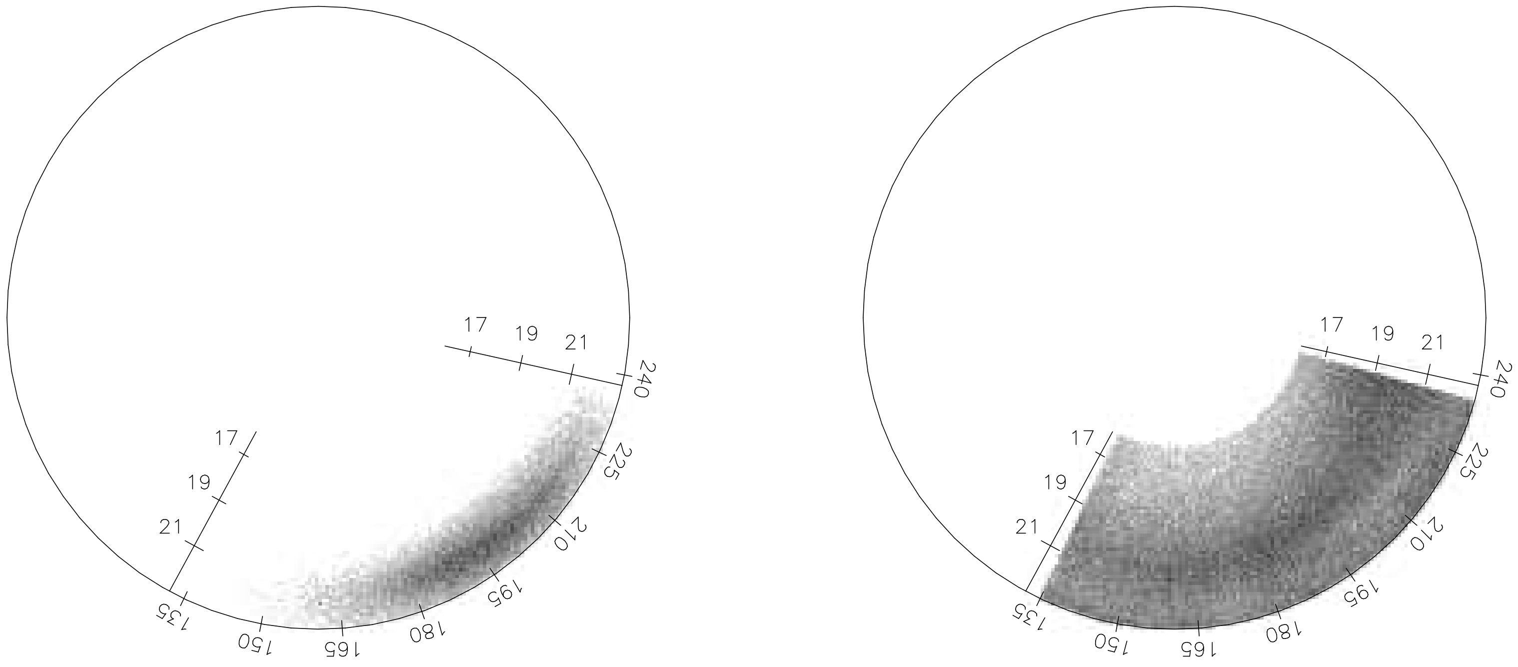

Figure 4.26: SDSS stripe 13 dataset separated density wedge plots. Plotted here, in the same manner as figure 4.1, is the same 118,836 star dataset as in figure 4.25, however, the stars have been plotted separately based upon the catalogs returned from the separation algorithm. Thus, the Sgr tidal stream (left) and the stars remaining after extracting those Sgr stream stars (right) can be seen. The Sgr stream has clearly been extracted from the background distribution.

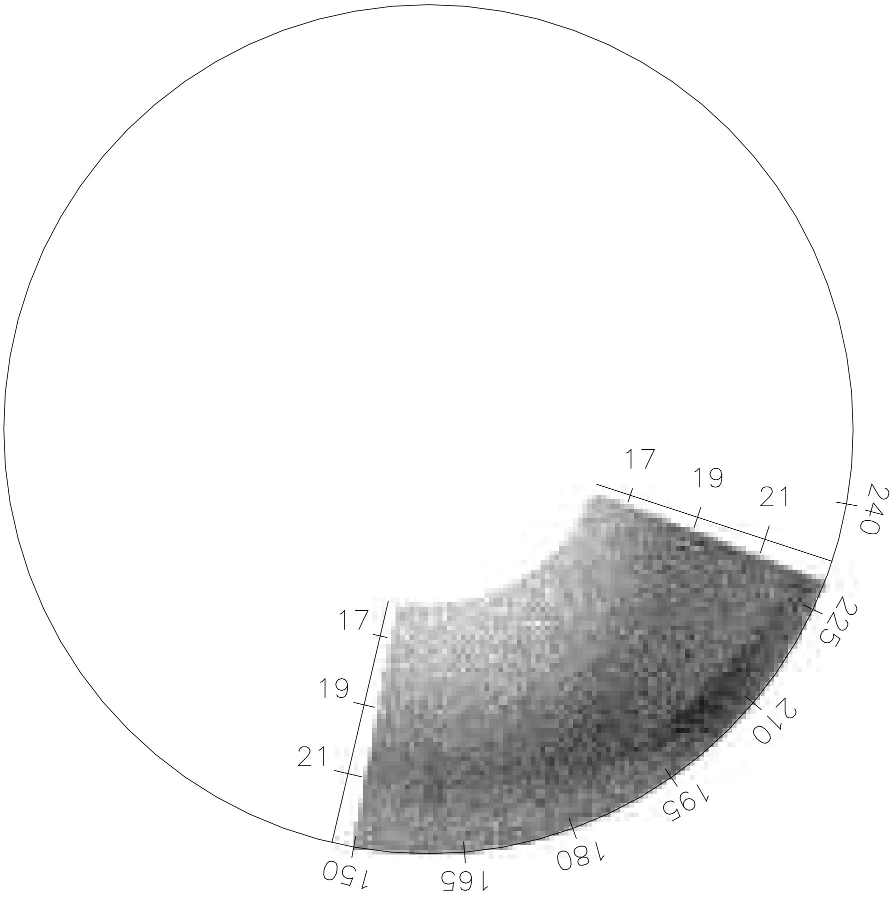

Figure 4.27: SDSS stripe 11 dataset density wedge plot. Plotted here, in the same manner as figure 4.1, is the 97,434 F turnoff stars within the volume limits of SDSS stripe 11. The angle about the stripe, μ, is limited here to $150° < \mu < 229°$.

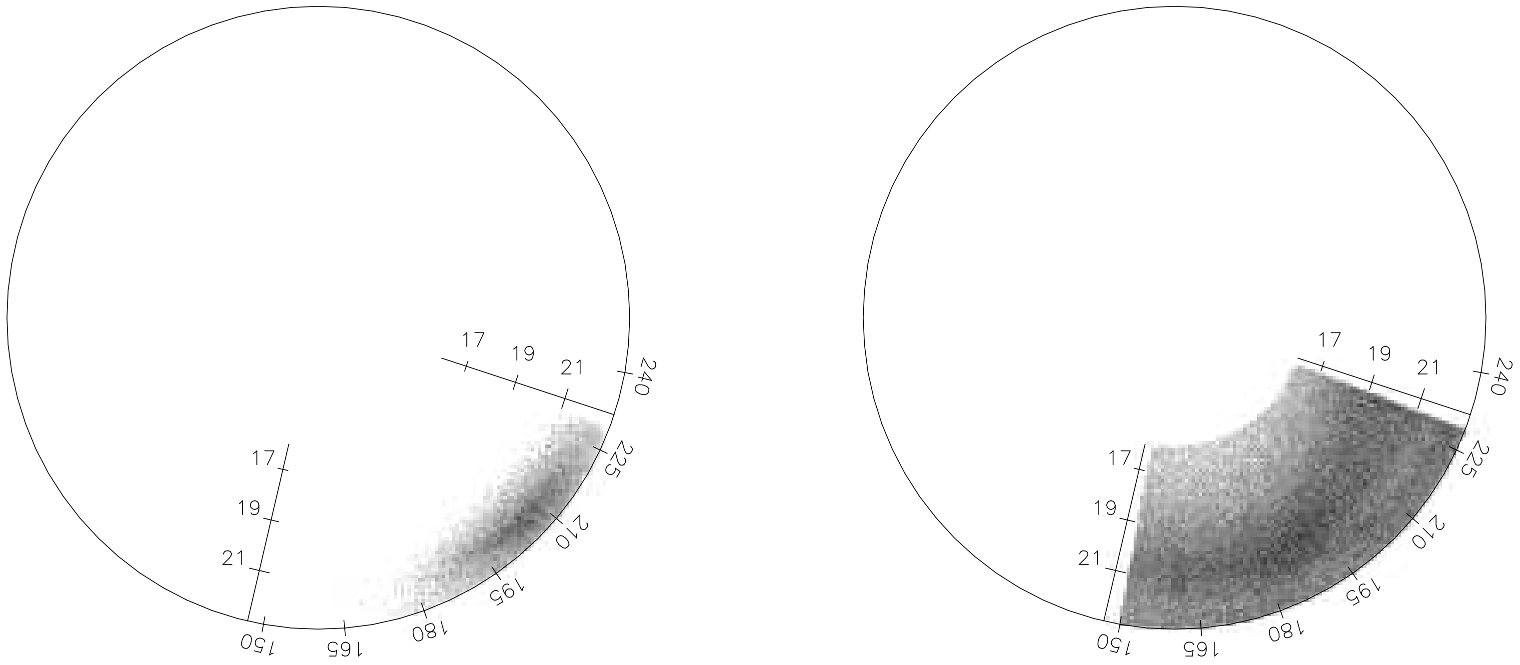

Figure 4.28: SDSS stripe 11 dataset separated density wedge plots. Plotted here, in the same manner as figure 4.1, is the same 97,434 star dataset as in figure 4.27, however, the stars have been plotted separately based upon the catalogs returned from the separation algorithm. Thus, the Sgr tidal stream (left) and the stars remaining after extracting those Sgr stream stars (right) can be seen. The Sgr stream has clearly been extracted from the background distribution.

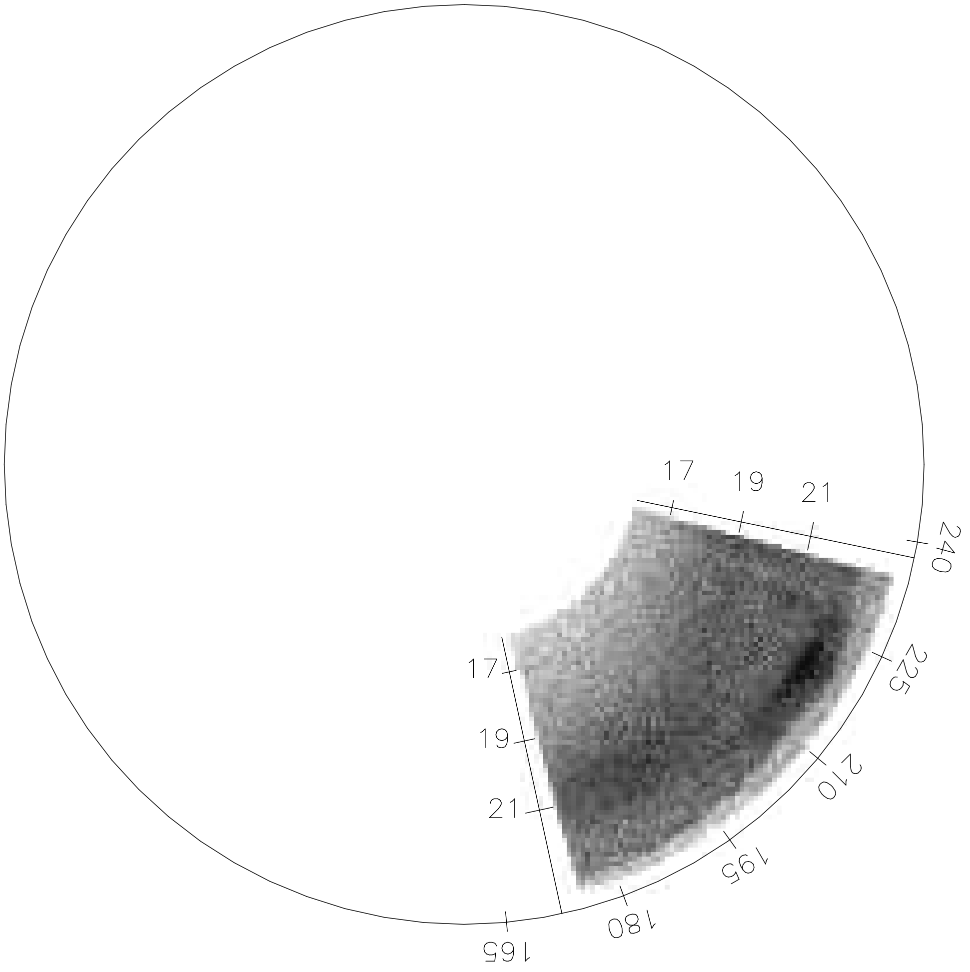

Figure 4.29: SDSS stripe 9 dataset density wedge plot. Plotted here, in the same manner as figure 4.1, is the 95,435 F turnoff stars within the volume limits of SDSS stripe 9. Due to the increased magnitude range the circle has been moved to constant magnitude $g_0 = 23.5$. The angle about the stripe, μ, is limited here to $170° < \mu < 235°$.

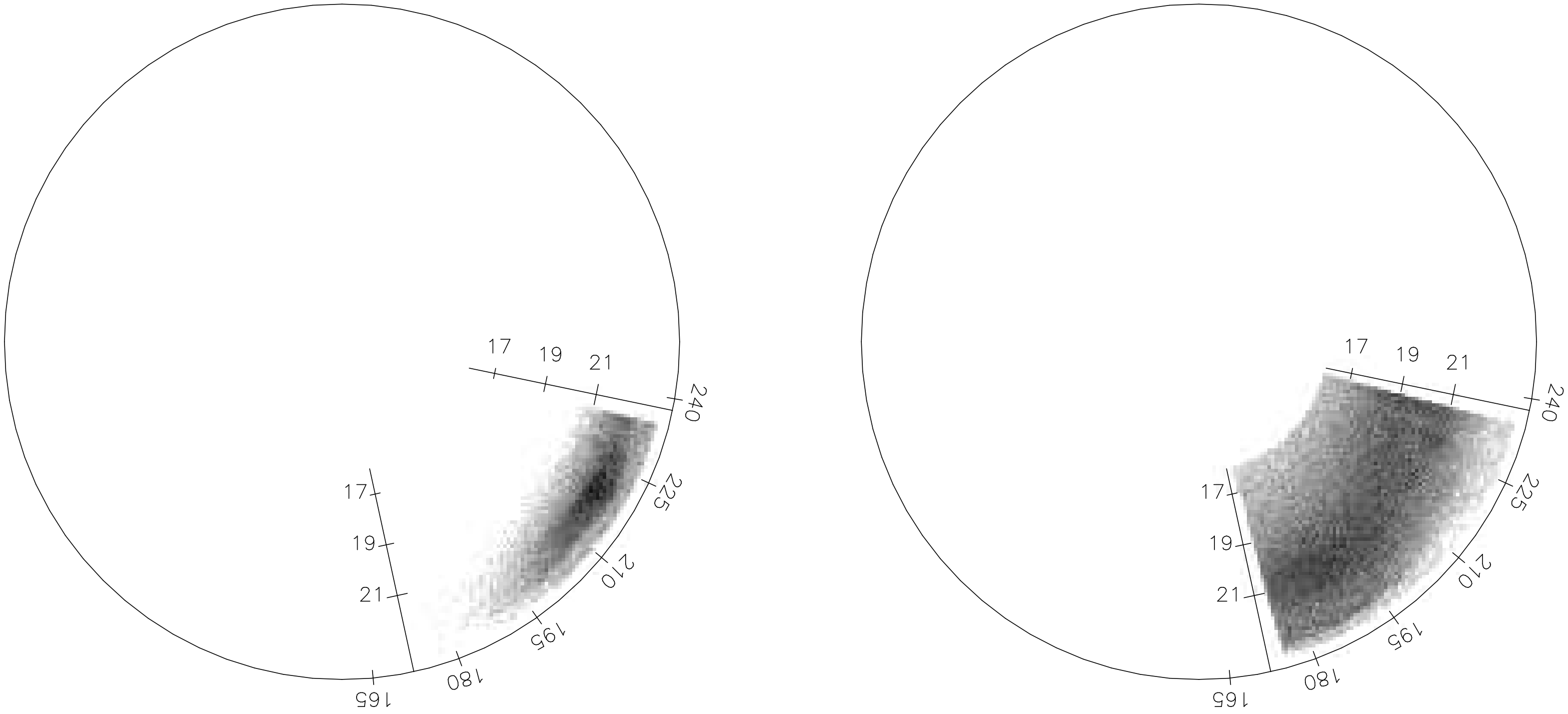

Figure 4.30: SDSS stripe 9 dataset separated density wedge plots. Plotted here, in the same manner as figure 4.1 but with the circle at constant magnitude $g_0 = 23.5$, is the same 95,435 star dataset as in figure 4.29, however, the stars have been plotted separately based upon the catalogs returned from the separation algorithm. Thus, the Sgr tidal stream (left) and the stars remaining after extracting those Sgr stream stars (right) can be seen. The Sgr stream has clearly been extracted from the background distribution.

CHAPTER 5
Discussion and Conclusions

Here the significance of the maximum likelihood results obtained in chapter 4 are reviewed. First, the integrated view of the Sgr leading and trailing tails are presented. Then, the results of the Hernquist profile fits are reviewed. Finally, the overall implications of this work will be covered.

5.1 The Sagittarius Tidal Stream

5.1.1 Trailing Tail

Previous authors [67] detected the position of the Sgr tidal debris within stripe 82 $(\alpha, R) = (33.99^\circ \pm 1^\circ, 29\ \text{kpc})$ using A colored blue horizontal branch (BHB) stars. The maximum likelihood result here shows a slight shift in angle to $(31.27^\circ \pm 0.25^\circ, 29.22 \pm 0.20\ \text{kpc})$. While the radial distance is consistent, the angular shift is slightly larger than expected but is not alarming, for the definition of the center of the stream is somewhat subjective and could introduce some error in this comparison. Also, the comparison between F turnoff stars and BHB stars may introduce more error in comparison should there be any amount of segregation in the type of star along the tidal stream. Finally, it should be noted that an angular position of $\alpha = 33^\circ$ was calculated for the Sgr stream within stripe 82 in F turnoff stars in [39], providing a much closer value to that found via the maximum likelihood method.

The direction of the Sgr stream in stripe 82 can also be compared to those results found in [90]. They estimate the angle between the observational plane and the Sgr stream to be 30° and the angle between the normal to the line of sight toward a point and the tangent of the stream at that point to be 10°. The first of these angles can be calculated from the "best-fit" parameters by calculating the angle between the directional vector, $\hat{a}$, and the observational plane of stripe 82. This is calculated to be $30^\circ \pm 03^\circ$, corresponding exactly with that found previously. The second of these angles can be calculated by finding the line-of-sight vector to the center of the stream, determining a normal to that, and then finding the angle between this normal and the stream directional vector, $\hat{a}$. This is calculated to be $22.5° \pm 2°$. This difference can be explained by the dramatic improvement in accuracy of the maximum likelihood method over that which can be accomplished by an estimate by eye for this angle which is much more difficult to determine.

The position of the tidal debris within stripe 86 was detected at $(l, b, R) = (134.776°, -72.342°, 26.077 \text{ kpc})$. This is significantly different from the detection in A colored stars in [67] of $(l, b, R) = (148.8°, -70.8°, 30 \text{ kpc})$. Since the maximum likelihood method is of higher accuracy, and the results fit much more consistently with a smooth path/orbit needed to connect the other trailing tail detections (stripe 79 and 82) with the Sgr core, the maximum likelihood measurement is believed to be correct.

The detection of the Sgr stream in stripe 79 completes the analysis of the trailing tidal tail in the South Galactic cap. The position and angle of the stream are consistent with a smooth orbit from the Sgr core through the three detections. The widths increase systematically, within the errors, the farther from the Sgr core the detection. This may imply that the stream grows in width and also decreases in density, with distance from the core of the disrupted galaxy. This decrease in density is seen most dramatically in the detection of stripe 79.

The three southern detections have been plotted with respect to the Sgr dSph orbital plane. Figure 5.1 shows the Sgr dSph orbital plane face on. The Sgr dSph orbital plane is roughly perpendicular to the Galactic plane, thus this figure roughly corresponds to viewing the Milky Way edge on. The tail of the arrows denote the detection of the tidal debris while the direction of the arrow corresponds to the spatial direction of the debris that was fit via the maximum likelihood algorithm. The length of the arrow is arbitrary and is simply a multiple of the directional unit vector $\hat{a}$. Similarly, the Sgr dSph orbital plane edge on can be seen in figure 5.2 which is similar to viewing the Milky Way face on. As can be seen in these two figures the detections the vast majority of the detections are in good agreement with each other.

Figure 5.3 views the Sgr dSph orbital plane face on and shows the detections

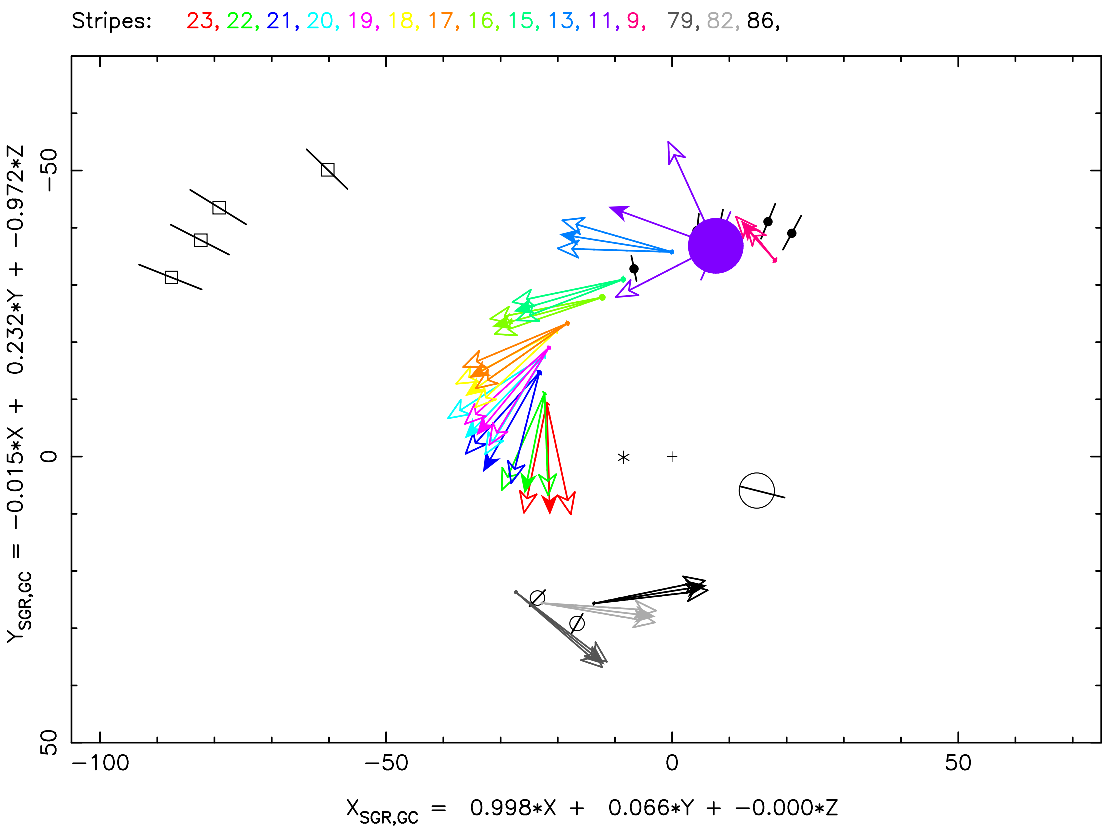

Figure 5.1: Plotted here is a reproduction of figure 3 from [67]. Overlayed are arrows denoting the position (tail) and spatial direction of the Sgr tidal debris for each SDSS stripe analyzed as calculated via the maximum likelihood algorithm. The fits seem reasonable within the errors to form a smooth orbit. From top right going counter-clockwise the stripes are 9,11,13,15-23 and 79, 82, and 86. 1-σ errors are shown in angle with outlined arrows while 1-σ errors in position are depicted with solid points (the larger of the angular and distance error is taken as the radius of the point).

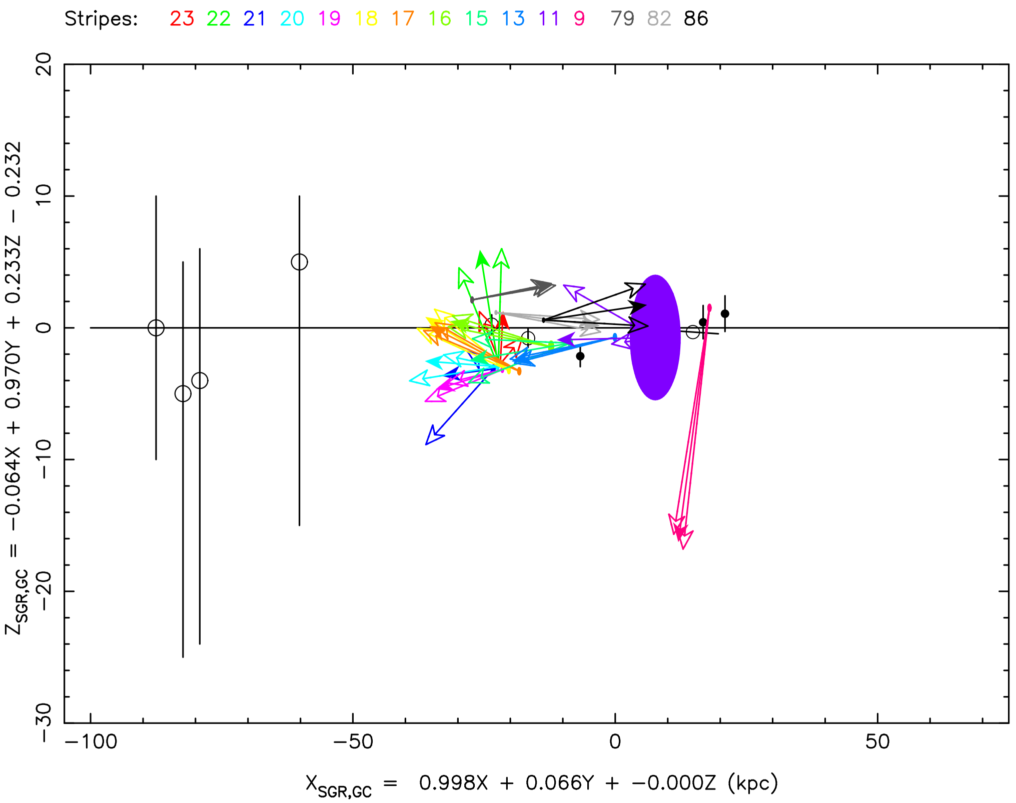

Figure 5.2: Plotted here is a reproduction of figure 4 from [67]. Overlayed are arrows denoting the position (tail) and spatial direction of the Sgr tidal debris for each SDSS stripe analyzed as calculated via the maximum likelihood algorithm. 1-σ errors are shown in angle with outlined arrows while 1-σ errors in position are depicted with solid points (the larger of the angular and distance error is taken as the radius of the point).The fits seem reasonable, within the errors, to lie within a reasonable orbital plane, aside from those fits for stripes 23, 22. In stripes 23 and 22 the Sgr stream occurs along the edge of the data which may influence the accuracy of the angle determination.

(position and direction) of the southern stripes. However it also depicts a subsampling of those stars determined to fit the density profile of the Sgr tidal stream via the separation algorithm. These observational results are then overlayed upon a simulation of the Sgr dSph disruption which replicates that found in [79]. It can be seen that the three detections in the trailing tail correspond very well with the trailing tail of the simulation.

5.1.2 The Leading Tail

The leading Sgr tidal stream is a very prominent feature in the northern SDSS data. The field of streams in [49] made this quite apparent and also discovered the bifurcated section of the Sgr tidal stream. This is a forking of the Sgr tidal stream which can be seen in figure 5.4 above the main Sgr branch on this plot, but is displayed much more prominently in the, now famous, field of streams image. This thesis is focused solely on fitting the main Sgr stream within the data. The bifurcated section was, in theory, fit during optimization since the northern SDSS data was fit with three simultaneous streams, but no action was taken to analyze these other streams as they were beyond the scope of this work.

Figure 5.1 depicts the positional and directional results of all optimizations to the northern SDSS data analyzed here. As can be seen the detections are in good agreement with each other, within the errors, and form a smooth orbit from stripe 23 to the Sgr core and around the trailing tidal tail. Figure 4 of [47] performed a similar study using F turnoff stars, by fitting the the turnoff of the Sgr stream. While the results presented in table 1 of [47] are, in general, very similar in Galactic latitude determinations for each of the stripes, there is considerable difference in Galactic longitude determinations. These differences seem to systematically grow, as the stream is traced from higher to lower stripe numbers. This corresponds with an increase in the distance of the Sgr tidal stream. A similar effect is observed in the distance determinations at each of these detections. The distances presented in [47] are consistently larger than those determined via the maximum likelihood method.

A possible explanation for this discrepancy could be that the fits performed in [47] were simultaneously fitting the main Sgr stream as well as its bifurcated

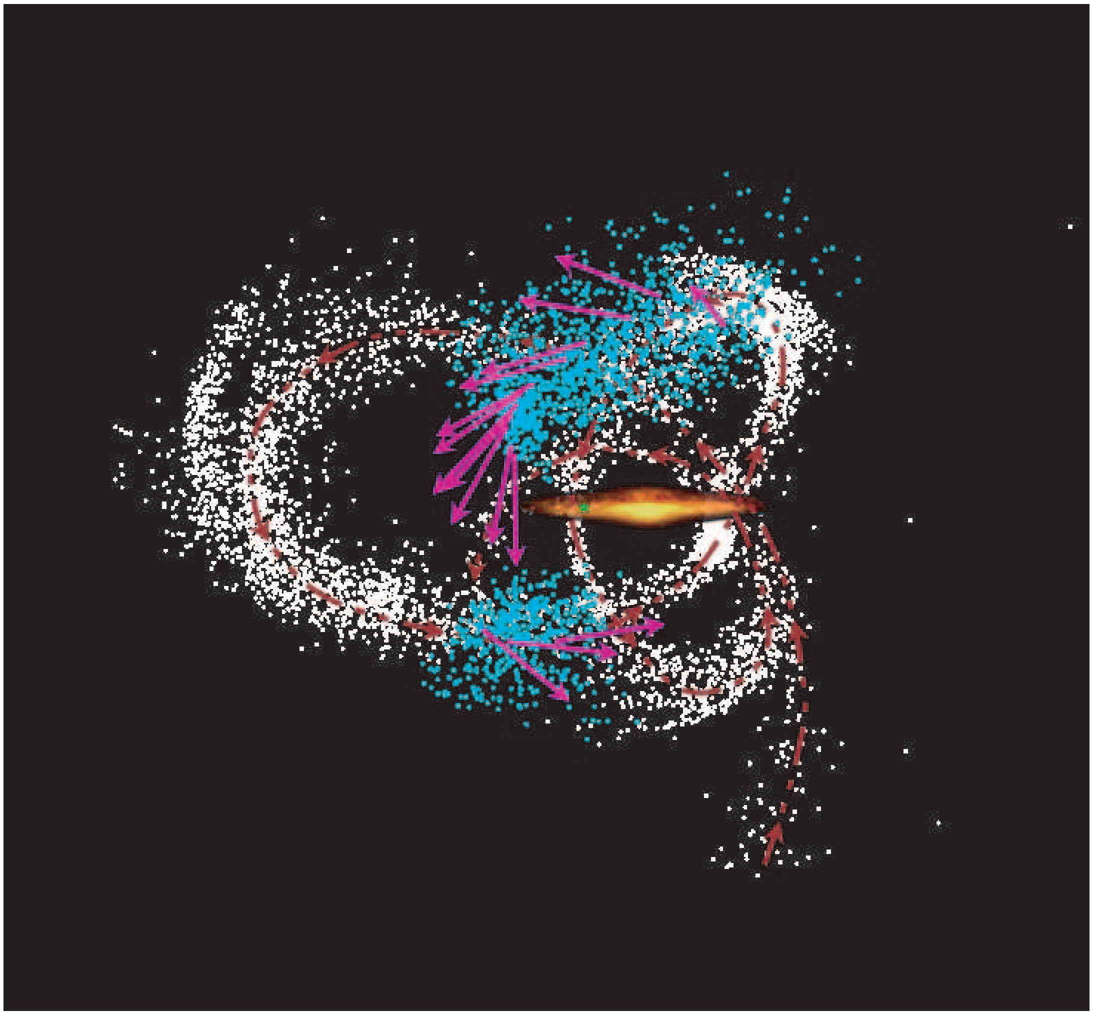

Figure 5.3: Plotted here is the Sgr dSph orbital plane face on. The green star denotes the Solar position while the galaxy is consistent in size and shape with the Milky Way. The white dots are simulated stars of the Sgr dSph disruption consistent with that found in [79]. The dotted red arrow shows the orbital path of the Sgr dSph during the simulated disruption. The pink arrows denote the position (tail) and spatial direction of the Sgr tidal debris for each SDSS stripe analyzed as calculated via the maximum likelihood algorithm. The cyan points are a subsampling of those stars found to fit the density profile of the Sgr tidal stream. From top right going counter-clockwise the stripes are 9, 11, 13, 15-23 and 79, 82, and 86. The trailing tail of the simulation fits the observational data very while; however, the leading tail clearly does not match the observational data.

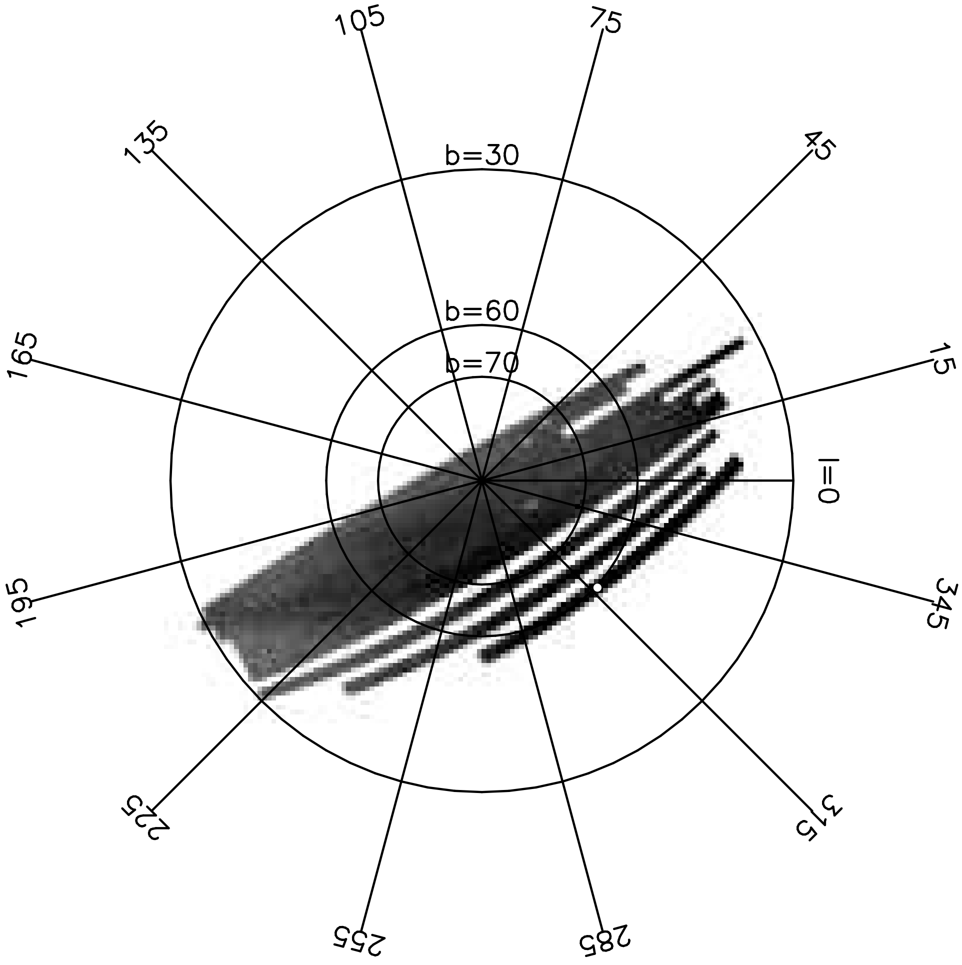

Figure 5.4: Density polar plot in Galactic coordinates of all Northern Galactic cap data analyzed via the maximum likelihood algorithm. Galactic latitude, b, is denoted along circles of constant radius while Galactic longitude is denoted by the azimuthal angle. The Sgr tidal stream can be seen as the overdensity that crosses the entirety of the data.

section. This would have the effect of moving the center of the detected structure further away, caused by the stream being much wider due to the combination of two distinct pieces of the stream. This effect could also explain the differing Galactic longitude determinations as well, for fitting the Sgr stream and its bifurcated section simultaneously at a larger distance would affect the determination of where on the sky the stream center is. For these reasons, it is difficult to compare the results presented in these two means. The stream appears to be well fit in both cases, however. This exemplifies the difficulty and need for determining a consistent definition of the "center" of a detection.

Figure 5.2 shows the detections via the maximum likelihood algorithm in the orbital plane of the Sgr orbital plane. It can be seen that the parameter determinations, in general, find a consistent direction within the plane. The major exceptions to this would be stripes 23, 22, and 9. The Sgr stream in stripes 23 and 22 occurs at the edge of the dataset analyzed; therefore, it is quite possible that the angle determination may be negatively affected in this instance. The Sgr stream debris in stripe 9 is at a much greater distance than any other stripe, and the efficiency function at this magnitude drops rapidly. For this reason it may simply be that an accurate angle determination under these conditions may be incredibly difficult or even unable to achieve.

As with the southern stripes, the detections in the north are presented with the simulated Sgr dSph disruption, and those stars fitting the stream density profile superimposed in figure 5.3. While the observations of the trailing tail agree very well with the simulation, the observations of the leading tidal tail differ dramatically from those seen in the simulation. This shows that the current models for the Sgr dSph disruption are flawed. Therefore, these models need to be updated to fit this newly available data and take advantage of the improved results.

5.2 Global Stream Analysis

Compiling the analyses of the number of F turnoff stars in the Sgr tidal stream versus the number seen currently in the Sgr dSph shows that within the fifteen stripes analyzed there are 9.0% the number of F turnoff stars currently in the stream as the core. This shows considerable disruption of the Sgr dSph, for this number represents only the stars in the stripes studies which is but a fraction of those stars in the tidal stream.

The width of the stream within all fifteen stripes has been plotted versus the angle along the stripe in figure 5.5. Angle along the stripe has been calculated, here, as the angle from the Sgr dSph core to the stream detection with positive angles representing the leading tail and negative angles representing the trailing tail. The trailing tail appears to show a trend in increasing width while the leading tail shows a distinct decrease in stream width with angle from the Sgr dSph. A possible explanation for this feature is would be the existence of the bifurcation in the leading tail. This bifurcation appears to cause the stream to break into two smaller streams; the separation between the two pieces becomes more prominent with angle along the stream. The width of the stream in the simulated disruption of the Sgr dSph within seven stripes, along the leading and trailing tails, are also plotted in figure 5.5. This simulated data follows the same trends as that seen in the observations: widths along the leading tail decrease with angle along the stream while there is evidence that the stream increases in width as the magnitude of the angle along the stream increases along the trailing tail.

The density of the stream within all fifteen stripes has been plotted versus the angle along the stripe in figure 5.6. Angle along the stripe is defined here as before, while the density is a linear density defined as the number of stars per kiloparsec along the stream at the detection point, corrected for the angle between the stripe and the stream, and then corrected for the thickness of the stripe at the detection distance because the farther away the stream the larger the volume subtended by the angle. A correction for edge effects, the tidal debris falling outside the angular stripe limits or the stream being far enough away to to lose stars due to falling survey efficiency at faint magnitudes have been taken into account here. The efficiency effect was corrected by binning the stars by distance and correcting the bins based on the efficiency function prior to the directional correction described above. If a portion of the stream was cut out due to the stripe limits, then the number of stream stars was correct by estimating the amount of stream that was

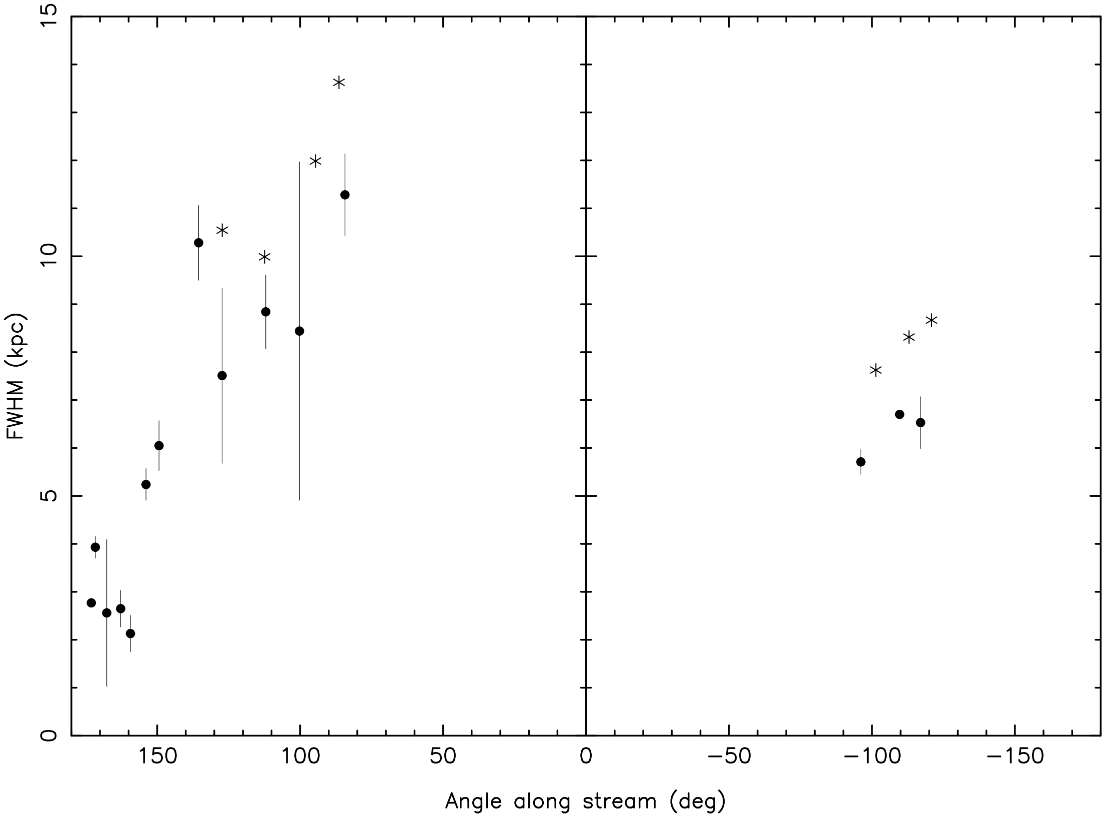

Figure 5.5: The width (FWHM) at each of the detections has been plotted versus the angle along the stream (solid dots) while the asterisks denote the width calculated in the model disruption of the Sgr dSph for those stripes. Here, angle along the stripe denotes the angle from the Sgr dSph core to the stream detection with positive angles representing the leading tail and negative angles representing the trailing tail. There is a clear trend in decreasing width as the magnitude of the angle increases along the stream in the leading tail and some evidence of the width increasing with the magnitude of the angle along the stream in the trailing tail. These trends are observed in the simulated data as well.

cut out based on symmetry.

There is a definitive trend that the stream density decreases with distance from the core. Densities were also calculated for the simulated disruption within seven stripes along the leading and trailing tail and plotted in figure 5.6. The decreasing trend in observed in the leading tail in the simulation, as well; however, the trailing tail shows a constant density in the simulation. Again, a clear need for improved models to match the data can be seen here.

From figure 5.2, it can be seen that the detections of the leading tidal tail lie along a consistent line as do the detections of the trailing tail, but that these are not consistent with the orbital plane of [69] which has equation

$$-0.064X + 0.970Y + 0.233Z + 0.232 = 0. \tag{5.1}$$

This implies that a new orbital plane is needed. Using all fifteen detections, a least squares method was applied to find the best fit plane to these points. The resulting plane has equation

$$-0.207X + 0.925Y + 0.319Z - 1.996 = 0 \tag{5.2}$$

and correlation value of 0.992. A similar fit was performed in the same manner but adding in the position of the Sgr dSph core for an eighteenth point. The plane resulting from this fit has equation

$$-0.159X 0.940Y + 0.302Z - 0.807 = 0 \tag{5.3}$$

and correlation value of 0.981. The fit with the Sgr core is closer to the original value of equation 5.1 and has a lower "goodness of fit" than that of the fit without the Sgr core. Attempts were made to align the Sgr dSph core with the plane of the leading tidal tail by adjusting the distance and angular position on the sky (within reasonable errors) but without success.

The fifteen detections are plotted on the new orbital plane of equation 5.2 in figures 5.7 and 5.8. Figure 5.7 shows no considerable change from that of figure 5.1;

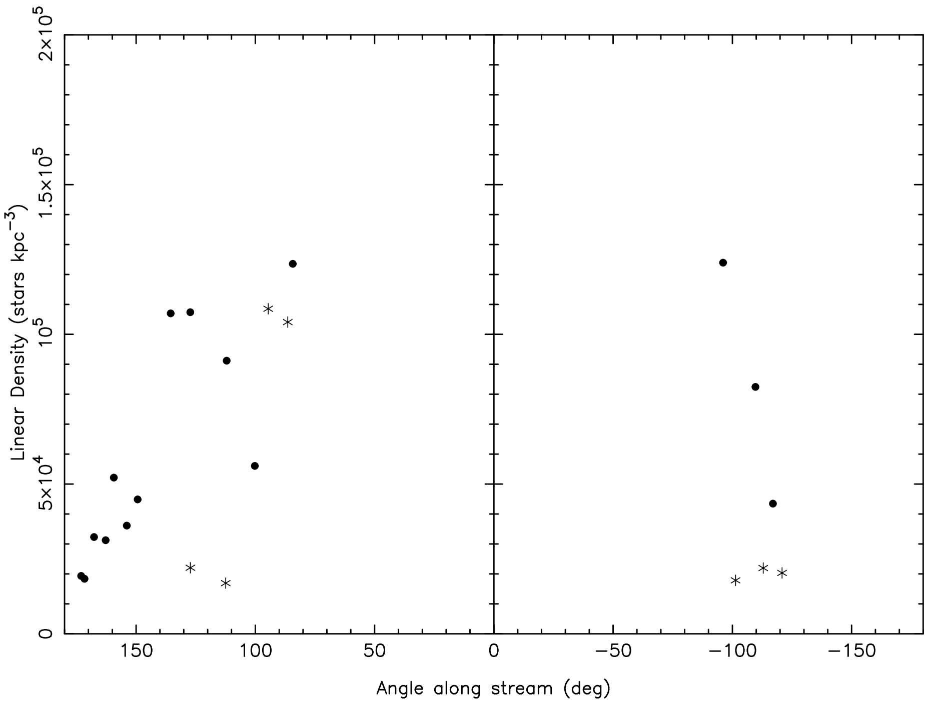

Figure 5.6: The density in each stripe of the Sgr stream has been plotted versus the angle along the stream (solid dots) and the asterisks represents those densities calculated in the model disruption of the Sgr dSph. Here, angle along the stripe denotes the angle from the Sgr dSph core to the stream detection with positive angles representing the leading tail and negative angles representing the trailing tail. Density, here, is a linear density defined as the number of stars within the stream at the detection point after rotating the portion of the stream to be aligned with the plane then normalized by the thickness of the stripe at that point and corrected for edge effects. A prominent trend towards density decreasing as the magnitude of the angle along the stream increases is observed in both the leading and trailing tail. This trend is also observed in the simulation along the leading tail; however, the density appears to remain quite constant along the trailing tail of the simulation.

however, figure 5.8 clearly shows that all the detections of the leading tail lie on a well defined plane, while the Sgr core and the three detections of the trailing tail do not.

The least squares method was again applied to find the best-fit plane to tthe three trailing tail detections and the Sgr dSph core position, resulting in the plane equation

$$0.024X + 03990Y + 0.136Z - 1.801 = 0, \tag{5.4}$$

with correlation value 0.992. These points have been plotted along this plane edge on in figure 5.9. Clearly the trailing tail detections and Sgr core are well described by this plane. The two planes of equations 5.2 and 5.4 are approximately 17° different in orientation. The leading and trailing tail appear to lie along differing orbital planes with the Sgr core lying in the orbital plane of the trailing tail. This may imply a strong precession in the orbital plane of the Sgr dSph which in turn would imply a non-spherical Galactic potential.

The results of the maximum likelihood optimizations and tidal debris extractions provide a set of very accurate determinations to use in construction of a better disruption model. Not only are summary statistics available for use in determining the correctness of a simulation, but a catalog of stars fitting the density profile of the tidal stream has been generated. This provides a brand new means in which the validity of the simulations may be tested, and will serve the constrain the models for the Galaxy.

5.3 The Stellar Spheroid

The results for the stellar spheroid are very interesting. They do not yet give a definitive answer as to the structure of the spheroid because the results returned from the maximum likelihood algorithm are so greatly varied. These results can be seen in table 5.1. The values for the flattening parameter q have a range of $0.314 < q < 0.633$, so the stellar spheroid is clearly oblate; the exact value of the q parameter remains ill-defined. However, with one exception, the analysis of all the contiguous stripes show much greater correspondence than when the three southern stripes are included. The average of q over all stripes is $q = 0.588$. This is consistent

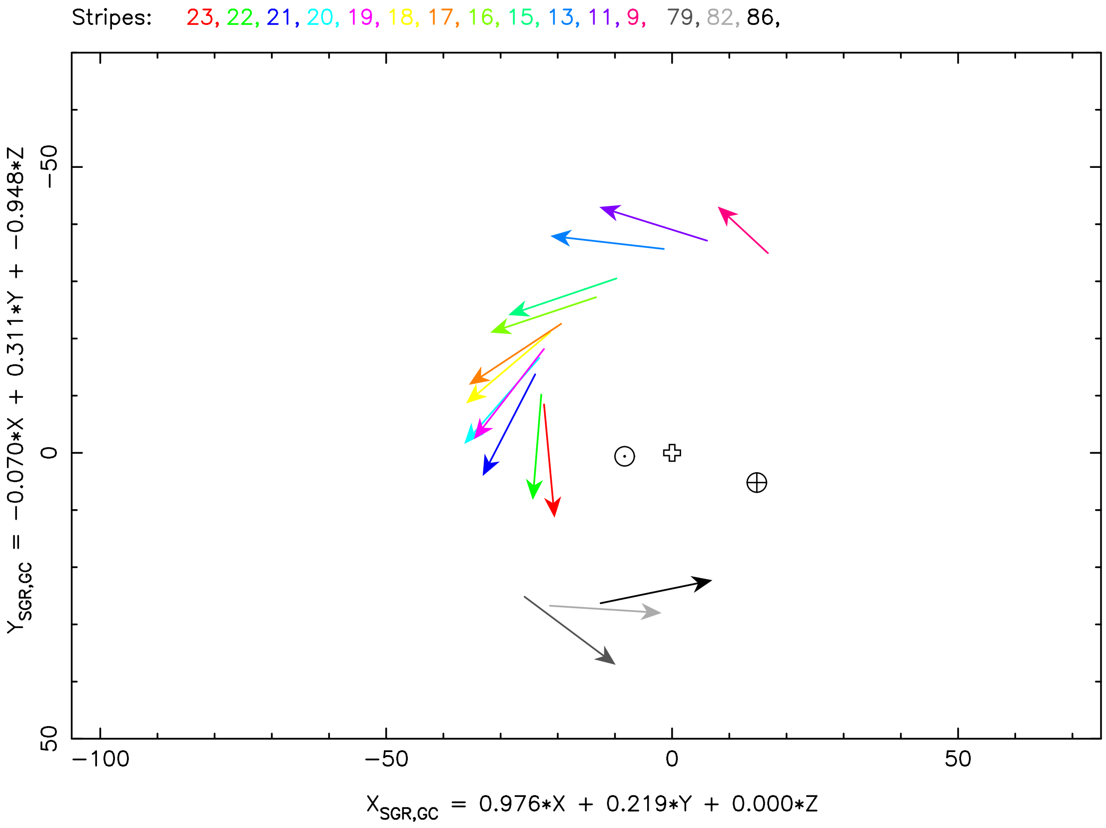

Figure 5.7: Plotted here are the fifteen maximum likelihood detections of the Sgr tidal stream on the orbital plane in equation 5.2 viewed face on. The Galactic center, Solar position, and Sgr dSph position are plotted along with the detected and spatial directions calculated via the maximum likelihood method. Very little has changed in appearance as compared to figure5.1.

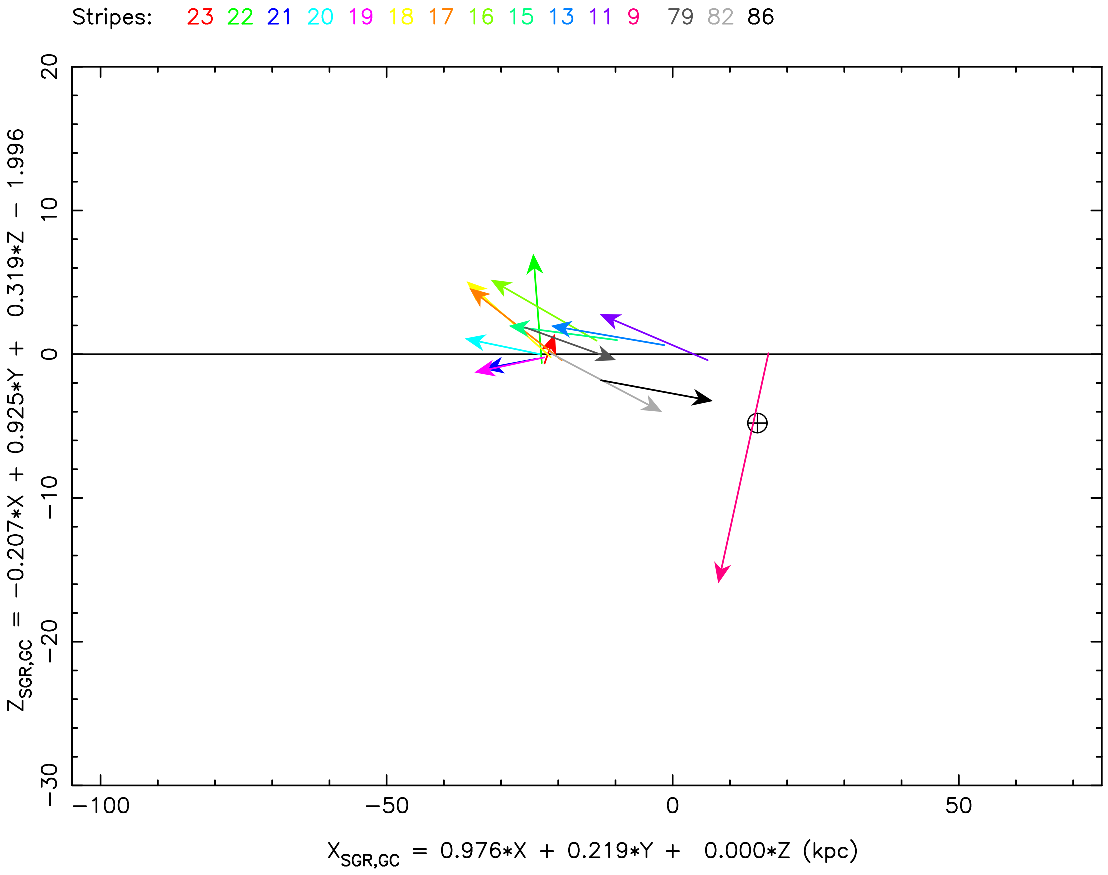

Figure 5.8: Plotted here are the fifteen maximum likelihood detections of the Sgr tidal stream on the orbital plane in equation5.2 viewed edge on. The Sgr dSph position are plotted along with the detected and spatial directions calculated via the maximum likelihood method. Clearly the detections of the leading tail lie along the calculated orbital plane while the trailing tail detections and the Sgr dSph do not.

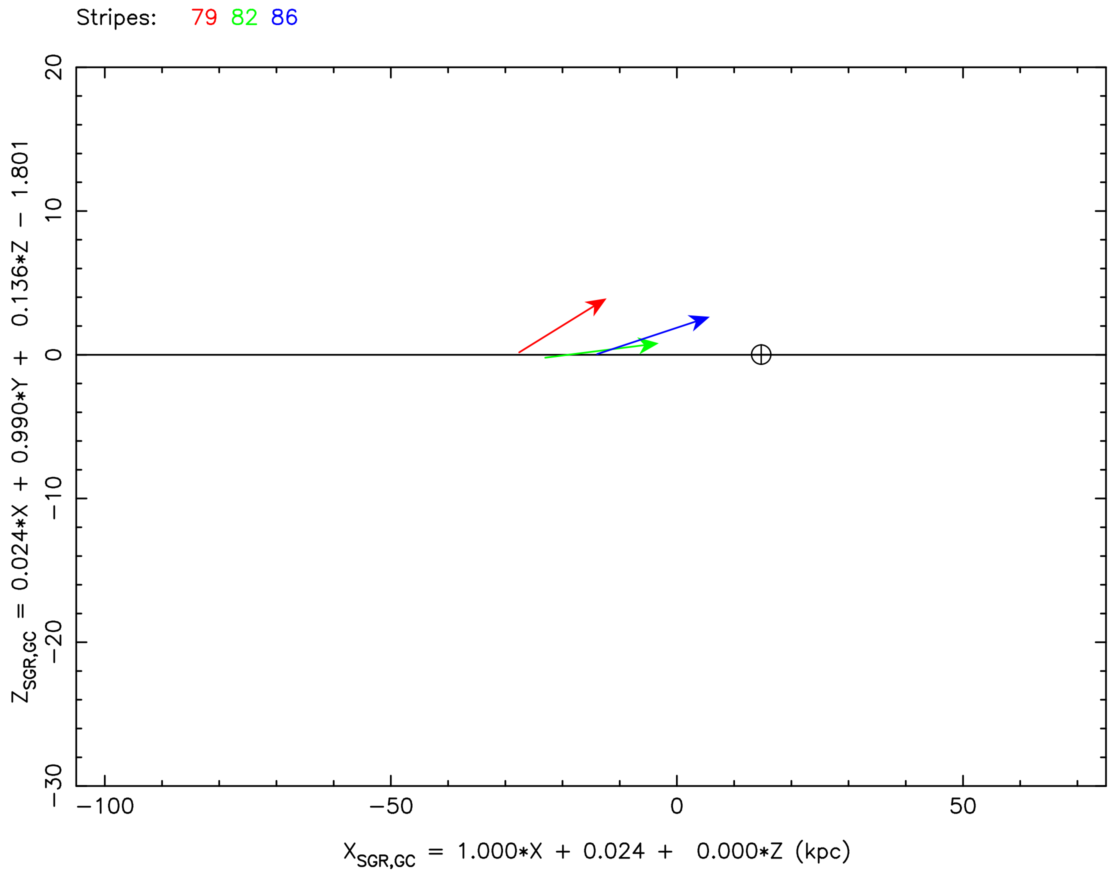

Figure 5.9: Plotted here are the three maximum likelihood detections of the trailing Sgr tidal stream on the orbital plane in equation5.4 viewed edge on. The Sgr dSph position are plotted along with the detected and spatial directions calculated via the maximum likelihood method. Clearly the detections of the trailing tail lie along the calculated orbital plane along with the Sgr dSph. Comparing this figure with figure 5.8 suggests that the leading and trailing tails lie along different orbital planes.

with the range of values fit in [92] ($0.5 < q < 0.8$), though the values found here seem tend to be more oblate, this could be explained in the slight differences in models used to model the spheroid.

The core radius, r_0, varies even more greatly than that of the flattening parameter, q. The values for r_0 were found in the range $1.844 < r_0 < 25.952$. As with q, the values found among the contiguous datasets of the North Galactic cap were found to maintain a more consistent value than those of the three southern stripes. It should also be noted that those values found in the southern stripes are almost a factor of two larger than those found in the northern stripes. The average over all stripes gives $r_0 = 9.187$ kpc.

There are a couple of reasons why the spheroid results are not definitive. It is highly likely that there is more substructure in the spheroid than was fit via the maximum likelihood algorithm in this work. Remnants of past mergers may exist in large enough overdensities to interfere with the maximum likelihood fits but not a high enough overdensity to actively fit. Another possibility is that a global structure such as the spheroid cannot be accurately fit over such a small volume as done in this study. It is possible that optimizing over multiple stripes simultaneously would yield more consistent results.

The single most likely cause for the spheroid results, however, is that the Hernquist model does not accurately represent the smooth component of the stellar spheroid density profile. However, how does one determine the smooth component of a structure without knowing where the non-smooth components are? Until now, it has been an arduous task to attempt to extract uncontaminated samples from the data that represent the smooth spheroid. Yet, the results are still ill-defined as in [92]. This is where the maximum likelihood technique presented here can greatly aid in the spheroid studies, by enabling the removal of all the substructure from the spheroid leaving only the smooth component behind.

As shown in section 3.3, tidal debris can be accurately fit despite an incorrect spheroid model. Therefore, it is possible to run the maximum likelihood algorithm on the data to fit tidal debris, and then extract that tidal debris from the data as shown numerous times here. Once, the tidal debris has been removed, all that

Table 5.1: Spheroid results by stripe.

Stripe	q	r_0 (kpc)
86	0.633 ± 0.010	16.657 ± 0.370
82	0.458 ± 0.024	19.404 ± 0.588
79	0.342 ± 0.005	25.952 ± 0.671
23	0.552 ± 0.009	11.938 ± 0.471
22	0.314 ± 0.019	2.879 ± 0.860
21	0.534 ± 0.015	6.514 ± 0.668
20	0.541 ± 0.009	10.218 ± 0.315
19	0.524 ± 0.013	5.951 ± 0.363
18	0.572 ± 0.009	7.367 ± 00.310
17	0.591 ± 0.010	5.461 ± 0.294
16	0.545 ± 0.010	5.489 ± 0.353
15	0.537 ± 0.013	6.942 ± 0.576
13	0.526 ± 0.012	6.985 ± 0.511
11	0.566 ± 0.053	4.206 ± 1.966
9	0.547 ± 0.017	1.844 ± 0.307

should remain the smooth component of the spheroid. This smooth spheroid data can then, in principle, be fit to great accuracy, and the correct stellar spheroid structure determined.

5.4 Overview

The maximum likelihood method for fitting tidal debris has proven to be an extremely effective means at analyzing spatial star data. In this manner, fifteen distinct SDSS stripes of F turnoff star data have been successfully analyzed with regard to the Sgr tidal stream. A Galactic coordinates density plot can be seen in figure 5.4 The results of the maximum likelihood optimizations have provided positional, orientation, and size information regarding the tidal debris while simultaneously determining the flattening and core radius of the stellar spheroid. Through the use of a probabilistic separation technique, the tidal debris can then be extracted from the data set for separate analysis of the tidal debris and the stellar spheroid. After removing the tidal debris, the remaining spheroid stars it is then possible to study the structure of the smooth component of the spheroid itself. The remaining stars after extracting the Sgr tidal stream can be seen in figure 5.10.

The extracted tidal debris star catalog, seen in figure 5.11, has many uses. This catalog can then be used for comparison with simulations. By creating a catalog of stars that accurately represent the debris characteristics, these simulations will be able to be better constrained, thereby producing the most accurate representations of how the Galaxy attained its current state. Specifically, by constraining the Galactic potential used in these simulations it will be possible to determine the distribution of mass in the Milky Way, and since the primary mass component of the Milky Way is dark matter it will thus be possible to determine the distribution of dark matter in the Galaxy.

Though it does not contain stars that are explicitly stream stars, the catalog as a whole represents the spatial characteristics of the stream at that point in the sky, the tidal debris star catalog could potentially be used in follow-up studies. This is not to say a survey should target all stars in a the star catalog, but the probability that a star is as stream star could potentially be used to maximize the

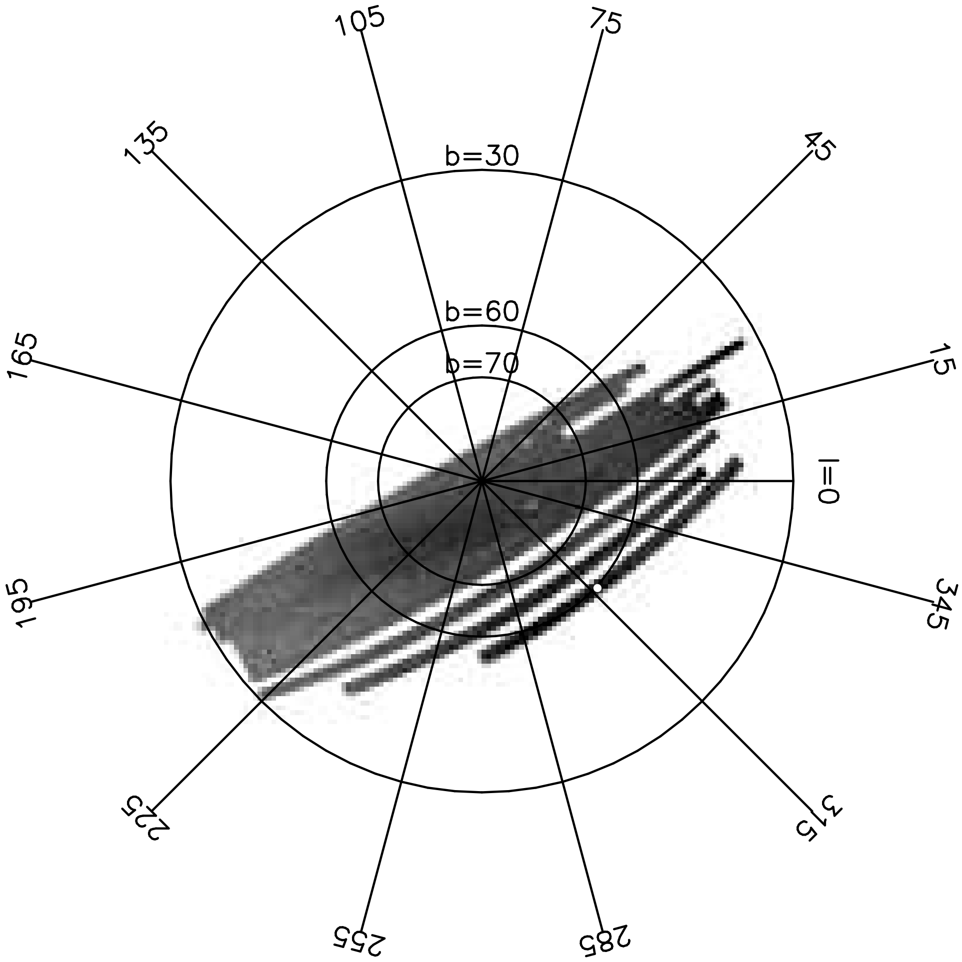

Figure 5.10: Density polar plot in Galactic coordinates are those stars in the Northern Galactic cap remaining after removing those stars found to fit the density profile of the Sgr tidal stream via the separation algorithm. The main Sgr tidal stream has been clearly removed while the bifurcated section of the stream remains.

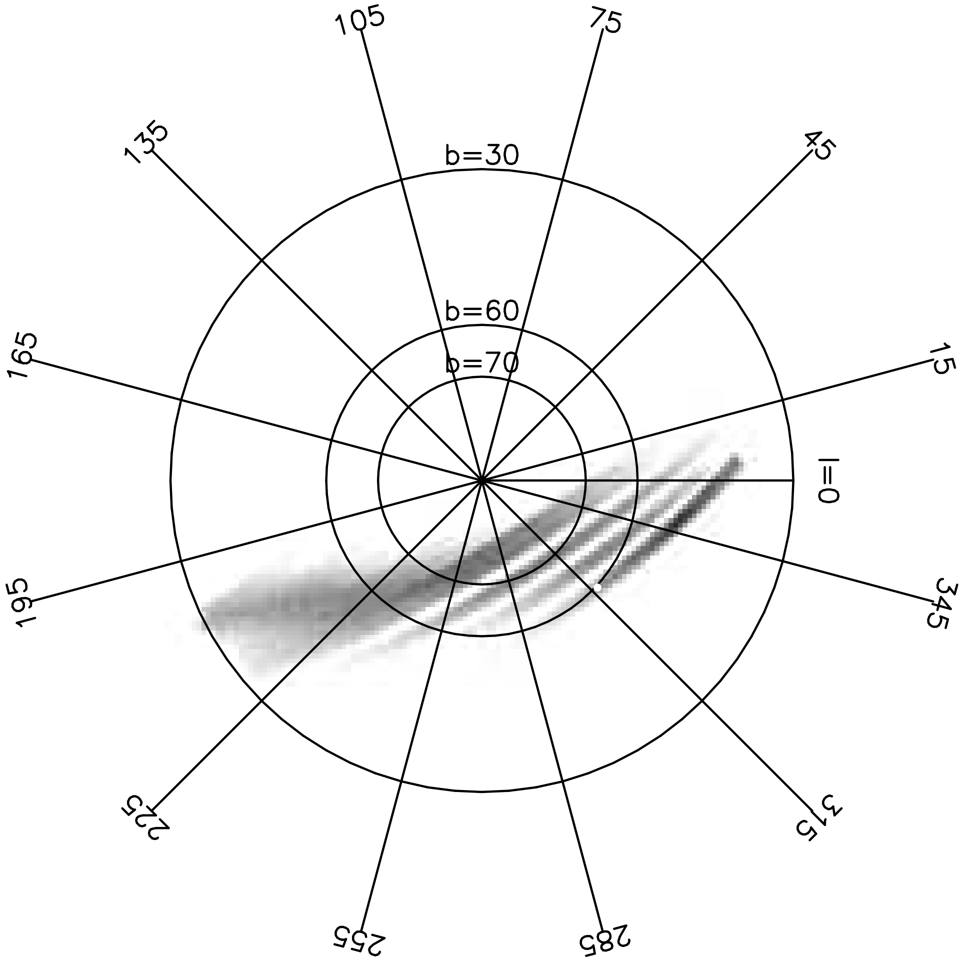

Figure 5.11: Density polar plot in Galactic coordinates are those stars in the Northern Galactic cap found to fit the density profile of the Sgr tidal stream via the separation algorithm.

chance of actually targeting a stream star. By specifically targeting tidal debris stars, it may then be possible to perform studies regarding the stellar properties and characteristics of stars from the disrupted body. This could then provide insight into the disrupted body itself, which would be especially useful should the body be completely disrupted.

5.5 Future Work

There are a number of endeavors that will be pursued both using and regarding the maximum likelihood algorithm. The primary endeavor will be to analyze the SDSS data with regards to other substructure. For instance, fitting the bifurcated section of the Sgr stream along with the Virgo stellar stream would reduce the amount of substructure and would provide not only interesting results regarding these structures themselves, but after extracting these structures from the spheroid, a large sample of reasonably smooth spheroid data should be available for study in order to determine the true density profile of the stellar spheroid.

It will also be useful to extend the ability of the algorithm to fit not only multiple streams simultaneously, but multiple stripes simultaneously. This ability would, in theory, provide a much better fit to the global spheroid population and if the substructure has already been previously removed the structure of the spheroid can be constrained. It may also prove useful to have the ability to maintain continuity between stream segments along adjacent stripes being fit simultaneously. This would mean that the stream axis must meet at the edges of the stripe to maintain a piecewise curve. With this addition to the algorithm it may be possible to provide even more accurate results as the streams would be somewhat more constrained. The addition of multiple star types would be useful as well, in that it would provide more data as well as probing different populations. For example, the addition to use BHB stars would provide the ability to study much more different structures not possible through the use of F turnoff stars.

LITERATURE CITED

[1] P. Whitfield. *Astrology: A History.* British Library, 2004.

[2] Edwin Hubble. A relation between distance and radial velocity among extragalactic nebulae. In *PNAS*, volume 15 (3), pages 168–173, 1929.

[3] T. Matsumoto, S. Hayakawa, H. Koizumi, H. Murakami, K. Uyama, T. Yamagami, and J. A. Thomas. Balloon observation of the central bulge of our Galaxy in near infrared radiation. In G. R. Riegler and R. D. Blandford, editors, *The Galactic Center*, volume 83 of *American Institute of Physics Conference Series*, pages 48–52, 1982.

[4] Y. M. Georgelin and Y. P. Georgelin. The spiral structure of our Galaxy determined from H II regions. *A&A*, 49:57–79, May 1976.

[5] M. J. Reid, K. M. Menten, X. W. Zheng, A. Brunthaler, L. Moscadelli, Y. Xu, B. Zhang, M. Sato, M. Honma, T. Hirota, K. Hachisuka, Y. K. Choi, G. A. Moellenbrock, and A. Bartkiewicz. Trigonometric Parallaxes of Massive Star Forming Regions: VI. Galactic Structure, Fundamental Parameters and Non-Circular Motions. *ArXiv e-prints*, Feb 2009.

[6] K. A. Janes and R. L. Phelps. The galactic system of old star clusters: The development of the galactic disk. *AJ*, 108:1773–1785, Nov 1994.

[7] O. J. Eggen, D. Lynden-Bell, and A. R. Sandage. Evidence from the motions of old stars that the Galaxy collapsed. *ApJ*, 136:748–+, nov 1962.

[8] L. Searle and R. Zinn. Compositions of halo clusters and the formation of the galactic halo. *ApJ*, 225:357–379, oct 1978.

[9] K. C. Freeman. The Galactic spheroid and old disk. *ARA*, 25:603–632, 1987.

[10] K. Freeman and J. Bland-Hawthorn. The New Galaxy: Signatures of Its Formation. *ARA*, 40:487–537, 2002.

[11] The SDSS-II SEGUE Collaboration: Brian Yanny, C. Rockosi, H. J. Newberg, and G. R. Knapp. SEGUE: A Spectroscopic Survey of 240,000 stars with g=14-20. *ArXiv e-prints*, Feb 2009.

[12] J. A. Frieman, B. Bassett, A. Becker, C. Choi, D. Cinabro, F. DeJongh, D. L. Depoy, B. Dilday, M. Doi, P. M. Garnavich, C. J. Hogan, J. Holtzman, M. Im, S. Jha, R. Kessler, K. Konishi, H. Lampeitl, J. Marriner, J. L. Marshall, D. McGinnis, G. Miknaitis, R. C. Nichol, J. L. Prieto, A. G. Riess, M. W. Richmond, R. Romani, M. Sako, D. P. Schneider, M. Smith, N. Takanashi, K. Tokita, K. van der Heyden, N. Yasuda, C. Zheng, J. Adelman-McCarthy,

J. Annis, R. J. Assef, J. Barentine, R. Bender, R. D. Blandford, W. N. Boroski, M. Bremer, H. Brewington, C. A. Collins, A. Crotts, J. Dembicky, J. Eastman, A. Edge, E. Edmondson, E. Elson, M. E. Eyler, A. V. Filippenko, R. J. Foley, S. Frank, A. Goobar, T. Gueth, J. E. Gunn, M. Harvanek, U. Hopp, Y. Ihara, Ž. Ivezić, S. Kahn, J. Kaplan, S. Kent, W. Ketzeback, S. J. Kleinman, W. Kollatschny, R. G. Kron, J. Krzesiński, D. Lamenti, G. Leloudas, H. Lin, D. C. Long, J. Lucey, R. H. Lupton, E. Malanushenko, V. Malanushenko, R. J. McMillan, J. Mendez, C. W. Morgan, T. Morokuma, A. Nitta, L. Ostman, K. Pan, C. M. Rockosi, A. K. Romer, P. Ruiz-Lapuente, G. Saurage, K. Schlesinger, S. A. Snedden, J. Sollerman, C. Stoughton, M. Stritzinger, M. Subba Rao, D. Tucker, P. Vaisanen, L. C. Watson, S. Watters, J. C. Wheeler, B. Yanny, and D. York. The Sloan Digital Sky Survey-II Supernova Survey: Technical Summary. *AJ*, 135:338–347, Jan 2008.

[13] M. Sako, B. Bassett, A. Becker, D. Cinabro, F. DeJongh, D. L. Depoy, B. Dilday, M. Doi, J. A. Frieman, P. M. Garnavich, C. J. Hogan, J. Holtzman, S. Jha, R. Kessler, K. Konishi, H. Lampeitl, J. Marriner, G. Miknaitis, R. C. Nichol, J. L. Prieto, A. G. Riess, M. W. Richmond, R. Romani, D. P. Schneider, M. Smith, M. Subba Rao, N. Takanashi, K. Tokita, K. van der Heyden, N. Yasuda, C. Zheng, J. Barentine, H. Brewington, C. Choi, J. Dembicky, M. Harnavek, Y. Ihara, M. Im, W. Ketzeback, S. J. Kleinman, J. Krzesiński, D. C. Long, E. Malanushenko, V. Malanushenko, R. J. McMillan, T. Morokuma, A. Nitta, K. Pan, G. Saurage, and S. A. Snedden. The Sloan Digital Sky Survey-II Supernova Survey: Search Algorithm and Follow-Up Observations. *AJ*, 135:348–373, jan 2008.

[14] D. G. York, J. Adelman, J. E. Anderson, Jr., S. F. Anderson, J. Annis, N. A. Bahcall, J. A. Bakken, R. Barkhouser, S. Bastian, E. Berman, W. N. Boroski, S. Bracker, C. Briegel, J. W. Briggs, J. Brinkmann, R. Brunner, S. Burles, L. Carey, M. A. Carr, F. J. Castander, B. Chen, P. L. Colestock, A. J. Connolly, J. H. Crocker, I. Csabai, P. C. Czarapata, J. E. Davis, M. Doi, T. Dombeck, D. Eisenstein, N. Ellman, B. R. Elms, M. L. Evans, X. Fan, G. R. Federwitz, L. Fiscelli, S. Friedman, J. A. Frieman, M. Fukugita, B. Gillespie, J. E. Gunn, V. K. Gurbani, E. de Haas, M. Haldeman, F. H. Harris, J. Hayes, T. M. Heckman, G. S. Hennessy, R. B. Hindsley, S. Holm, D. J. Holmgren, C.-h. Huang, C. Hull, D. Husby, S.-I. Ichikawa, T. Ichikawa, Ž. Ivezić, S. Kent, R. S. J. Kim, E. Kinney, M. Klaene, A. N. Kleinman, S. Kleinman, G. R. Knapp, J. Korienek, R. G. Kron, P. Z. Kunszt, D. Q. Lamb, B. Lee, R. F. Leger, S. Limmongkol, C. Lindenmeyer, D. C. Long, C. Loomis, J. Loveday, R. Lucinio, R. H. Lupton, B. MacKinnon, E. J. Mannery, P. M. Mantsch, B. Margon, P. McGehee, T. A. McKay, A. Meiksin, A. Merelli, D. G. Monet, J. A. Munn, V. K. Narayanan, T. Nash, E. Neilsen, R. Neswold, H. J. Newberg, R. C. Nichol, T. Nicinski, M. Nonino, N. Okada, S. Okamura, J. P. Ostriker, R. Owen, A. G. Pauls, J. Peoples, R. L. Peterson, D. Petravick, J. R. Pier, A. Pope, R. Pordes,

A. Prosapio, R. Rechenmacher, T. R. Quinn, G. T. Richards, M. W. Richmond, C. H. Rivetta, C. M. Rockosi, K. Ruthmansdorfer, D. Sandford, D. J. Schlegel, D. P. Schneider, M. Sekiguchi, G. Sergey, K. Shimasaku, W. A. Siegmund, S. Smee, J. A. Smith, S. Snedden, R. Stone, C. Stoughton, M. A. Strauss, C. Stubbs, M. SubbaRao, A. S. Szalay, I. Szapudi, G. P. Szokoly, A. R. Thakar, C. Tremonti, D. L. Tucker, A. Uomoto, D. Vanden Berk, M. S. Vogeley, P. Waddell, S.-i. Wang, M. Watanabe, D. H. Weinberg, B. Yanny, and N. Yasuda. The Sloan Digital Sky Survey: Technical Summary. *AJ*, 120:1579–1587, sep 2000.

[15] J. E. Gunn, M. Carr, C. Rockosi, M. Sekiguchi, K. Berry, B. Elms, E. de Haas, Ž. Ivezić, G. Knapp, R. Lupton, G. Pauls, R. Simcoe, R. Hirsch, D. Sanford, S. Wang, D. York, F. Harris, J. Annis, L. Bartozek, W. Boroski, J. Bakken, M. Haldeman, S. Kent, S. Holm, D. Holmgren, D. Petravick, A. Prosapio, R. Rechenmacher, M. Doi, M. Fukugita, K. Shimasaku, N. Okada, C. Hull, W. Siegmund, E. Mannery, M. Blouke, D. Heidtman, D. Schneider, R. Lucinio, and J. Brinkman. The Sloan Digital Sky Survey Photometric Camera. *AJ*, 116:3040–3081, dec 1998.

[16] E.F. Lally. Mosaic Guidance For Interplanetary Travel. In *Space Flight Report to the Nation*, American Rocket Society, pages 2249–2261, Oct 1961.

[17] W.S. Boyle and G.E. Smith. Charge Coupled Semiconductor Devices. *Bell Systems Technical Journal*, 49:587–593, 1970.

[18] M. Fukugita, T. Ichikawa, J. E. Gunn, M. Doi, K. Shimasaku, and D. P. Schneider. The Sloan Digital Sky Survey Photometric System. *AJ*, 111:1748–+, apr 1996.

[19] J. A. Smith, D. L. Tucker, S. Kent, M. W. Richmond, M. Fukugita, T. Ichikawa, S.-i. Ichikawa, A. M. Jorgensen, A. Uomoto, J. E. Gunn, M. Hamabe, M. Watanabe, A. Tolea, A. Henden, J. Annis, J. R. Pier, T. A. McKay, J. Brinkmann, B. Chen, J. Holtzman, K. Shimasaku, and D. G. York. The u'g'r'i'z' Standard-Star System. *AJ*, 123:2121–2144, apr 2002.

[20] C. Stoughton, R. H. Lupton, M. Bernardi, M. R. Blanton, S. Burles, F. J. Castander, A. J. Connolly, D. J. Eisenstein, J. A. Frieman, G. S. Hennessy, R. B. Hindsley, Ž. Ivezić, S. Kent, P. Z. Kunszt, B. C. Lee, A. Meiksin, J. A. Munn, H. J. Newberg, R. C. Nichol, T. Nicinski, J. R. Pier, G. T. Richards, M. W. Richmond, D. J. Schlegel, J. A. Smith, M. A. Strauss, M. SubbaRao, A. S. Szalay, A. R. Thakar, D. L. Tucker, D. E. Vanden Berk, B. Yanny, J. K. Adelman, J. E. Anderson, Jr., S. F. Anderson, J. Annis, N. A. Bahcall, J. A. Bakken, M. Bartelmann, S. Bastian, A. Bauer, E. Berman, H. Böhringer, W. N. Boroski, S. Bracker, C. Briegel, J. W. Briggs, J. Brinkmann, R. Brunner, L. Carey, M. A. Carr, B. Chen, D. Christian, P. L. Colestock, J. H. Crocker, I. Csabai, P. C. Czarapata, J. Dalcanton, A. F. Davidsen, J. E. Davis, W. Dehnen, S. Dodelson, M. Doi, T. Dombeck, M. Donahue, N. Ellman, B. R. Elms, M. L.

Evans, L. Eyer, X. Fan, G. R. Federwitz, S. Friedman, M. Fukugita, R. Gal, B. Gillespie, K. Glazebrook, J. Gray, E. K. Grebel, B. Greenawalt, G. Greene, J. E. Gunn, E. de Haas, Z. Haiman, M. Haldeman, P. B. Hall, M. Hamabe, B. Hansen, F. H. Harris, H. Harris, M. Harvanek, S. L. Hawley, J. J. E. Hayes, T. M. Heckman, A. Helmi, A. Henden, C. J. Hogan, D. W. Hogg, D. J. Holmgren, J. Holtzman, C.-H. Huang, C. Hull, S.-I. Ichikawa, T. Ichikawa, D. E. Johnston, G. Kauffmann, R. S. J. Kim, T. Kimball, E. Kinney, M. Klaene, S. J. Kleinman, A. Klypin, G. R. Knapp, J. Korienek, J. Krolik, R. G. Kron, J. Krzesiński, D. Q. Lamb, R. F. Leger, S. Limmongkol, C. Lindenmeyer, D. C. Long, C. Loomis, J. Loveday, B. MacKinnon, E. J. Mannery, P. M. Mantsch, B. Margon, P. McGehee, T. A. McKay, B. McLean, K. Menou, A. Merelli, H. J. Mo, D. G. Monet, O. Nakamura, V. K. Narayanan, T. Nash, E. H. Neilsen, Jr., P. R. Newman, A. Nitta, M. Odenkirchen, N. Okada, S. Okamura, J. P. Ostriker, R. Owen, A. G. Pauls, J. Peoples, R. S. Peterson, D. Petravick, A. Pope, R. Pordes, M. Postman, A. Prosapio, T. R. Quinn, R. Rechenmacher, C. H. Rivetta, H.-W. Rix, C. M. Rockosi, R. Rosner, K. Ruthmansdorfer, D. Sandford, D. P. Schneider, R. Scranton, M. Sekiguchi, G. Sergey, R. Sheth, K. Shimasaku, S. Smee, S. A. Snedden, A. Stebbins, C. Stubbs, I. Szapudi, P. Szkody, G. P. Szokoly, S. Tabachnik, Z. Tsvetanov, A. Uomoto, M. S. Vogeley, W. Voges, P. Waddell, R. Walterbos, S.-i. Wang, M. Watanabe, D. H. Weinberg, R. L. White, S. D. M. White, B. Wilhite, D. Wolfe, N. Yasuda, D. G. York, I. Zehavi, and W. Zheng. Sloan Digital Sky Survey: Early Data Release. *AJ*, 123:485–548, jan 2002.

[21] J. R. Pier, J. A. Munn, R. B. Hindsley, G. S. Hennessy, S. M. Kent, R. H. Lupton, and Ž. Ivezić. Astrometric Calibration of the Sloan Digital Sky Survey. *AJ*, 125:1559–1579, mar 2003.

[22] D. W. Hogg, D. P. Finkbeiner, D. J. Schlegel, and J. E. Gunn. A Photometricity and Extinction Monitor at the Apache Point Observatory. *AJ*, 122:2129–2138, Oct 2001.

[23] K. Abazajian, J. K. Adelman-McCarthy, M. A. Agüeros, S. S. Allam, S. F. Anderson, J. Annis, N. A. Bahcall, I. K. Baldry, S. Bastian, A. Berlind, M. Bernardi, M. R. Blanton, N. Blythe, J. J. Bochanski, Jr., W. N. Boroski, H. Brewington, J. W. Briggs, J. Brinkmann, R. J. Brunner, T. Budavári, L. N. Carey, M. A. Carr, F. J. Castander, K. Chiu, M. J. Collinge, A. J. Connolly, K. R. Covey, I. Csabai, J. J. Dalcanton, S. Dodelson, M. Doi, F. Dong, D. J. Eisenstein, M. L. Evans, X. Fan, P. D. Feldman, D. P. Finkbeiner, S. D. Friedman, J. A. Frieman, M. Fukugita, R. R. Gal, B. Gillespie, K. Glazebrook, C. F. Gonzalez, J. Gray, E. K. Grebel, L. Grodnicki, J. E. Gunn, V. K. Gurbani, P. B. Hall, L. Hao, D. Harbeck, F. H. Harris, H. C. Harris, M. Harvanek, S. L. Hawley, T. M. Heckman, J. F. Helmboldt, J. S. Hendry, G. S. Hennessy, R. B. Hindsley, D. W. Hogg, D. J. Holmgren, J. A. Holtzman, L. Homer, L. Hui, S.-i. Ichikawa, T. Ichikawa, J. P. Inkmann, Ž. Ivezić, S. Jester, D. E. Johnston, B. Jordan,

W. P. Jordan, A. M. Jorgensen, M. Jurić, G. Kauffmann, S. M. Kent, S. J. Kleinman, G. R. Knapp, A. Y. Kniazev, R. G. Kron, J. Krzesiński, P. Z. Kunszt, N. Kuropatkin, D. Q. Lamb, H. Lampeitl, B. E. Laubscher, B. C. Lee, R. F. Leger, N. Li, A. Lidz, H. Lin, Y.-S. Loh, D. C. Long, J. Loveday, R. H. Lupton, T. Malik, B. Margon, P. M. McGehee, T. A. McKay, A. Meiksin, G. A. Miknaitis, B. K. Moorthy, J. A. Munn, T. Murphy, R. Nakajima, V. K. Narayanan, T. Nash, E. H. Neilsen, Jr., H. J. Newberg, P. R. Newman, R. C. Nichol, T. Nicinski, M. Nieto-Santisteban, A. Nitta, M. Odenkirchen, S. Okamura, J. P. Ostriker, R. Owen, N. Padmanabhan, J. Peoples, J. R. Pier, B. Pindor, A. C. Pope, T. R. Quinn, R. R. Rafikov, S. N. Raymond, G. T. Richards, M. W. Richmond, H.-W. Rix, C. M. Rockosi, J. Schaye, D. J. Schlegel, D. P. Schneider, J. Schroeder, R. Scranton, M. Sekiguchi, U. Seljak, G. Sergey, B. Sesar, E. Sheldon, K. Shimasaku, W. A. Siegmund, N. M. Silvestri, A. J. Sinisgalli, E. Sirko, J. A. Smith, V. Smolčić, S. A. Snedden, A. Stebbins, C. Steinhardt, G. Stinson, C. Stoughton, I. V. Strateva, M. A. Strauss, M. SubbaRao, A. S. Szalay, I. Szapudi, P. Szkody, L. Tasca, M. Tegmark, A. R. Thakar, C. Tremonti, D. L. Tucker, A. Uomoto, D. E. Vanden Berk, J. Vandenberg, M. S. Vogeley, W. Voges, N. P. Vogt, L. M. Walkowicz, D. H. Weinberg, A. A. West, S. D. M. White, B. C. Wilhite, B. Willman, Y. Xu, B. Yanny, J. Yarger, N. Yasuda, C.-W. Yip, D. R. Yocum, D. G. York, N. L. Zakamska, I. Zehavi, W. Zheng, S. Zibetti, and D. B. Zucker. The First Data Release of the Sloan Digital Sky Survey. *AJ*, 126:2081–2086, Oct 2003.

[24] K. Abazajian, J. K. Adelman-McCarthy, M. A. Agüeros, S. S. Allam, K. Anderson, S. F. Anderson, J. Annis, N. A. Bahcall, I. K. Baldry, S. Bastian, A. Berlind, M. Bernardi, M. R. Blanton, J. J. Bochanski, Jr., W. N. Boroski, J. W. Briggs, J. Brinkmann, R. J. Brunner, T. Budavári, L. N. Carey, S. Carliles, F. J. Castander, A. J. Connolly, I. Csabai, M. Doi, F. Dong, D. J. Eisenstein, M. L. Evans, X. Fan, D. P. Finkbeiner, S. D. Friedman, J. A. Frieman, M. Fukugita, R. R. Gal, B. Gillespie, K. Glazebrook, J. Gray, E. K. Grebel, J. E. Gunn, V. K. Gurbani, P. B. Hall, M. Hamabe, F. H. Harris, H. C. Harris, M. Harvanek, T. M. Heckman, J. S. Hendry, G. S. Hennessy, R. B. Hindsley, C. J. Hogan, D. W. Hogg, D. J. Holmgren, S.-i. Ichikawa, T. Ichikawa, Ž. Ivezić, S. Jester, D. E. Johnston, A. M. Jorgensen, S. M. Kent, S. J. Kleinman, G. R. Knapp, A. Y. Kniazev, R. G. Kron, J. Krzesinski, P. Z. Kunszt, N. Kuropatkin, D. Q. Lamb, H. Lampeitl, B. C. Lee, R. F. Leger, N. Li, H. Lin, Y.-S. Loh, D. C. Long, J. Loveday, R. H. Lupton, T. Malik, B. Margon, T. Matsubara, P. M. McGehee, T. A. McKay, A. Meiksin, J. A. Munn, R. Nakajima, T. Nash, E. H. Neilsen, Jr., H. J. Newberg, P. R. Newman, R. C. Nichol, T. Nicinski, M. Nieto-Santisteban, A. Nitta, S. Okamura, W. O'Mullane, J. P. Ostriker, R. Owen, N. Padmanabhan, J. Peoples, J. R. Pier, A. C. Pope, T. R. Quinn, G. T. Richards, M. W. Richmond, H.-W. Rix, C. M. Rockosi, D. J. Schlegel, D. P. Schneider, R. Scranton, M. Sekiguchi, U. Seljak, G. Sergey, B. Sesar, E. Sheldon, K. Shimasaku, W. A. Siegmund, N. M. Silvestri, J. A.

Smith, V. Smolčić, S. A. Snedden, A. Stebbins, C. Stoughton, M. A. Strauss, M. SubbaRao, A. S. Szalay, I. Szapudi, P. Szkody, G. P. Szokoly, M. Tegmark, L. Teodoro, A. R. Thakar, C. Tremonti, D. L. Tucker, A. Uomoto, D. E. Vanden Berk, J. Vandenberg, M. S. Vogeley, W. Voges, N. P. Vogt, L. M. Walkowicz, S.-i. Wang, D. H. Weinberg, A. A. West, S. D. M. White, B. C. Wilhite, Y. Xu, B. Yanny, N. Yasuda, C.-W. Yip, D. R. Yocum, D. G. York, I. Zehavi, S. Zibetti, and D. B. Zucker. The Second Data Release of the Sloan Digital Sky Survey. *AJ*, 128:502–512, Jul 2004.

[25] K. Abazajian, J. K. Adelman-McCarthy, M. A. Agüeros, S. S. Allam, K. S. J. Anderson, S. F. Anderson, J. Annis, N. A. Bahcall, I. K. Baldry, S. Bastian, A. Berlind, M. Bernardi, M. R. Blanton, J. J. Bochanski, Jr., W. N. Boroski, H. J. Brewington, J. W. Briggs, J. Brinkmann, R. J. Brunner, T. Budavári, L. N. Carey, F. J. Castander, A. J. Connolly, K. R. Covey, I. Csabai, J. J. Dalcanton, M. Doi, F. Dong, D. J. Eisenstein, M. L. Evans, X. Fan, D. P. Finkbeiner, S. D. Friedman, J. A. Frieman, M. Fukugita, B. Gillespie, K. Glazebrook, J. Gray, E. K. Grebel, J. E. Gunn, V. K. Gurbani, P. B. Hall, M. Hamabe, D. Harbeck, F. H. Harris, H. C. Harris, M. Harvanek, S. L. Hawley, J. Hayes, T. M. Heckman, J. S. Hendry, G. S. Hennessy, R. B. Hindsley, C. J. Hogan, D. W. Hogg, D. J. Holmgren, J. A. Holtzman, S.-i. Ichikawa, T. Ichikawa, Ž. Ivezić, S. Jester, D. E. Johnston, A. M. Jorgensen, M. Jurić, S. M. Kent, S. J. Kleinman, G. R. Knapp, A. Y. Kniazev, R. G. Kron, J. Krzesinski, D. Q. Lamb, H. Lampeitl, B. C. Lee, H. Lin, D. C. Long, J. Loveday, R. H. Lupton, E. Mannery, B. Margon, D. Martínez-Delgado, T. Matsubara, P. M. McGehee, T. A. McKay, A. Meiksin, B. Ménard, J. A. Munn, T. Nash, E. H. Neilsen, Jr., H. J. Newberg, P. R. Newman, R. C. Nichol, T. Nicinski, M. Nieto-Santisteban, A. Nitta, S. Okamura, W. O'Mullane, R. Owen, N. Padmanabhan, G. Pauls, J. Peoples, J. R. Pier, A. C. Pope, D. Pourbaix, T. R. Quinn, M. J. Raddick, G. T. Richards, M. W. Richmond, H.-W. Rix, C. M. Rockosi, D. J. Schlegel, D. P. Schneider, J. Schroeder, R. Scranton, M. Sekiguchi, E. Sheldon, K. Shimasaku, N. M. Silvestri, J. A. Smith, V. Smolčić, S. A. Snedden, A. Stebbins, C. Stoughton, M. A. Strauss, M. SubbaRao, A. S. Szalay, I. Szapudi, P. Szkody, G. P. Szokoly, M. Tegmark, L. Teodoro, A. R. Thakar, C. Tremonti, D. L. Tucker, A. Uomoto, D. E. Vanden Berk, J. Vandenberg, M. S. Vogeley, W. Voges, N. P. Vogt, L. M. Walkowicz, S.-i. Wang, D. H. Weinberg, A. A. West, S. D. M. White, B. C. Wilhite, Y. Xu, B. Yanny, N. Yasuda, C.-W. Yip, D. R. Yocum, D. G. York, I. Zehavi, S. Zibetti, and D. B. Zucker. The Third Data Release of the Sloan Digital Sky Survey. *AJ*, 129:1755–1759, Mar 2005.

[26] J. K. Adelman-McCarthy, M. A. Agüeros, S. S. Allam, K. S. J. Anderson, S. F. Anderson, J. Annis, N. A. Bahcall, I. K. Baldry, J. C. Barentine, A. Berlind, M. Bernardi, M. R. Blanton, W. N. Boroski, H. J. Brewington, J. Brinchmann, J. Brinkmann, R. J. Brunner, T. Budavári, L. N. Carey, M. A. Carr, F. J.

Castander, A. J. Connolly, I. Csabai, P. C. Czarapata, J. J. Dalcanton, M. Doi, F. Dong, D. J. Eisenstein, M. L. Evans, X. Fan, D. P. Finkbeiner, S. D. Friedman, J. A. Frieman, M. Fukugita, B. Gillespie, K. Glazebrook, J. Gray, E. K. Grebel, J. E. Gunn, V. K. Gurbani, E. de Haas, P. B. Hall, F. H. Harris, M. Harvanek, S. L. Hawley, J. Hayes, J. S. Hendry, G. S. Hennessy, R. B. Hindsley, C. M. Hirata, C. J. Hogan, D. W. Hogg, D. J. Holmgren, J. A. Holtzman, S.-i. Ichikawa, Ž. Ivezić, S. Jester, D. E. Johnston, A. M. Jorgensen, M. Jurić, S. M. Kent, S. J. Kleinman, G. R. Knapp, A. Y. Kniazev, R. G. Kron, J. Krzesinski, N. Kuropatkin, D. Q. Lamb, H. Lampeitl, B. C. Lee, R. F. Leger, H. Lin, D. C. Long, J. Loveday, R. H. Lupton, B. Margon, D. Martínez-Delgado, R. Mandelbaum, T. Matsubara, P. M. McGehee, T. A. McKay, A. Meiksin, J. A. Munn, R. Nakajima, T. Nash, E. H. Neilsen, Jr., H. J. Newberg, P. R. Newman, R. C. Nichol, T. Nicinski, M. Nieto-Santisteban, A. Nitta, W. O'Mullane, S. Okamura, R. Owen, N. Padmanabhan, G. Pauls, J. J. Peoples, J. R. Pier, A. C. Pope, D. Pourbaix, T. R. Quinn, G. T. Richards, M. W. Richmond, C. M. Rockosi, D. J. Schlegel, D. P. Schneider, J. Schroeder, R. Scranton, U. Seljak, E. Sheldon, K. Shimasaku, J. A. Smith, V. Smolčić, S. A. Snedden, C. Stoughton, M. A. Strauss, M. SubbaRao, A. S. Szalay, I. Szapudi, P. Szkody, M. Tegmark, A. R. Thakar, D. L. Tucker, A. Uomoto, D. E. Vanden Berk, J. Vandenberg, M. S. Vogeley, W. Voges, N. P. Vogt, L. M. Walkowicz, D. H. Weinberg, A. A. West, S. D. M. White, Y. Xu, B. Yanny, D. R. Yocum, D. G. York, I. Zehavi, S. Zibetti, and D. B. Zucker. The Fourth Data Release of the Sloan Digital Sky Survey. *ApJS*, 162:38–48, jan 2006.

[27] J. K. Adelman-McCarthy, M. A. Agüeros, S. S. Allam, K. S. J. Anderson, S. F. Anderson, J. Annis, N. A. Bahcall, C. A. L. Bailer-Jones, I. K. Baldry, J. C. Barentine, T. C. Beers, V. Belokurov, A. Berlind, M. Bernardi, M. R. Blanton, J. J. Bochanski, W. N. Boroski, D. M. Bramich, H. J. Brewington, J. Brinchmann, J. Brinkmann, R. J. Brunner, T. Budavári, L. N. Carey, S. Carliles, M. A. Carr, F. J. Castander, A. J. Connolly, R. J. Cool, C. E. Cunha, I. Csabai, J. J. Dalcanton, M. Doi, D. J. Eisenstein, M. L. Evans, N. W. Evans, X. Fan, D. P. Finkbeiner, S. D. Friedman, J. A. Frieman, M. Fukugita, B. Gillespie, G. Gilmore, K. Glazebrook, J. Gray, E. K. Grebel, J. E. Gunn, E. de Haas, P. B. Hall, M. Harvanek, S. L. Hawley, J. Hayes, T. M. Heckman, J. S. Hendry, G. S. Hennessy, R. B. Hindsley, C. M. Hirata, C. J. Hogan, D. W. Hogg, J. A. Holtzman, S.-i. Ichikawa, T. Ichikawa, Ž. Ivezić, S. Jester, D. E. Johnston, A. M. Jorgensen, M. Jurić, G. Kauffmann, S. M. Kent, S. J. Kleinman, G. R. Knapp, A. Y. Kniazev, R. G. Kron, J. Krzesinski, N. Kuropatkin, D. Q. Lamb, H. Lampeitl, B. C. Lee, R. F. Leger, M. Lima, H. Lin, D. C. Long, J. Loveday, R. H. Lupton, R. Mandelbaum, B. Margon, D. Martínez-Delgado, T. Matsubara, P. M. McGehee, T. A. McKay, A. Meiksin, J. A. Munn, R. Nakajima, T. Nash, E. H. Neilsen, Jr., H. J. Newberg, R. C. Nichol, M. Nieto-Santisteban, A. Nitta, H. Oyaizu, S. Okamura, J. P. Ostriker, N. Padmanabhan, C. Park, J. J. Peoples, J. R. Pier, A. C. Pope, D. Pourbaix, T. R. Quinn, M. J. Raddick,

P. Re Fiorentin, G. T. Richards, M. W. Richmond, H.-W. Rix, C. M. Rockosi, D. J. Schlegel, D. P. Schneider, R. Scranton, U. Seljak, E. Sheldon, K. Shimasaku, N. M. Silvestri, J. A. Smith, V. Smolčić, S. A. Snedden, A. Stebbins, C. Stoughton, M. A. Strauss, M. SubbaRao, Y. Suto, A. S. Szalay, I. Szapudi, P. Szkody, M. Tegmark, A. R. Thakar, C. A. Tremonti, D. L. Tucker, A. Uomoto, D. E. Vanden Berk, J. Vandenberg, S. Vidrih, M. S. Vogeley, W. Voges, N. P. Vogt, D. H. Weinberg, A. A. West, S. D. M. White, B. Wilhite, B. Yanny, D. R. Yocum, D. G. York, I. Zehavi, S. Zibetti, and D. B. Zucker. The Fifth Data Release of the Sloan Digital Sky Survey. *ApJS*, 172:634–644, Oct 2007.

[28] J. K. Adelman-McCarthy, M. A. Agüeros, S. S. Allam, C. Allende Prieto, K. S. J. Anderson, S. F. Anderson, J. Annis, N. A. Bahcall, C. A. L. Bailer-Jones, I. K. Baldry, J. C. Barentine, B. A. Bassett, A. C. Becker, T. C. Beers, E. F. Bell, A. A. Berlind, M. Bernardi, M. R. Blanton, J. J. Bochanski, W. N. Boroski, J. Brinchmann, J. Brinkmann, R. J. Brunner, T. Budavári, S. Carliles, M. A. Carr, F. J. Castander, D. Cinabro, R. J. Cool, K. R. Covey, I. Csabai, C. E. Cunha, J. R. A. Davenport, B. Dilday, M. Doi, D. J. Eisenstein, M. L. Evans, X. Fan, D. P. Finkbeiner, S. D. Friedman, J. A. Frieman, M. Fukugita, B. T. Gänsicke, E. Gates, B. Gillespie, K. Glazebrook, J. Gray, E. K. Grebel, J. E. Gunn, V. K. Gurbani, P. B. Hall, P. Harding, M. Harvanek, S. L. Hawley, J. Hayes, T. M. Heckman, J. S. Hendry, R. B. Hindsley, C. M. Hirata, C. J. Hogan, D. W. Hogg, J. B. Hyde, S.-i. Ichikawa, Ž. Ivezić, S. Jester, J. A. Johnson, A. M. Jorgensen, M. Jurić, S. M. Kent, R. Kessler, S. J. Kleinman, G. R. Knapp, R. G. Kron, J. Krzesinski, N. Kuropatkin, D. Q. Lamb, H. Lampeitl, S. Lebedeva, Y. S. Lee, R. F. Leger, S. Lépine, M. Lima, H. Lin, D. C. Long, C. P. Loomis, J. Loveday, R. H. Lupton, O. Malanushenko, V. Malanushenko, R. Mandelbaum, B. Margon, J. P. Marriner, D. Martínez-Delgado, T. Matsubara, P. M. McGehee, T. A. McKay, A. Meiksin, H. L. Morrison, J. A. Munn, R. Nakajima, E. H. Neilsen, Jr., H. J. Newberg, R. C. Nichol, T. Nicinski, M. Nieto-Santisteban, A. Nitta, S. Okamura, R. Owen, H. Oyaizu, N. Padmanabhan, K. Pan, C. Park, J. J. Peoples, J. R. Pier, A. C. Pope, N. Purger, M. J. Raddick, P. Re Fiorentin, G. T. Richards, M. W. Richmond, A. G. Riess, H.-W. Rix, C. M. Rockosi, M. Sako, D. J. Schlegel, D. P. Schneider, M. R. Schreiber, A. D. Schwope, U. Seljak, B. Sesar, E. Sheldon, K. Shimasaku, T. Sivarani, J. A. Smith, S. A. Snedden, M. Steinmetz, M. A. Strauss, M. SubbaRao, Y. Suto, A. S. Szalay, I. Szapudi, P. Szkody, M. Tegmark, A. R. Thakar, C. A. Tremonti, D. L. Tucker, A. Uomoto, D. E. Vanden Berk, J. Vandenberg, S. Vidrih, M. S. Vogeley, W. Voges, N. P. Vogt, Y. Wadadekar, D. H. Weinberg, A. A. West, S. D. M. White, B. C. Wilhite, B. Yanny, D. R. Yocum, D. G. York, I. Zehavi, and D. B. Zucker. The Sixth Data Release of the Sloan Digital Sky Survey. *ApJS*, 175:297–313, Apr 2008.

[29] K. Abazajian and f. t. Sloan Digital Sky Survey. The Seventh Data Release of the Sloan Digital Sky Survey. *ApJS*, 2009.

[30] SDSS Website. http://www.sdss.org, Oct 2008.

[31] R. A. Ibata, G. Gilmore, and M. J. Irwin. A Dwarf Satellite Galaxy in Sagittarius. *Nature*, 370:194–+, jul 1994.

[32] C. J. Grillmair, K. C. Freeman, M. Irwin, and P. J. Quinn. Globular Clusters with Tidal Tails: Deep Two-Color Star Counts. *AJ*, 109:2553–+, jun 1995.

[33] M. Irwin and D. Hatzidimitriou. Structural parameters for the Galactic dwarf spheroidals. *MNRAS*, 277:1354–1378, dec 1995.

[34] J. R. Kuhn, H. A. Smith, and S. L. Hawley. Tidal Disruption and Tails from the Carina Dwarf Spheroidal Galaxy. *ApJ*, 469:L93+, oct 1996.

[35] S. R. Majewski, S. L. Hawley, and J. A. Munn. Moving Groups, Stellar Streams and Phase Space Substructure in the Galactic Halo. In H. L. Morrison and A. Sarajedini, editors, *Formation of the Galactic Halo...Inside and Out*, volume 92 of *Astronomical Society of the Pacific Conference Series*, pages 119–+, apr 1996.

[36] R. Ibata, M. Irwin, G. F. Lewis, and A. Stolte. Galactic Halo Substructure in the Sloan Digital Sky Survey: The Ancient Tidal Stream from the Sagittarius Dwarf Galaxy. *ApJ*, 547:L133–L136, feb 2001.

[37] R. Ibata, G. F. Lewis, M. Irwin, E. Totten, and T. Quinn. Great Circle Tidal Streams: Evidence for a Nearly Spherical Massive Dark Halo around the Milky Way. *ApJ*, 551:294–311, apr 2001.

[38] B. Yanny, H. J. Newberg, S. Kent, S. A. Laurent-Muehleisen, J. R. Pier, G. T. Richards, C. Stoughton, J. E. Anderson, Jr., J. Annis, J. Brinkmann, B. Chen, I. Csabai, M. Doi, M. Fukugita, G. S. Hennessy, Ž. Ivezić, G. R. Knapp, R. Lupton, J. A. Munn, T. Nash, C. M. Rockosi, D. P. Schneider, J. A. Smith, and D. G. York. Identification of A-colored Stars and Structure in the Halo of the Milky Way from Sloan Digital Sky Survey Commissioning Data. *ApJ*, 540:825–841, sep 2000.

[39] H. J. Newberg, B. Yanny, C. Rockosi, E. K. Grebel, H.-W. Rix, J. Brinkmann, I. Csabai, G. Hennessy, R. B. Hindsley, R. Ibata, Z. Ivezić, D. Lamb, E. T. Nash, M. Odenkirchen, H. A. Rave, D. P. Schneider, J. A. Smith, A. Stolte, and D. G. York. The Ghost of Sagittarius and Lumps in the Halo of the Milky Way. *ApJ*, 569:245–274, Apr 2002.

[40] B. Yanny, H. J. Newberg, E. K. Grebel, S. Kent, M. Odenkirchen, C. M. Rockosi, D. Schlegel, M. Subbarao, J. Brinkmann, M. Fukugita, Ž. Ivezic, D. Q. Lamb, D. P. Schneider, and D. G. York. A Low-Latitude Halo Stream around the Milky Way. *ApJ*, 588:824–841, may 2003.

[41] C. J. Grillmair. Substructure in Tidal Streams: Tributaries in the Anticenter Stream. *ApJ*, 651:L29–L32, nov 2006.

[42] C. J. Grillmair, J. L. Carlin, and S. R. Majewski. Fishing in Tidal Streams: New Radial Velocity and Proper Motion Constraints on the Orbit of the Anticenter Stream. *ApJ*, 689:L117–L120, dec 2008.

[43] H. J. Rocha-Pinto, S. R. Majewski, M. F. Skrutskie, J. D. Crane, and R. J. Patterson. Exploring Halo Substructure with Giant Stars: A Diffuse Star Cloud or Tidal Debris around the Milky Way in Triangulum-Andromeda. *ApJ*, 615:732–737, nov 2004.

[44] J. Peñarrubia, D. Martínez-Delgado, H. W. Rix, M. A. Gómez-Flechoso, J. Munn, H. Newberg, E. F. Bell, B. Yanny, D. Zucker, and E. K. Grebel. A Comprehensive Model for the Monoceros Tidal Stream. *ApJ*, 626:128–144, jun 2005.

[45] A. K. Vivas, R. Zinn, P. Andrews, C. Bailyn, C. Baltay, P. Coppi, N. Ellman, T. Girard, D. Rabinowitz, B. Schaefer, J. Shin, J. Snyder, S. Sofia, W. van Altena, C. Abad, A. Bongiovanni, C. Briceño, G. Bruzual, F. Della Prugna, D. Herrera, G. Magris, J. Mateu, R. Pacheco, G. Sánchez, G. Sánchez, H. Schenner, J. Stock, B. Vicente, K. Vieira, I. Ferrín, J. Hernandez, M. Gebhard, R. Honeycutt, S. Mufson, J. Musser, and A. Rengstorf. The QUEST RR Lyrae Survey: Confirmation of the Clump at 50 Kiloparsecs and Other Overdensities in the Outer Halo. *ApJ*, 554:L33–L36, jun 2001.

[46] S. Duffau, R. Zinn, A. K. Vivas, G. Carraro, R. A. Méndez, R. Winnick, and C. Gallart. Spectroscopy of QUEST RR Lyrae Variables: The New Virgo Stellar Stream. *ApJ*, 636:L97–L100, jan 2006.

[47] H. J. Newberg, B. Yanny, N. Cole, T. C. Beers, P. Re Fiorentin, D. P. Schneider, and R. Wilhelm. The Overdensity in Virgo, Sagittarius Debris, and the Asymmetric Spheroid. *ApJ*, 668:221–235, oct 2007.

[48] C. J. Grillmair. Detection of a 60°-long Dwarf Galaxy Debris Stream. *ApJ*, 645:L37–L40, jul 2006.

[49] V. Belokurov, D. B. Zucker, N. W. Evans, G. Gilmore, S. Vidrih, D. M. Bramich, H. J. Newberg, R. F. G. Wyse, M. J. Irwin, M. Fellhauer, P. C. Hewett, N. A. Walton, M. I. Wilkinson, N. Cole, B. Yanny, C. M. Rockosi, T. C. Beers, E. F. Bell, J. Brinkmann, Ž. Ivezić, and R. Lupton. The Field of Streams: Sagittarius and Its Siblings. *ApJ*, 642:L137–L140, may 2006.

[50] H. J. Newberg and B. Yanny. *submitted*, 2009.

[51] B. Willman, J. J. Dalcanton, D. Martinez-Delgado, A. A. West, M. R. Blanton, D. W. Hogg, J. C. Barentine, H. J. Brewington, M. Harvanek, S. J. Kleinman,

J. Krzesinski, D. Long, E. H. Neilsen, Jr., A. Nitta, and S. A. Snedden. A New Milky Way Dwarf Galaxy in Ursa Major. *ApJ*, 626:L85–L88, jun 2005.

[52] D. B. Zucker, V. Belokurov, N. W. Evans, M. I. Wilkinson, M. J. Irwin, T. Sivarani, S. Hodgkin, D. M. Bramich, J. M. Irwin, G. Gilmore, B. Willman, S. Vidrih, M. Fellhauer, P. C. Hewett, T. C. Beers, E. F. Bell, E. K. Grebel, D. P. Schneider, H. J. Newberg, R. F. G. Wyse, C. M. Rockosi, B. Yanny, R. Lupton, J. A. Smith, J. C. Barentine, H. Brewington, J. Brinkmann, M. Harvanek, S. J. Kleinman, J. Krzesinski, D. Long, A. Nitta, and S. A. Snedden. A New Milky Way Dwarf Satellite in Canes Venatici. *ApJ*, 643:L103–L106, jun 2006.

[53] D. B. Zucker, V. Belokurov, N. W. Evans, J. T. Kleyna, M. J. Irwin, M. I. Wilkinson, M. Fellhauer, D. M. Bramich, G. Gilmore, H. J. Newberg, B. Yanny, J. A. Smith, P. C. Hewett, E. F. Bell, H.-W. Rix, O. Y. Gnedin, S. Vidrih, R. F. G. Wyse, B. Willman, E. K. Grebel, D. P. Schneider, T. C. Beers, A. Y. Kniazev, J. C. Barentine, H. Brewington, J. Brinkmann, M. Harvanek, S. J. Kleinman, J. Krzesinski, D. Long, A. Nitta, and S. A. Snedden. A Curious Milky Way Satellite in Ursa Major. *ApJ*, 650:L41–L44, oct 2006.

[54] V. Belokurov, D. B. Zucker, N. W. Evans, M. I. Wilkinson, M. J. Irwin, S. Hodgkin, D. M. Bramich, J. M. Irwin, G. Gilmore, B. Willman, S. Vidrih, H. J. Newberg, R. F. G. Wyse, M. Fellhauer, P. C. Hewett, N. Cole, E. F. Bell, T. C. Beers, C. M. Rockosi, B. Yanny, E. K. Grebel, D. P. Schneider, R. Lupton, J. C. Barentine, H. Brewington, J. Brinkmann, M. Harvanek, S. J. Kleinman, J. Krzesinski, D. Long, A. Nitta, J. A. Smith, and S. A. Snedden. A Faint New Milky Way Satellite in Bootes. *ApJ*, 647:L111–L114, aug 2006.

[55] V. Belokurov, D. B. Zucker, N. W. Evans, J. T. Kleyna, S. Koposov, S. T. Hodgkin, M. J. Irwin, G. Gilmore, M. I. Wilkinson, M. Fellhauer, D. M. Bramich, P. C. Hewett, S. Vidrih, J. T. A. De Jong, J. A. Smith, H.-W. Rix, E. F. Bell, R. F. G. Wyse, H. J. Newberg, P. A. Mayeur, B. Yanny, C. M. Rockosi, O. Y. Gnedin, D. P. Schneider, T. C. Beers, J. C. Barentine, H. Brewington, J. Brinkmann, M. Harvanek, S. J. Kleinman, J. Krzesinski, D. Long, A. Nitta, and S. A. Snedden. Cats and Dogs, Hair and a Hero: A Quintet of New Milky Way Companions. *ApJ*, 654:897–906, jan 2007.

[56] M. J. Irwin, V. Belokurov, N. W. Evans, E. V. Ryan-Weber, J. T. A. de Jong, S. Koposov, D. B. Zucker, S. T. Hodgkin, G. Gilmore, P. Prema, L. Hebb, A. Begum, M. Fellhauer, P. C. Hewett, R. C. Kennicutt, Jr., M. I. Wilkinson, D. M. Bramich, S. Vidrih, H.-W. Rix, T. C. Beers, J. C. Barentine, H. Brewington, M. Harvanek, J. Krzesinski, D. Long, A. Nitta, and S. A. Snedden. Discovery of an Unusual Dwarf Galaxy in the Outskirts of the Milky Way. *ApJ*, 656:L13–L16, feb 2007.

[57] M. Metz, P. Kroupa, C. Theis, G. Hensler, and H. Jerjen. Did the Milky Way dwarf satellites enter the halo as a group? *ArXiv e-prints*, mar 2009.

[58] M. Odenkirchen, E. K. Grebel, C. M. Rockosi, W. Dehnen, R. Ibata, H.-W. Rix, A. Stolte, C. Wolf, J. E. Anderson, Jr., N. A. Bahcall, J. Brinkmann, I. Csabai, G. Hennessy, R. B. Hindsley, Ž. Ivezić, R. H. Lupton, J. A. Munn, J. R. Pier, C. Stoughton, and D. G. York. Detection of Massive Tidal Tails around the Globular Cluster Palomar 5 with Sloan Digital Sky Survey Commissioning Data. *ApJ*, 548:L165–L169, feb 2001.

[59] C. M. Rockosi, M. Odenkirchen, E. K. Grebel, W. Dehnen, K. M. Cudworth, J. E. Gunn, D. G. York, J. Brinkmann, G. S. Hennessy, and Ž. Ivezić. A Matched-Filter Analysis of the Tidal Tails of the Globular Cluster Palomar 5. *AJ*, 124:349–363, jul 2002.

[60] C. J. Grillmair and O. Dionatos. A 22° Tidal Tail for Palomar 5. *ApJ*, 641:L37–L39, apr 2006.

[61] C. J. Grillmair and R. Johnson. The Detection of a 45° Tidal Stream Associated with the Globular Cluster NGC 5466. *ApJ*, 639:L17–L20, mar 2006.

[62] V. Belokurov, N. W. Evans, M. J. Irwin, P. C. Hewett, and M. I. Wilkinson. The Discovery of Tidal Tails around the Globular Cluster NGC 5466. *ApJ*, 637:L29–L32, jan 2006.

[63] C. J. Grillmair. Four New Stellar Debris Streams in the Galactic Halo. *ApJ*, 693:1118–1127, mar 2009.

[64] C. J. Grillmair and O. Dionatos. Detection of a 63° Cold Stellar Stream in the Sloan Digital Sky Survey. *ApJ*, 643:L17–L20, may 2006.

[65] V. Belokurov, N. W. Evans, E. F. Bell, M. J. Irwin, P. C. Hewett, S. Koposov, C. M. Rockosi, G. Gilmore, D. B. Zucker, M. Fellhauer, M. I. Wilkinson, D. M. Bramich, S. Vidrih, H.-W. Rix, T. C. Beers, D. P. Schneider, J. C. Barentine, H. Brewington, J. Brinkmann, M. Harvanek, J. Krzesinski, D. Long, K. Pan, S. A. Snedden, O. Malanushenko, and V. Malanushenko. The Hercules-Aquila Cloud. *ApJ*, 657:L89–L92, mar 2007.

[66] D. Carollo, T. C. Beers, Y. S. Lee, M. Chiba, J. E. Norris, R. Wilhelm, T. Sivarani, B. Marsteller, J. A. Munn, C. A. L. Bailer-Jones, P. R. Fiorentin, and D. G. York. Two stellar components in the halo of the Milky Way. *Nature*, 450:1020–1025, dec 2007.

[67] H. J. Newberg, B. Yanny, E. K. Grebel, G. Hennessy, Ž. Ivezić, D. Martinez-Delgado, M. Odenkirchen, H.-W. Rix, J. Brinkmann, D. Q. Lamb, D. P. Schneider, and D. G. York. Sagittarius Tidal Debris 90 Kiloparsecs from the Galactic Center. *ApJ*, 596:L191–L194, Oct 2003.

[68] M. Bellazzini, R. Ibata, F. R. Ferraro, and V. Testa. Tracing the Sgr Stream with 2MASS. Detection of Stream stars around Outer Halo globular clusters. *A&A*, 405:577–583, jul 2003.

[69] S. R. Majewski, M. F. Skrutskie, M. D. Weinberg, and J. C. Ostheimer. A Two Micron All Sky Survey View of the Sagittarius Dwarf Galaxy. I. Morphology of the Sagittarius Core and Tidal Arms. *ApJ*, 599:1082–1115, dec 2003.

[70] S. R. Majewski, W. E. Kunkel, D. R. Law, R. J. Patterson, A. A. Polak, H. J. Rocha-Pinto, J. D. Crane, P. M. Frinchaboy, C. B. Hummels, K. V. Johnston, J. Rhee, M. F. Skrutskie, and M. Weinberg. A Two Micron All Sky Survey View of the Sagittarius Dwarf Galaxy. II. Swope Telescope Spectroscopy of M Giant Stars in the Dynamically Cold Sagittarius Tidal Stream. *AJ*, 128:245–259, jul 2004.

[71] D. Martínez-Delgado, M. Á. Gómez-Flechoso, A. Aparicio, and R. Carrera. Tracing Out the Northern Tidal Stream of the Sagittarius Dwarf Spheroidal Galaxy. *ApJ*, 601:242–259, jan 2004.

[72] M. Fellhauer, V. Belokurov, N. W. Evans, M. I. Wilkinson, D. B. Zucker, G. Gilmore, M. J. Irwin, D. M. Bramich, S. Vidrih, R. F. G. Wyse, T. C. Beers, and J. Brinkmann. The Origin of the Bifurcation in the Sagittarius Stream. *ApJ*, 651:167–173, nov 2006.

[73] M.-Y. Chou, S. R. Majewski, K. Cunha, V. V. Smith, R. J. Patterson, D. Martínez-Delgado, D. R. Law, J. D. Crane, R. R. Muñoz, R. Garcia López, D. Geisler, and M. F. Skrutskie. A 2MASS All-Sky View of the Sagittarius Dwarf Galaxy. V. Variation of the Metallicity Distribution Function along the Sagittarius Stream. *ApJ*, 670:346–362, nov 2007.

[74] K. V. Johnston, D. N. Spergel, and L. Hernquist. The Disruption of the Sagittarius Dwarf Galaxy. *ApJ*, 451:598–+, oct 1995.

[75] R. A. Ibata, R. F. G. Wyse, G. Gilmore, M. J. Irwin, and N. B. Suntzeff. The Kinematics, Orbit, and Survival of the Sagittarius Dwarf Spheroidal Galaxy. *AJ*, 113:634–655, feb 1997.

[76] M. A. Gómez-Flechoso, R. Fux, and L. Martinet. Sagittarius, a dwarf spheroidal galaxy without dark matter? *A&A*, 347:77–91, jul 1999.

[77] A. Helmi and S. D. M. White. Simple dynamical models of the Sagittarius dwarf galaxy. *MNRAS*, 323:529–536, may 2001.

[78] D. R. Law, S. R. Majewski, M. F. Skrutskie, and K. V. Johnston. Modeling the Tidal Tails of the Sagittarius Dwarf Galaxy. In F. Prada, D. Martinez Delgado, and T. J. Mahoney, editors, *Satellites and Tidal Streams*, volume 327 of *Astronomical Society of the Pacific Conference Series*, pages 239–+, dec 2004.

[79] D. R. Law, K. V. Johnston, and S. R. Majewski. A Two Micron All-Sky Survey View of the Sagittarius Dwarf Galaxy. IV. Modeling the Sagittarius Tidal Tails. *ApJ*, 619:807–823, Feb 2005.

[80] K. V. Johnston, H. Zhao, D. N. Spergel, and L. Hernquist. Tidal Streams as Probes of the Galactic Potential. *ApJ*, 512:L109–L112, feb 1999.

[81] R. Fletcher. *Practical Methods of Optimization*. Wiley-Interscience, New York, NY, second edition, 1987.

[82] L. Hernquist. An analytical model for spherical galaxies and bulges. *ApJ*, 356:359–364, Jun 1990.

[83] H. J. Newberg and B. Yanny. The Milky Way's stellar halo - lumpy or triaxial? *Journal of Physics Conference Series*, 47:195–204, Oct 2006.

[84] Michael T. Heath. *Scientific Computing*. McGraw-Hill, New York, NY, second edition, 2002.

[85] T. Desell, N. Cole, M. Magdon-Ismail, H. Newberg, B. Szymanski, and C. Varela. Distributed and Generic Maximum Likelihood Evaluation. In *3rd IEEE International Conference on e-Science and Grid Computing*, pages 337–344, Dec 2007.

[86] Carlos A. Varela and Gul Agha. Programming Dynamically Reconfigurable Open Systems with SALSA. *ACM SIGPLAN Notices. OOPSLA'2001 Intriguing Technology Track Proceedings*, 36(12):20–34, dec 2001.

[87] W. Gropp, E. Lusk, N. Doss, and A. Skjellum. A high-performance, portable implementation of the MPI message passing interface standard . *Parallel Computing*, 22(6):789–828, sep 1996.

[88] David P. Anderson, Eric Korpela, and Rom Walton. High-Performance Task Distribution for Volunteer Computing. *e-Science*, pages 196–203, 2005.

[89] P. Teuben. The Stellar Dynamics Toolbox NEMO. In R. A. Shaw, H. E. Payne, and J. J. E. Hayes, editors, *Astronomical Data Analysis Software and Systems IV*, volume 77 of *Astronomical Society of the Pacific Conference Series*, pages 398–+, 1995.

[90] K. Freese, P. Gondolo, and H. J. Newberg. Detectability of weakly interacting massive particles in the Sagittarius dwarf tidal stream. *Phys. Rev. D*, 71(4):043516–+, feb 2005.

[91] D. J. Schlegel, D. P. Finkbeiner, and M. Davis. Maps of Dust Infrared Emission for Use in Estimation of Reddening and Cosmic Microwave Background Radiation Foregrounds. *ApJ*, 500:525–+, jun 1998.

[92] E. F. Bell, D. B. Zucker, V. Belokurov, S. Sharma, K. V. Johnston, J. S. Bullock, D. W. Hogg, K. Jahnke, J. T. A. de Jong, T. C. Beers, N. W. Evans, E. K. Grebel, Ž. Ivezić, S. E. Koposov, H.-W. Rix, D. P. Schneider, M. Steinmetz, and A. Zolotov. The Accretion Origin of the Milky Way's Stellar Halo. *ApJ*, 680:295–311, jun 2008.

APPENDIX A
Standard Candles

A "standard candle" is an object that has a well known intrinsic brightness which allows for the estimation of the star's distance throught the inverse square law of brightness. The inverse square law simply states that the apparent brightness (magnitude) of a star will decrease with the square of the distance. The absolute magnitude is defined as the apparent magnitude a star would have if it were 10 pc away. Using this definition, it is possible to calculate the distance of a star using the observed brightness of the star, its apparent magnitude, g, via the equation

$$g - M_g = 5 \log \frac{d}{10\text{pc}}, \tag{A.1}$$

where g is the star's apparent magnitude, M_g is the star's absolute magnitude, and d is the star's distance.

The best stars for use as standard candles are variable stars, such as Cepheids or RR Lyraes, which have very well defined period-luminosity relationships, this allows for the calculation of a very precise absolute magnitude and therefore the most accurate distance estimate possible. However, these are rare and do not provide a significant sampling over the sky nor of all stellar populations. Other star types that make good standard candles are those that occur at approximately a constant absolute magnitude on a color-magnitude diagram (CMD). A color magnitude diagram depicts a star's magnitude versus the difference of two color filters, these diagrams closely parallel those of Hertzsprung-Russell (H-R) diagrams which depict luminosity versus temperature. Therefore stars that occur approximately along a horizontal line on these diagrams make good standard candles. Blue horizontal branch (BHB) stars, one type of A colored star, are a good example of this; these stars are very bright, and can therefore be seen at large distances, and are at a relatively constant absolute magnitude. However, these stars are still somewhat low in number and do not occur in sufficient numbers for a study of this type.